

The Phonovoltaic Cell: Harvesting Optical Phonons in Order to Approach the Carnot Limit

by
Corey Melnick

A dissertation submitted in partial fulfillment
of the requirements for the degree of
Doctor of Philosophy
(Mechanical Engineering)
in The University of Michigan
2017

Doctoral Committee:

Professor Massoud Kaviani, Chair
Professor Jamie Phillips
Associate Professor Kevin Pipe
Professor Ctirad Uher

Corey Melnick
cmelni@umich.edu
ORCID iD: 0000-0003-1105-6336

ACKNOWLEDGEMENTS

My time at the University of Michigan has been an singular experience, in large part due to the community of friends, colleagues, and educators I have met. Without their support and camaraderie, it is hard to imagine how I could have succeeded in arriving here and writing this dissertation. I will do my best to thank them, and I will start by writing: thank you, everyone.

Then, I would like to thank those professors who were instrumental to my success at Michigan. In particular, I would like to thank my adviser, Professor Massoud Kaviani, without whom I would not have been able to pursue this research and persist through its difficulties. His willingness and enthusiasm to discuss and support my research was a constant for which I am grateful. In addition, I would like to thank the remaining members of my committee, Professors Ctirad Uher, Jamie Phillips, and Kevin pipe, for their advice, for the discussions regarding the phonovoltaic during its inception, and for their insightful questions throughout the course of my research. Professor Alan McGaughey also provided thoughtful and invaluable advice as I approached my dissertation, for which I am grateful. Finally, I would like to thank Professor Marc Hodes, without whom I would never have considered entering the world of research.

I would also like to thank the members of my research group who were and continue to sources of advice for my research and life at Michigan. I would especially like to acknowledge Seungha Shin and Hyounghul Kim, who helped me acclimate to

my graduate studies, and whose advice was a necessity as a young graduate student.

Lastly, I would like to thank my friends and family whose support, faith, company, and love was a constant source of motivation and camaraderie. Without them, life would have been difficult; with them, it was fun. So thank you Zakir, Pat, and Brad for your companionship; thank you Erin for your love; thank you mom and dad, bro and sis, for being the best family I ever had; and thank you again to the many wonderful people who are or have been a part of my life at Michigan.

This work was supported by the NSF program on Thermal Transport and Processes (Award No. CBET1332807) and employed computing resources of the DOE National Energy Research Scientific Computing Center (Office of Science, Contract No. DE-AC02-05CH11231).

TABLE OF CONTENTS

ACKNOWLEDGEMENTS	ii
LIST OF FIGURES	vi
LIST OF TABLES	xii
LIST OF APPENDICES	xiii
ABSTRACT	xiv
CHAPTER	
I. Introduction to Phonovoltaic Cells and Materials	1
1.1 Non-equilibrium optical phonons as an energy source	2
1.2 The phonovoltaic cell	4
1.3 The unique properties of graphene for use in a phonovoltaic cell	6
1.4 Statement of objective and scope of thesis	8
II. Central Mechanisms of the Phonovoltaic cell	11
2.1 Scattering interactions and rates	11
2.2 Electron-phonon coupling	12
2.3 Phonon-phonon coupling	17
2.4 Phonon-defect coupling	18
2.5 Evaluating $\dot{\gamma}_{e-p}^*$	19
III. Phonovoltaic Regime, Efficiency, and Material Figure of Merit	21
3.1 The phonovoltaic regime and comparison to thermoelectric and photovoltaic cells	22
3.2 Non-equilibrium in the phonovoltaic cell	26
3.3 Analytic efficiency and figure of merit	32
3.3.1 Net generation	34
3.3.2 Current-voltage curve	36
3.3.3 Efficiency	37
3.3.4 Results	38
3.4 Hydrodynamic efficiency and operation	39
3.4.1 Device operation	42
3.4.2 Achieving analytic efficiency	45
3.4.3 Exceeding analytic efficiency	46
3.5 Conclusions	48
IV. The Importance of Kinetics: A Study of Partially-Hydrogenated Graphene	50

4.1	Partially hydrogenated graphene	50
4.2	Electron properties	53
4.3	Phonon properties	55
4.4	Scattering kinetics	56
	4.4.1 e - p coupling and kinetics	57
	4.4.2 p - p coupling and kinetics	58
	4.4.3 Figure of merit	60
4.5	Conclusions	61
V. A High ZT Material: A Study of Graphene-Boron Nitride Alloys		63
5.1	Graphene:BN	63
5.2	Graphene/BN	65
5.3	Tight binding model	66
5.4	<i>Ab initio</i> results	70
	5.4.1 Methods	71
	5.4.2 Electron and phonon properties	72
	5.4.3 Scattering kinetics	76
5.5	Graphene:BN phonovoltaics	83
5.6	Conclusions	85
VI. An Integrated Graphene Field-Effect Transistor and Phonovoltaic		88
6.1	Combined graphene field-effect transistor and phonovoltaic for in-situ phonon harvest	88
6.2	<i>Ab initio</i> properties of bilayer graphene under a strong electric field	91
	6.2.1 Electronic properties	91
	6.2.2 Electron-phonon coupling and the phonovoltaic figure of merit in bilayer-graphene	93
6.3	Electric fields as a source of hot optical phonons	95
6.4	Monte Carlo simulation of tuned graphene under a field	96
6.5	Conclusions	98
VII. Conclusions and Future Work		100
7.1	Contributions	100
7.2	Future Work	101
7.3	Outlook	102
APPENDICES		104
BIBLIOGRAPHY		119

LIST OF FIGURES

Figure

1.1	Optical phonon sources and sinks. Typically, electronic excitation precedes optical phonon production, and electronic relaxation provides the primary source of optical phonons. These optical phonons can accumulate into a non-equilibrium (hot) population, down-convert into the low-energy acoustic modes (becoming heat), or be harvested to produce energy.	3
1.2	(a) The phonovoltaic (pV) cell and (b) its energy diagram, which shows the quasi-Fermi level (E_F), conduction and valence bands ($E_{e,c}$, $E_{e,v}$), and the generation of an electron-hole pair. In a pV, a source excites a population of optical phonon modes more energetic than the bandgap in a p - n junction. This population relaxes by producing electrons (and power) or acoustic phonons (and heat).	4
1.3	The bandgap and optical phonon energy of various semiconductors. An efficient pV requires $E_{p,O} > \Delta E_{e,g} \gg k_B T$, as in tuned graphene. In typical materials at 300 K, however, $\Delta E_{e,g} \gg E_{p,O}$ or $E_{p,O} \approx k_B T$, as the strong bonds which enable energetic phonon modes also localize electrons and open a large bandgap. The symmetry of group IV, sp^2 coordinated materials (e.g., graphene) enables them to overcome this trend. For traditional elemental and composite semiconductors, see [[47, 1, 88]]. For graphane (h-C:H), see [[84, 51]]. For materials with the sp^1 acetylene bond, graphdiyne and BNyne, see [[32, 96]]	7
1.4	(a) The graphene sheet, its geometry, and brillouin zone (BZ). In graphene, the sp^2 hybridized orbitals of carbon atoms form strong bonds with the three nearest neighbors in a hexagonal lattice (defined by two vectors a_1 and a_2 of length a) with two symmetric, triangular sublattices, separated by δ_1 . (b) h-C/BN bilayers. Real bilayers form Moire superlattices rather than an ideally stacked structure due to the small difference in the h-C and h-BN lattice constants.	8
2.1	The electron-phonon coupling during phonon absorption. (a) The unperturbed system is in equilibrium with an electron in the highest occupied state (HOS, $ \mathbf{k}_e, v\rangle$) and no electron in the lowest unoccupied state (LUS, $ \mathbf{k}'_e, c\rangle$). (b) A phonon is excited (\mathbf{k}_p, α), which displaces the atoms by $\mathbf{u}_{\mathbf{k}_p, \alpha}$ and perturbs the HOS, such that it overlaps with the LUS. (c) The electron in the perturbed HOS and excited phonon are annihilated and an electron is created in the highest occupied state, as shown in (c) \mathbf{k}_e space and in (d) the Feynman diagram.	13

2.2	The ratio of the interband generation rate to the total rate of optical phonon absorption by electrons in graphene. When the optical phonon energy is much larger than $k_B T$ in an intrinsic semiconductor, the rate of interband generation events dominates the rate of intraband heating events until $\Delta E_{e,g} \rightarrow E_{p,O}$. As the optical phonon energy approaches $k_B T$ or as the Fermi level approaches the conduction band edge ($E_F \rightarrow E_{e,c}$), the interband interactions dominate over a much smaller range of bandgap energies. When $E_{p,O}/k_B T < 5$, the intraband interactions always dominate.	14
3.1	Qualitative regimes of a pV cell for variations in L/δ_{e-p} and $\dot{\gamma}_{e-p}^*$. The pV regime requires (i) a device smaller than the electron-phonon cooling length, δ_{e-p} , to sustain a nonequilibrium between the optical phonon and electron populations (NE- e), and (ii) that generation dominates downconversion ($\dot{\gamma}_{e-p}^* > 0.5$). When the local nonequilibrium vanishes (E- e), the pV cell behaves as a TE (TV regime). When generation is much slower than downconversion ($\dot{\gamma}_{e-p}^* < 0.5$), conduction hinders or dominates the device operation (CH regime).	25
3.2	Spatial distributions of the (a) Electron density and (b) temperature, and (c) local energy distributions within the active region in 400 and 40 nm pV cells. The generation rates are scaled by $1/L$ to demonstrate that transport is partially ballistic in the 40 nm cell. The generation of cold electrons reduces the average energy of the population, but the nonequilibrium within the electron population remains small. The 400 nm cell, in comparison, exhibits diffusive transport, a negligible change in the electron temperature, and equilibrium occupancy within the electron population.	31
3.3	The pV efficiency as a function of the nonequilibrium, $\eta_C \Delta E_{e,g}/k_B T_c$, and the pV figure of merit, Z_{pV} [Eq. (3.28)]. Significant nonequilibrium is required to outperform a TE with $Z_{TE} T = 1$, unless the figure of merit exceeds 0.7. When T_c vanishes, the pV cell achieves $\eta_{pV} = \eta_C Z_{pV} \leq 1$. When $Z_{pV} \rightarrow 0$, the efficiency vanishes, and when $\eta_C \rightarrow 0$, the efficiency approaches $0.25\eta_C Z_{pV}$. The hydrodynamic model (HM) simulations use a standard set of parameters slightly exceeding the TE cell.	39
3.4	The pV efficiency as a function of $\eta_C \Delta E_{e,g}^*$ for variations in $\Delta E_{e,g}^*$ and η_C . As shown, the analytical model [Eq. (3.28)] provides a reasonable estimate for the pV cell performance. A significant nonequilibrium ($\eta_C \Delta E_{e,g}^*$) is required to exceed the TE efficiency (shown for $Z_{TE} T = 1.0$) when $Z_{pV} < 0.7$	41
3.5	Spatial distributions of (a) the electron and hole densities, (b) population temperatures, and (c) generation and downconversion rates for a pV cell under 5 mV of applied voltage (maximum power) with $T_c = 300$ K and $T_{p,O} = 900$ K in the active region. The abrupt drop in the optical phonon temperature outside the active region leads to recombination and a lowered open-circuit voltage. Downconversion, however, extends throughout the cell.	43
3.6	(a) Dimensionless and (b) dimensional current-voltage curves for variations in T_c for the pV cell parameters in Table 3.3. As expected, the quantum efficiency, open-circuit voltage ($\Delta\varphi_o$), and efficiency are limited by $\dot{\gamma}_{e-p}^*$, $\eta_C \Delta E_{e,g}$, and Z_{pV} . This limiting efficiency is approached as T_c vanishes and the nonequilibrium extends across the entire cell, i.e., when $F_F \rightarrow 1$ and $L_a = L$	44

3.7	Efficiency of a pV cell for variations in $\hat{\gamma}_{e-p}^*$ using the analytical (AM) and hydrodynamic (HM) models. While increased resonance between $E_{p,O}$ and $\Delta E_{e,g}$ increases efficiency, increasing $\hat{\gamma}_{e-p}^*$ enables the efficiency to approach its limit: $\eta_C Z_{pV}$. Moreover, it greatly reduces the impact the temperature has on the efficiency and enables efficient room-temperature operation. The TE efficiency is shown for comparison.	47
4.1	(a,b) Graphane in the chair configuration and (c) graphene and (d) partially hydrogenated graphene. Hydrogenation opens a bandgap by altering the sp^2 hybridized structure of graphene and transforming it into a sp^3 structure.	51
4.2	(a) Formation energy of graphane structures for an increasing number of hydrogen in a chair configured island. Each island tested has fully hydrogenated carbon rings ($C_6H_{1 \times 6}$). Nearly complete concentric rings (22 H) or complete concentric rings (24 H) are required for stability. (b) Graphane cells $C_{128}H_{1 \times 6}$ and $C_{128}H_{1 \times 24}$ are shown.	52
4.3	Electron Dispersion of lowest-energy bands in graphene (C_{128}) and graphane ($C_{128}H_{N_R \times N_H}$) for variation in the number of islands (N_R) and number of hydrogen atoms per island (N_H). (a) At low hydrogen concentrations, no bandgap opens but the Dirac-point moves towards X along the Γ -X high-symmetry line. (b) A trap band forms for an uneven number of hydrogen atoms. (c) At large hydrogen concentrations, however, a narrow bandgap opens at X. Some discontinuities arise from the crossing of the π and σ bands.	54
4.4	Electron density of states for graphene and graphane. The density of states is not affected significantly at (a) low hydrogen concentrations, (b) unless an unpaired electron is left in the structure ($C_{128}H_{1 \times 13}$, $C_{128}H_{1 \times 19}$). (c) A significant bandgap is not formed until the structures become stable ($C_{128}H_{1 \times 22}$), at which point a 250 meV bandgap opens.	55
4.5	Phonon dispersion and density of states (D_p) for (a) graphane, (b) graphene, and $C_{128}H_{1 \times 24}$, where D_p is scaled by the number of modes (n_m) per unit cell. As expected, the $C_{128}H_{1 \times 24}$ phonon density of states shows a combination of the graphene and graphane optical phonon modes. These include (in order of energy) the energetic A_{1g} and A_{2u} graphane modes (out-of-plane hydrogen vibration), the E_{2g} mode (graphene), the A'_1 mode (graphene mode - Kohn Anomaly), and E_g (graphane).	56
4.6	Contours of constant $e-p$ coupling ($ M_{e-p} $) and energy conserving lines (δ_E) of a selected phonon modes in (a) graphene and (b) $C_{128}H_{1 \times 24}$. The (c) intraband and (d) interband $e-p$ coupling strength at the band-edge (X) for variations in $E_{p,O}$ and the phonon lifetime ($1/\hat{\gamma}_{e-p}$) of selected modes.	57
4.7	(a) Active downconversion pathways, (b) energy of the phonon modes produced, and (c) the scattering rate as a function of temperature for graphene E_{2g} and graphane E_g modes. Graphane exhibits significantly enhanced optical phonon downconversion rates.	59

4.8	The fraction of hot optical phonons which generate electrons as they relax ($\dot{\gamma}_{e-p}^*$) and pV figure of merit (Z_{pV}) for graphene and tuned $C_{128}H_{1 \times 24}$ cells. Also shown is the graphene figure of merit if the $e-p$ and $p-p$ couplings remained constant as the bandgap opens. This figure of merit is substantially larger than that of $C_{128}H_{1 \times 24}$, as the interaction between the σ and σ^* bands is much weaker than that between the π and π^* bands in Graphene.	60
5.1	(a) The band structure (ϵ_{\pm}) and (b) fraction of the electron wavefunction composed by atomic orbitals centered on atoms in one of the two sublattices ($ \beta_i^{\pm} / \sum \beta_i^{\pm} $) and resulting overlap ($I_{\mathbf{k}_e, \mathbf{k}_e'}^{\pm}$) of the valence (-) and conduction(+) bands with (—) and without (--) sublattice symmetry. In a symmetric crystal like graphene, no gap exists and the valence- and conduction-band wavefunctions overlap. In a non-symmetric crystal like h-BN, a band gap opens, the valence and conduction bands collapse into atomic orbitals centered on different sublattices, and the overlap between them vanishes at the band edge, proscribing the $e-p$ interaction.	69
5.2	The band gap of h-C:BN and h-C/BN for variations in the BN concentration. The band gap tends to increase as the concentration increases, particularly when the B and N atoms are substituted into different sublattices (ordered h-C:BN _o), as previously predicted.[56] Conversely, the band gap widens slowly with the disordered substitution of BN onto random sublattices (h-C:BN _d). The experimental results[9] show that the gap widens even more quickly than in h-C:BN _o . Regardless, a few of the simulated crystals meet the primary pV condition: $E_{p,O} > \Delta E_{e,g}$	72
5.3	The electronic structure of (a) h-C and h-BN, (b) h-C/BN, and (c) h-C ₄₈ (BN) _{1,o} . The band structure of h-C/BN strongly resembles the superposition of the h-C and h-BN band structures. The band structure of h-C ₄₈ (BN) _{1,o} , although complicated by the band-folding, resembles that of h-C. However, the π bands are less energetic and have some dispersion throughout the BZ. Note the narrow band gap formed in h-C:BN and h-C/BN and the large band gap of h-BN.	74
5.4	The phonon density of states (D_p) for h-C:BN and h-C/BN. The density of states in h-C/BN is nearly the superposition of that in h-C and h-BN. While the density of states in h-C:BN strongly resembles that of h-C, the h-C:BN D_p calculation uses a single <i>ab initio</i> dynamical matrix (at $\mathbf{k}_p = \Gamma$). Therefore, the D_p is not as well resolved.	76
5.5	<i>Ab initio</i> (a) Interband $e-p$ coupling and (b) $e-p$ scattering rate in h-C, h-BN, h-C/BN, and h-C:BN for the zone-center, LO phonon mode. The BZ and high symmetry points are shown, along with the ring for which energy is conserved (δ_E). Also shown are two TB models: TB 1, which uses a scaled overlap integral [Eq. (5.14)] as the $e-p$ matrix element; and TB 2, which assumes the matrix element is independent of the band gap. The scattering rate is approximately halved when h-C is doped with BN. However, the $e-p$ coupling remains strong at the K and K' points, regardless of the asymmetry and band gap. Therefore, $\dot{\gamma}_{e-p}$ is nearly independent of $\Delta E_{e,g}$ until $\Delta E_{e,g} \simeq E_{p,O}$, at which point the number of states available for interband transitions vanishes. The TB 2 model predicts this trend.	77

5.6	(a) The p - p coupling in the first BZ, (b) down-conversion pathways, (c) down-converted phonon energy distribution, and (d) down-conversion rates in h-C and h-C/BN. (a), (b), and (c) combine to show the momentum and energy of the acoustic phonon modes produced during down-conversion of the LO phonon. These results show that the p - p coupling is nearly unaffected by the disruption of the sublattice symmetry, such that the down-conversion rate of h-C/BN approximately equals that in graphene.	80
5.7	(a) Spectral function and (b) defect scattering rate for h-C:BN. While the rate of scattering is negligible at a low BN concentration, it increases substantially with the BN concentration. However, only a small BN concentration is required to tune the band gap to the optical phonon energy.[9]	82
5.8	(a) The optical phonon scattering rates of h-C, h-BN, h-C/BN, and h-C:BN and (b) resulting h-C:BN performance metrics. The TB 2 model (Sec. 5.4.3) is used to model the $\dot{\gamma}_{e-p}$ trends and interpolate performance between the <i>ab initio</i> h-C:BN results. While the incorporation of BN in h-C disrupts its strong e - p coupling, $\dot{\gamma}_{e-p}$ remains much faster than $\dot{\gamma}_{p-p}$ until $\Delta E_{e,g} \rightarrow E_{p,O}$. Moreover, the defect scattering rate remains negligible in comparison to both $\dot{\gamma}_{e-p}$ and $\dot{\gamma}_{p-p}$. Thus, the $\dot{\gamma}_{e-p}^*$ in h-C:BN remains near 0.75 and Z_{pV} nearly reaches 0.7 at $\Delta E_{e,g} = 181$ meV. As the non-equilibrium between optical phonon population and cell increase ($\eta_C \rightarrow 1$), the fill factor of the cell increases, and the efficiency ($\eta_p V$) approaches the figure of merit (Z_{pV}) times the Carnot limit (η_C) [Eq. (3.28)], as shown using the color gradation.	84
6.1	(A) An integrated graphene FET and pV and (b) bilayer graphene (BG) sandwiched between h-BN and under and electric field. A transistor field is constant applied between the source and drain. When the gate field is applied, it opens a large band gap and prohibits electronic transport in the FET. The pV diode harvests optical phonons released as ballistic electrons deposit their energy in the drain, reducing the amount of heat generated by the transistor.	89
6.2	(a) The band gap in bilayer-graphene under a strong electric field and (b) the resulting electronic dispersion. The band gap is nearly proportional to the field, and a band gap exceeding 200 meV is nearly possible within the quasi-linear regime. Once the band gap grows beyond around 100 meV, the topology of constant energy contours change near the band edge, transitioning from single- to double-rings: Note the quartic electronic bands near K.	92
6.3	(a) the electron-phonon coupling in bilayer graphene under a field, (b) the resulting scattering rate, and (c) the $\dot{\gamma}_{e-p}^*$ and pV figure of merit for variations in the bandgap. The electron-phonon coupling vanishes at the K points, but remains strong very near them. Initially, the electron-phonon coupling decreases as the energy-conserving transitions draw closer to the K points. As the band gap increases, the change in the topology of the band-structure enables more energy conserving transitions, some of which are relatively far from K. Thus, the scattering rate increases drastically and the Z_{pV} reaches a record 0.9.	94

6.4	Electric fields as a source of hot optical phonons in tuned graphene. (a) An illustration of the electron dispersion and electron and hole populations in tuned graphene. Under a field, these populations are shifted symmetrically in \mathbf{k}_e space, and the excited electrons release optical phonons. (b) If the valence and conduction bands are not in-line, (c) or if the phonon released does not follow this line, then the released optical phonons have too much momentum to generate electrons. (d) If the phonon released is in-line with the bands, then that phonon can generate electrons.	95
6.5	(a) The energy distribution of electrons before and after the application of a strong electric field and the final momentum distributions of (b) electron and (c) phonon populations. The electric field (oriented along $\theta = \pi$) shifts the electron distribution towards $\theta_e = 0$. These electrons, in turn, primarily emit phonons with $\theta_p = 0$. Similarly, the field creates a hole distribution near $\theta_e = \pi$, which also emits phonons near $\theta_p = 0$, as a hole losing momentum indicates an electron losing the opposite momentum.	97
A.1	The low-energy bandstructure of graphene for variations in the uniaxial strain (ϵ_x). Under a small strain, the Dirac-point moves from K towards M and the σ band moves towards the Fermi level at M. Around $\epsilon_x = 0.25$, the Dirac-point reaches M and a bandgap opens between the π bands. Around $\epsilon_x = 0.3$, the σ^* band becomes the first conduction band, reducing the bandgap.	106
B.1	A flowchart of the coupled MC-phonon simulation. The char includes the major subroutines and the primary quantities they manipulate or require. The program requires information on the electronic and phononic bandstructure as well as system information, such as the field strength, Fermi energy, and lattice temperature. Then, the program initializes the electron and phonon populations before proceeding with the main loop, which alternates between the MC loop (which updates the electron distribution) and the phonon block (which updates the phonon distribution and the related scattering mechanisms). After convergence, the electron and phonon distributions are output for analysis.	111
C.1	(a) Minority carrier density and (b) electron and hole currents in a pV cell with and without surface recombination (SR) for variations in the active volume and applied potential. With SR, carriers generated near the contact are lost instead of being collected. Moreover, the applied voltage drives minority carriers into the contacts, instead of reducing the net generation, reducing pV performance.	118

LIST OF TABLES

Table

3.1	A comparison of thermoelectric (TE), phonovoltaic (pV), and photovoltaic (PV) cells and their controlling processes, where $j_e - \Delta\varphi$ is the current-voltage curve, and other symbols are defined in the text.	23
3.2	Material and parameters used in the MC simulations, where m_e is the electron mass. Parameters are chosen to represent partially-hydrogenated graphite.	30
3.3	Material and parameters used in hydrodynamic model simulations at $T_c = 300$ K. Parameters are chosen to represent a hydrogenated graphite pV cell. Parameters are defined in Appendix A.	40

LIST OF APPENDICES

Appendix

A.	Graphene under a uniaxial strain	105
B.	Ensemble Monte Carlo Simulation	107
	B.1 Scattering events	107
	B.2 Free-flight	109
	B.3 The electron-superparticle and time-discretization	109
	B.4 Coupled electron and phonon simulation	110
	B.5 Building an efficient and fast MC program	112
C.	Hydrodynamic Simulations	114
	C.1 Boundary Conditions	116
	C.2 Surface Recombination	117

ABSTRACT

The Phonovoltaic Cell: Harvesting Optical Phonons in Order to Approach the Carnot Limit

by
Corey Melnick

Chair: Professor Massoud Kaviany

A new energy conversion device, the phonovoltaic (pV) cell, is proposed. In this cell, a non-equilibrium (hot) population of optical phonons more energetic than the bandgap produces electron-hole pairs in a p - n junction, which separates them to produce power. That is, it harvests optical phonons like a photovoltaic harvests photons. In this thesis, the function of the pV cell is modeled, suitable materials for the device are investigated, and a possible application is discussed.

In particular, a physically intuitive efficiency equation and material figure of merit are analytically derived in order to describe the function and performance of a pV cell. Then, ensemble Monte Carlo and hydrodynamic transport simulations are used to validate the predictions of this model. In combination, these modeling efforts show that a pV cell can reach the Carnot efficiency, unlike the thermoelectric generator (which is limited in practice by the achievable material figure of merit and theoretically by the coupled electronic and thermal transport).

To reach this promising result, the pV requires a material with a hot optical phonon mode more energetic than its bandgap and much more energetic than the thermal energy ($E_{p,O} > \Delta E_{e,g} \gg k_B T$). Moreover, the hot phonon mode must relax by generating electrons and power (at rate $\dot{\gamma}_{e-p}$) rather than acoustic phonons and heat (at rate $\dot{\gamma}_{p-p}$), i.e., a pV material also requires $\dot{\gamma}_{e-p} > \dot{\gamma}_{p-p}$. By surveying many semiconductors and semimetals and by discussing the relationship between the bandgap and optical phonon energy in typical materials, graphene is shown to be uniquely suited to meet these requirements. Indeed, it has an energetic phonon mode (200 meV), a tunable bandgap, and $\dot{\gamma}_{e-p} > \dot{\gamma}_{p-p}$.

Opening and tuning the bandgap in graphene typically requires altering its time-reversal symmetry or sp^2 hybridization. However, an *ab initio* investigation of partially hydrogenated graphene suggests that altering the hybridization of graphene weakens its electron-phonon coupling and ensures $\dot{\gamma}_{p-p} \gg \dot{\gamma}_{e-p}$. Conversely, an *ab initio* investigation of graphene alloyed with or deposited on boron nitride (h-C:BN or h-C/BN) shows that changing the symmetry of graphene preserves its electron-phonon coupling. Indeed, a h-C:BN pV cell can theoretically exceed 20% efficiency at 300 K at a Carnot limit of 50%, double the efficiency of a typical TE.

Even more impressively, *ab initio* simulations of bilayer graphene under a strong field (FE-BG) show that a FE-BG pV cell can exceed 60% of the Carnot limit at 300 K. This indicates that a combined graphene field-effect transistor and pV (FET-pV) could greatly reduce heat generation in the transistor while simultaneously generating power. Monte-Carlo simulations are performed to investigate the suitability of large electric fields as a source of optical phonons in support of the combined graphene FET-pV. Results indicate that a field can excite a suitable hot, non-equilibrium population of optical phonons.

CHAPTER I

Introduction to Phonovoltaic Cells and Materials

Modern electronic devices generate massive amounts of energy. If this energy is not properly managed, the temperature of the device drastically increases and its performance and reliability suffer. Indeed, modern devices are often limited by the exceptional energy densities they release and by our ability to remove this energy as heat without the device reaching a debilitating temperature. Classical and continuum-based approaches have proven unable to overcome many of the challenges facing these devices. Moreover, restricting investigations to the classical and continuum renders many of the phenomena crucial to their operation invisible, as they only exist on the discrete, quantum level, i.e., on the nanometer and picosecond scales.

In contrast to the classical models, the Schrödinger equation considers the physics inherent to the situation from first-principles (*ab initio*). From this perspective, the discrete quantum states arise which scientists and engineers can manipulate in order to tune material properties controlling energy transport and conversion. Indeed, the foundation of the high-powered electronics and photovoltaic science are based on this atomistic perspective. It follows that research into these subjects benefits from an *ab initio* approach.

However, exact solutions to the Schrödinger equation are only possible for the sim-

plest systems, and the numerical methods including density functional theory (DFT) only enables the approximate and numerical solution for periodic systems with unit cells containing less than a 1,000 atoms. Other atomistic and mesoscale approaches like molecular dynamics simulations or Monte Carlo (MC) simulations of the Boltzmann transport equation (BTE) help to extend discrete modeling into the domain of 500,000 atoms and hundreds of nanometers. In combination with manufacturing advancements, the investment into understanding and exploiting nanoscale phenomena has enabled many advances, including, for example, the creation of thermoelectric (TE) materials with a figure of merit (ZT) greater than one. In this thesis, such an atomistic, *ab initio* approach is taken in order to suggest a new device which could recycle the optical phonons generated in modern devices in-situ, generating power and reducing heat generation.

1.1 Non-equilibrium optical phonons as an energy source

When energy is released in a device, it typically excites the electronic system first, as shown in Fig. 1.1. These non-equilibrium, hot electrons relax by colliding with the crystal lattice and releasing a narrow spectrum high frequency vibrations (optical phonons). Then, this population of non-equilibrium, hot optical phonons down-converts into multiple low-frequency acoustic phonons. That is, the optical phonon population thermalizes.

The resulting, broad-spectrum of acoustic phonons is the primary component of heat, and it has substantially more entropy than its precursor: the narrow-spectrum of non-equilibrium optical phonons. Therefore, intervening before the hot optical phonon population thermalizes and harvesting it should enable a substantially higher conversion efficiency than that achieved in TE generators which harvest heat.

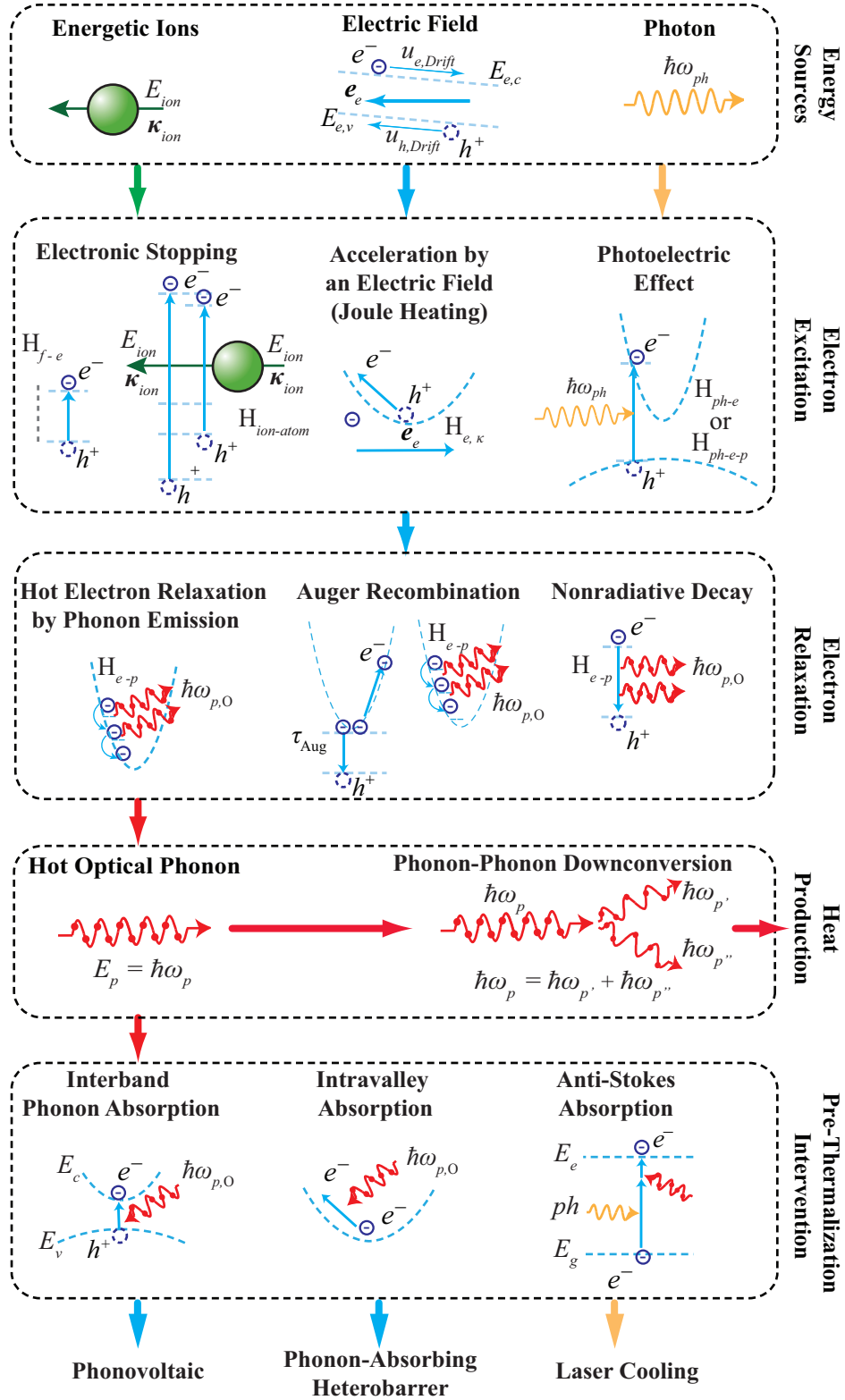


Figure 1.1: Optical phonon sources and sinks. Typically, electronic excitation precedes optical phonon production, and electronic relaxation provides the primary source of optical phonons. These optical phonons can accumulate into a non-equilibrium (hot) population, down-convert into the low-energy acoustic modes (becoming heat), or be harvested to produce energy.

However, the thermalization process typically occurs on the picosecond and nanometer scales, atomic vibrations are limited to below 500 meV, and typical optical phonon energies are below 50 meV. In combination, these factors make targeting and harvesting a hot optical phonon population very challenging. Indeed, most attempts have shown or predicted limited success[72, 73, 79, 78]. Here, a device is proposed which can theoretically utilize the low entropy of non-equilibrium optical phonon populations to approach the Carnot limit: The phonovoltaic (pV) cell.

1.2 The phonovoltaic cell

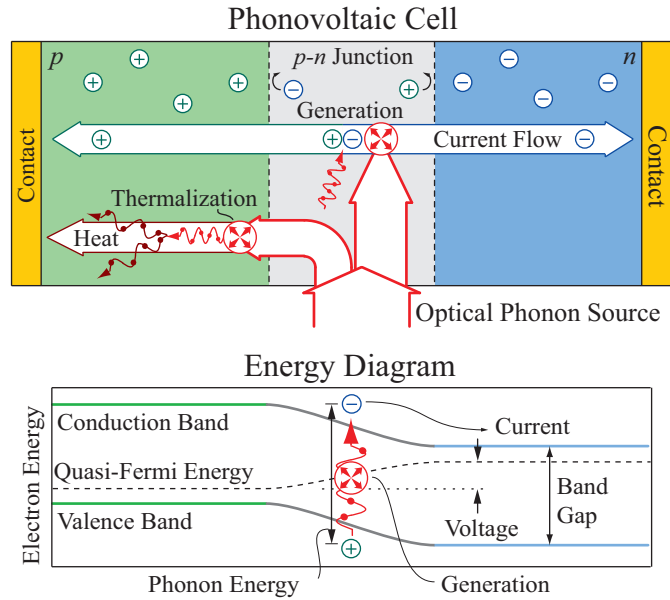


Figure 1.2: (a) The phonovoltaic (pV) cell and (b) its energy diagram, which shows the quasi-Fermi level (E_F), conduction and valence bands ($E_{e,c}$, $E_{e,v}$), and the generation of an electron-hole pair. In a pV, a source excites a population of optical phonon modes more energetic than the bandgap in a p - n junction. This population relaxes by producing electrons (and power) or acoustic phonons (and heat).

The phonovoltaic (pV) cell harvests hot optical phonons like the photovoltaic harvests photons, as shown in Fig. 1.2. It is a nanoscale p - n junction (length L) with metal contacts attached to both the p and n sides (at temperature T_c). Within the junction, a source of optical phonons creates a non-equilibrium (hot) population

of optical phonons (at temperature $T_{p,O}$) more energetic than the bandgap ($E_{p,O} > \Delta E_{e,g}$) and hotter than the cold contacts ($T_{p,O} > T_c$). This hot optical phonon population scatters with the valence electrons to generate electron-hole pairs. Then, the intrinsic field of the p - n junction separates them, forcing electrons (holes) towards the contact on the n (p) side. If the electrons reach and are collected by the contacts before they accumulate in the junction and inhibit further generation, then the device functions like a photovoltaic. That is, it functions like a diode with a supplied phonon current. Conversely, if cell is longer than the collection length ($\delta_e = \nu_e / \dot{\gamma}_{e-p}$, where ν_e is the electron velocity and $\dot{\gamma}_{e-p}$ is the rate of generation), then no significant non-equilibrium grows and the phonovoltaic acts like a thermoelectric.

Few materials excel in a phonovoltaic, due to the stringent requirements discussed here. First, if the phonon mode is more energetic than the bandgap, its extra energy ($E_{p,O} - \Delta E_{e,g}$) is wasted; and if it is less energetic than the bandgap, it cannot generate electrons. Furthermore, the bandgap and optical phonon must be substantially more energetic than the thermal energy; otherwise, the p - n junction to operates inefficiently, and the free carriers inhibit generation. Thus, the phonovoltaic requires a material with $E_{p,O} \approx \Delta E_{e,g} \gg k_B T$, where T is the cell temperature and k_B is the Boltzmann constant. As very few materials have a phonon mode more energetic than 100 meV, and even fewer of these have a small bandgap, finding a promising material candidate is very challenging.

Further difficulties arise from the ability of a hot phonon population to relax through a variety of channels, which includes but is not limited to the generation of electron-hole pairs (at rate $\dot{\gamma}_{e-p}$). For example, optical phonons can down-convert into the acoustic modes (at rate $\dot{\gamma}_{p-p}$), heat the free-carriers (at rate $\dot{\gamma}_{e-p}^{\text{intra}}$), and scatter with defects into unusable phonon modes (at rate $\dot{\gamma}_{p-d}$). These additional

pathways generate heat rather than power. Thus, a pV material not only requires that $E_{p,O} \approx \Delta E_{e,g} \gg k_B T$, but it also requires that the rate of electron generation dominates the rate of heat generation [$\dot{\gamma}_{e-p} > \dot{\gamma}_{p \rightarrow q} = \dot{\gamma}_{p-p} + \dot{\gamma}_{e-p}^{\text{intra}} + \dot{\gamma}_{p-d} + \dots$ or $\dot{\gamma}_{e-p}/(\dot{\gamma}_{e-p} + \dot{\gamma}_{p \rightarrow q}) = \dot{\gamma}_{e-p}^* > 0.5$]. This narrows the field of material candidates further.

However, if a material candidate is found which meets these criteria, the benefits would be momentous: By intervening before a low-entropy optical phonon population spreads into the acoustic modes, gains a substantial amount of entropy, and becomes heat, the phonovoltaic can substantially outperform a thermoelectric device. Indeed, discussions in Chapter III shows that the phonovoltaic cell can approach the Carnot limit (η_C), whereas the thermoelectric cells are limited, in practice, to around $0.2\eta_C$. While the phonovoltaic cell may only reach between $0.5\eta_C$ and $0.7\eta_C$ at 300 K due to the limits in the phonon energy[50], this would be a massive step forward in steady-state heat harvest and recovery. One of the major thrusts of this thesis is to demonstrate these advantages and develop understanding of this new device.

1.3 The unique properties of graphene for use in a phonovoltaic cell

The maximum energy of optical phonons in a typical material is less than 50 meV.[47, 1, 88] Not only does this limit the bandgap and thus the fill-factor of the phonovoltaic at higher temperatures, as discussed previously, but it also inhibits generation, as will be discussed in section 2.2. Only the semiconductors composed of first-row elements (e.g., Diamond and BN) exhibit an optical phonon more energetic than 150 meV. However, the strong bonds which produce these energetic phonons tend to localize electrons and open a bandgap well over 1 eV. Even in softer semiconductors, the bandgap is typically much larger than the optical phonon energy, as

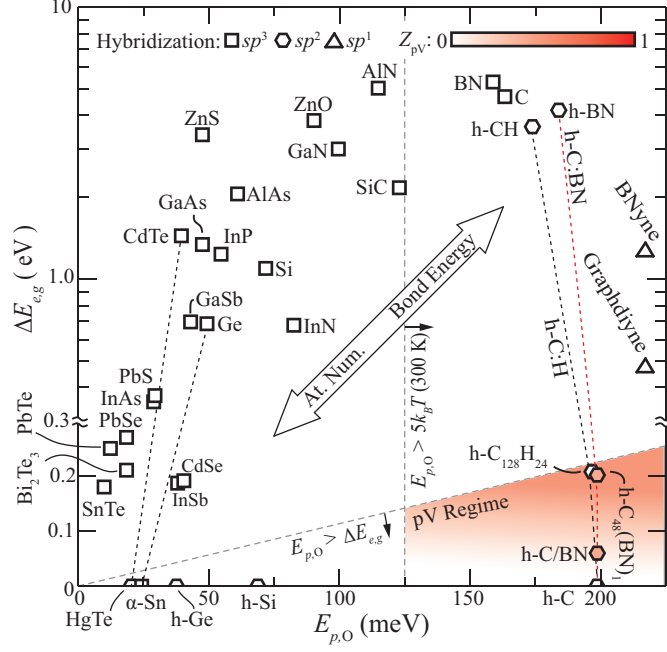


Figure 1.3: The bandgap and optical phonon energy of various semiconductors. An efficient pV requires $E_{p,O} > \Delta E_{e,g} \gg k_B T$, as in tuned graphene. In typical materials at 300 K, however, $\Delta E_{e,g} \gg E_{p,O}$ or $E_{p,O} \approx k_B T$, as the strong bonds which enable energetic phonon modes also localize electrons and open a large bandgap. The symmetry of group IV, sp^2 coordinated materials (e.g., graphene) enables them to overcome this trend. For traditional elemental and composite semiconductors, see [[47, 1, 88]]. For graphane (h-C:H), see [[84, 51]]. For materials with the sp^1 acetylene bond, graphdiyne and BNyne, see [[32, 96]]

shown in Fig. 1.3. Thus, the optical phonons in a typical semiconductor either can not generate electron-hole pairs or can only generate them quickly under cryogenic conditions.

The sp^2 hybridized, group IV semiconductors (e.g., graphene) are a notable exception. In these materials, the symmetry between the two triangular sublattices creates the degenerate Dirac points on the Fermi surface, and no bandgap forms despite the strong sp^2 bonds.[31, 68] Graphene, in particular, has extremely energetic optical phonon modes when compared to most materials, despite its semi-metallic nature. Crucially, there are many methods with which to open a bandgap in graphene, and the e - p coupling dominates the p - p coupling.[7] If the properties of graphene were to remain constant as the bandgap is tuned to the optical phonon energy, its pV figure

of merit could exceed 0.8.[51] No other material candidate surveyed comes close to this promising figure of merit.

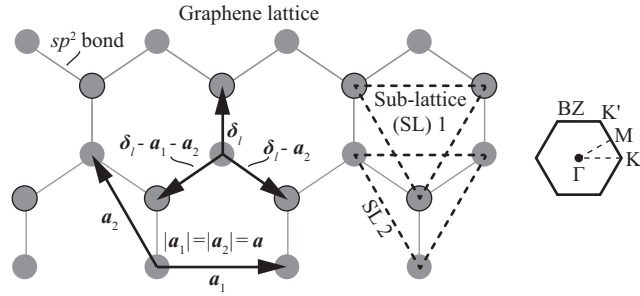


Figure 1.4: (a) The graphene sheet, its geometry, and brillouin zone (BZ). In graphene, the sp^2 hybridized orbitals of carbon atoms form strong bonds with the three nearest neighbors in a hexagonal lattice (defined by two vectors a_1 and a_2 of length a) with two symmetric, triangular sublattices, separated by δ_1 . (b) h-C/BN bilayers. Real bilayers form Moire superlattices rather than an ideally stacked structure due to the small difference in the h-C and h-BN lattice constants.

Opening a bandgap in graphene has attracted substantial attention after its initial discovery. Many methods of achieving this goal have been proposed, e.g., functionalization[21], growth on an ordered substrate[16], and the application of a mechanical strain [66, 27, 63], electric field[61] or magnetic field,[23] or through chemical doping[42]. As chemical doping can substantially shift the Fermi-level in graphene and preclude its use in a diode, and as magnetic fields are often prohibited in electronic devices, the focus is on the remaining methods. The second major thrust of this thesis is to describe the tuning of graphene, the resulting effects on its electron-phonon and phonon-phonon coupling, and evaluate the tuned graphene as a potential pV cell material candidate.

1.4 Statement of objective and scope of thesis

The major objective of this work is to define the phonovoltaic cell and showcase its ability to harvest optical phonons efficiently. Thus, the objectives are to (i) understand and model a pV cell, (ii) derive a physically intuitive efficiency and

figure of merit, (iii) find a suitable material, (iv) evaluate the efficiency of pV cell composed of this material, and (v) describe and evaluate a potential application. The chapters are laid out to follow these objectives in order.

That is, chapter II presents the central mechanism of the pV, the electron-phonon coupling, and a derivation of electron-phonon scattering rate. The additional and crucial scattering mechanisms of optical phonons are also discussed and their interaction rates are derived.

In Chapter III, the function of the pV cell is discussed and its efficiency and material figure of merit are derived. Numerical, hydrodynamic modeling is used to validate these models, and a MC model is used to justify the underlying assumptions of the analytical and numerical models.

Next, Chapter IV presents an investigation of partially hydrogenated graphene as a potential material candidate, and its material properties are evaluated in order to demonstrate that designing the energetics of the material are not sufficient to create an effective material. Instead, both energetics and kinetics are crucial to the function of the pv cell.

In Chapter V, graphene doped with boron nitride (h-C:BN) is shown to reach a large material figure of merit. Moreover, it is shown that graphene can generally succeed as a pV material when its bandgap is tuned through the manipulation of its time-reversal symmetry. A tight-binding model and *ab initio* calculations of graphene on a boron nitride substrate (h-C/BN) presented within are used to support this conclusion.

Then, Chapter VI presents new results on the *ab initio* properties of bilayer graphene under a field, and discusses the possibility of a combined graphene field-effect transistor and phonovoltaic (FET-pV). A full-band Monte Carlo simulation of

the coupled electron and phonon populations in graphene is conducted to show that electric fields can create suitable populations of harvestable optical phonons.

Finally, Chapter VII presents the important results of the work and suggests the future directions for the research.

CHAPTER II

Central Mechanisms of the Phonovoltaic cell

The electron-phonon coupling is central to the operation of the phonovoltaic cell. Indeed, this coupling enables optical phonons to generate electrons. However, the optical phonons also couple with each other, with defects in the lattice, and with electrons in the conduction band, and other energy carriers. These interactions do not contribute to power generation; instead, they contribute to the generation of heat. The goal of this chapter is to develop equations which describe the fraction of optical phonons which relax by generating electrons (and power) rather than acoustic phonons (and heat). To do so, a brief description of the Fermi golden rule is presented. Then, the Fermi golden rule is applied to the interactions between electrons, phonons and other phonons, and phonon and defects in a crystal lattice, as these interactions are important to the operation of a pV.

2.1 Scattering interactions and rates

The four primary carriers can interact with each other and with themselves. In addition to the wave-like interactions like interference or coherence, these carriers interact in a particle-like manner, scattering against each other elastically (no energy transfer) or in-elastically (energy transfer). Often, these interactions are described by a Hamiltonian H' , which gives the energy of that interaction. The Fermi golden

rule, derived from time-dependent perturbation theory, gives the resulting scattering rate

$$(2.1) \quad \dot{g} = \frac{2\pi}{\hbar} |\langle f | H' | i \rangle|^2 \delta(E_f - E_i \pm \hbar\omega),$$

where \hbar is the reduced Planck constant, $|f\rangle$ and $|i\rangle$ are the initial and final states, E_f and E_i are the energy of the initial and final state, and ω is the frequency at which H' oscillates[33]. The Dirac δ function enforces the conservation of energy. In the following sections, the Fermi golden rule is applied to the central carrier interactions in order to derive the kinetics of their scattering. In addition, a Green's function approach is discussed as a better method for calculating the phonon-defect scattering rate. Finally, these equations are used to discuss the fraction of hot optical phonons which relax via the generation of power rather than heat ($\dot{\gamma}_{e-p}^*$).

2.2 Electron-phonon coupling

As a phonon displaces the ions in a crystal, it changes the electric-potential created by those ions and seen by the nearby electrons. Therefore, electrons around the displaced ions can scatter against the perturbed potential and absorb the phonon.[83] The electron-phonon coupling describes this interaction (as well as phonon emission), and Fig 2.1 depicts it. The e - p interaction element which follows from perturbation theory is[2]

$$(2.2) \quad M_{ep,\alpha,i,j}(\mathbf{k}_e, \mathbf{k}_p) = \left(\frac{\hbar}{2m\omega_{\mathbf{k}_p,\alpha}}\right)^{1/2} \langle \mathbf{k}_e + \mathbf{k}_p, j | \frac{\partial \varphi_e}{\partial \mathbf{d}_{\mathbf{k}_p,\alpha}} | \mathbf{k}_e, i \rangle,$$

where i and j are the initial and final band indices, φ_e is the electron potential energy, m is the atomic mass, and $\omega_{\mathbf{k}_p,\alpha}$ and $\mathbf{d}_{\mathbf{k}_p,\alpha}$ are the frequency and atomic displacement pattern of a phonon with momentum \mathbf{k}_p and polarization α . The first group of terms describes the displacement of the phonon mode and the second quantifies the change

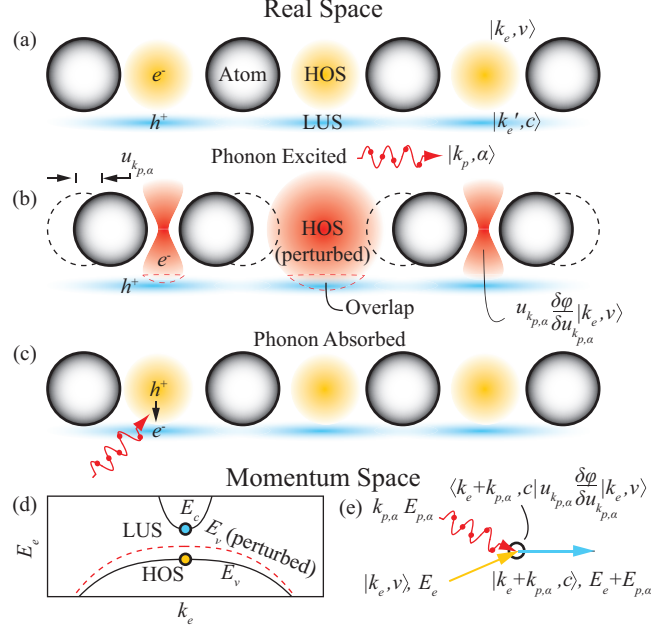


Figure 2.1: The electron-phonon coupling during phonon absorption. (a) The unperturbed system is in equilibrium with an electron in the highest occupied state (HOS, $|\mathbf{k}_e, v\rangle$) and no electron in the lowest unoccupied state (LUS, $|\mathbf{k}_e', c\rangle$). (b) A phonon is excited (\mathbf{k}_p, α), which displaces the atoms by $\mathbf{u}_{\mathbf{k}_p, \alpha}$ and perturbs the HOS, such that it overlaps with the LUS. (c) The electron in the perturbed HOS and excited phonon are annihilated and an electron is created in the highest occupied state, as shown in (c) \mathbf{k}_e space and in (d) the Feynman diagram.

in potential where initial and final electron states overlap. Thus, a strong e - p coupling requires, at minimum, that the valence and conduction states overlap substantially.

The Fermi golden rule (FGR)[33] turns this coupling element into an e - p scattering rate ($\dot{\gamma}_{e-p}$), i.e.,

$$(2.3) \quad \dot{\gamma}_{e-p}^{\pm}(\mathbf{k}_p, \alpha) = \frac{2\pi}{\hbar} \sum_{\mathbf{k}_e, ij} |M_{ep, \alpha, i, j}(\mathbf{k}_e, \pm \mathbf{k}_p)|^2 \delta[E_{e, i}(\mathbf{k}_e) - E_{e, j}(\mathbf{k}_e \pm \mathbf{k}_p) \pm \hbar\omega_{\mathbf{k}_p, \alpha}]$$

$$(2.4) \quad \times [f_{e, i}(\mathbf{k}_e) - f_{e, j}(\mathbf{k}_e \pm \mathbf{k}_p)],$$

where the + (-) indicates absorption (emission), and $E_{e, i}(\mathbf{k}_e)$ and $f_{e, i}(\mathbf{k}_e)$ are the energy and occupation of an electron in band i and with momentum \mathbf{k}_e .

The occupation terms have important consequences. Primarily, if the bandgap is much larger than $k_B T$ and the Fermi level is far from the valence and conduction

band edges, the intraband interactions are substantially reduced by either the lack of conduction electrons [$f_{e,c}(\mathbf{k}_e) \simeq 0$] or by the lack of empty states in the valence band [$f_{e,v}(\mathbf{k}_e) \simeq f_{e,v}(\mathbf{k}_e \pm \mathbf{k}_p) \simeq 1$]. Conversely, if the bandgap is much smaller than $k_B T$ or if doping moves the Fermi level into the conduction or valence bands, the interband interaction is inhibited by the lack of empty states in the conduction band or the lack of electrons in the valence band. Moreover, as the bandgap approaches the optical phonon energy, the number of available energy conserving states approaches zero. Thus, strong interband coupling requires that the bandgap is smaller than the phonon energy and that the phonon energy is substantially larger than $k_B T$, i.e., $E_{p,O} > \Delta E_{e,g} \gg k_B T$. [51]

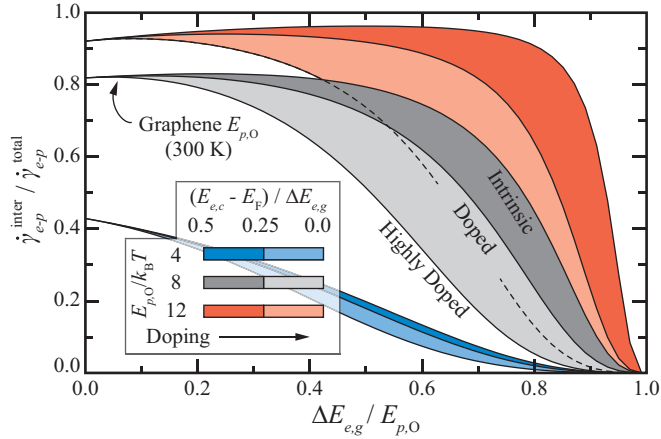


Figure 2.2: The ratio of the interband generation rate to the total rate of optical phonon absorption by electrons in graphene. When the optical phonon energy is much larger than $k_B T$ in an intrinsic semiconductor, the rate of interband generation events dominates the rate of intraband heating events until $\Delta E_{e,g} \rightarrow E_{p,O}$. As the optical phonon energy approaches $k_B T$ or as the Fermi level approaches the conduction band edge ($E_F \rightarrow E_{e,c}$), the interband interactions dominate over a much smaller range of bandgap energies. When $E_{p,O} / k_B T < 5$, the intraband interactions always dominate.

As previously noted, intraband phonon absorption events heat the electron population and do not contribute to power production. Therefore, they can reduce the material figure of merit. However, these events can be neglected, and the summation in Eq. (2.4) is safely restricted to the interband indices, in three instances.

First, intraband scattering events heat the optical phonon population, rather than cooling it. For example, when electrons (holes) are excited into energetic conduction (valence) states by an electric field, they emit optical phonons as they relax, which heats the optical phonon population. In this case, the intraband interactions do not act as a undesirable relaxation pathway. Rather, they act as the source of optical phonons required for pV operation, and the intraband coupling can be substantial without affecting Z_{pV} .

Second, the collection of hot optical phonon modes are limited to momenta which enable energy conservation for inter- but not intraband transitions, such that the intraband interaction rate is zero. For example, only interband e - p interactions occur in graphene when $\mathbf{k}_p < E_{p,O}/(|\nu_e|\hbar)$, where ν_e is the electron Fermi velocity. Conversely, if the interband transition is forbidden by momentum and energy conservation, but the intraband interaction is allowed, then intraband interactions dominate. For example, only intraband interactions occur in graphene when $\mathbf{k}_p > E_{p,O}/(|\nu_e|\hbar)$.

Third, there are substantially more electrons near the valence band edge than there are holes or conduction electrons, i.e., $E_{p,O} > \Delta E_{e,g} \gg k_B T$ and under moderate doping. To quantify this condition, consider a material where the inter- and intraband coupling elements have similar magnitude throughout the Brillouin zone (BZ), i.e., $|M_{ep,\alpha,c,v}| \approx |M_{ep,\alpha,c,c}| \approx |M_{ep,\alpha,v,v}|$, where c and v represent the conduction and valence band indices. Next, assume that the phonon of interest is an optical mode ($\alpha = O$) near the Γ -point with negligible group velocity ($\hbar\omega_{\hbar\mathbf{k}_p,O} \simeq E_{p,O}$ when $\mathbf{k}_p \approx 0$). Further assume that the electron distribution is given by Fermi-Dirac statistics (f_e°) and that the electron density of states (D_e) near valence and conduction band edges are identical. Finally, note that the total scattering rate involves a summation over \mathbf{k}_p as well as \mathbf{k}_e . That is, Eq. (2.4) gives the rate at which a particular

phonon mode (\mathbf{k}_p, α) scatters with all of the electrons, while the total rate considers the scattering of a particular polarization (α) with all of the electrons.

These summations and the δ -function are transformed into an integral over the electron energy using two electron density of state (D_e) functions representing the initial and final density of states. Through this procedure[51], the ratio of inter- to intraband phonon absorption events is quantified as

$$\begin{aligned}
\frac{\hat{\gamma}_{e-p}^{\text{inter}}}{\hat{\gamma}_{e-p}^{\text{intra}}} &= \left\{ \int_0^{E_{p,O} - \Delta E_{e,g}} dE_e D_e(E_{p,O} - \Delta E_{e,g} - E_e) D_e(E_e) \right. \\
&\quad \times [f_e^\circ(-E_e - \Delta E_{F,v}) - f_e(E_{p,O} - \Delta E_{e,g} - E_e + \Delta E_{F,c})] \left. \right\} \\
&\quad / \left\{ \int_0^\infty dE_e D_e(E_e) D_e(E_e + E_{p,O}) \right. \\
&\quad \times [f_e^\circ(E_e + \Delta E_{F,c}) - f_e^\circ(E_e + \Delta E_{F,c} + E_{p,O}) \\
(2.5) \quad &\quad \left. + f_e^\circ(-E_e - E_{p,O} - \Delta E_{F,v}) - f_e^\circ(-E_e - \Delta E_{F,v}) \right\},
\end{aligned}$$

where $\Delta E_{F,v} = E_F - E_{e,v}$ and $\Delta E_{F,c} = E_{e,c} - E_F$ are the energy differences between the valence ($E_{e,v}$) and conduction ($E_{e,c}$) band edges and the Fermi level (E_F). Note that the intraband scattering rate includes both hole and electron contributions.

Figure 2.2 shows the importance of intraband scattering for the dispersionless bands of graphene ($D_e \propto |E_e|$) as predicted by Eq. (2.5). Note that adding dispersion (e.g., $D_e \propto |E_e|^{1/2}$) to the bands increases the density of the low-energy states relative to the high-energy states. Thus, it decreases the relative importance of the intraband scattering events, and Fig. 2.2 provides conservative results.

Despite this, it shows that the interband interactions dominate when $E_{p,O} \gg k_B T$, unless the Fermi level moves extremely close to the band edges or the bandgap approaches the phonon energy. For $E_{p,O}/k_B T < 10$, however, the intraband scattering events begin to compete with generation events. For $E_{p,O}/k_B T < 5$ the intraband scattering events dominate the generation events, regardless of the bandgap or

amount of doping.

In this study, it is assumed that at least one of these three cases hold. Typically, an excited electron population produces the hot optical phonon population as it relaxes. Thus, the first conditions is met. Moreover, the second conditions is always met when the figure of merit is evaluated for a Γ -point phonon, as it is here. Finally, the third condition can be met under certain conditions, even at 300 K, as outlined by Fig. 2.2. Thus, this assumption is typically reasonable.

2.3 Phonon-phonon coupling

The crystal Hamiltonian determines the phonon dynamics and the phonon-phonon couplings, and it is [33, 87]

$$(2.6) \quad \langle \varphi \rangle = \langle \varphi \rangle_o + \frac{1}{2!} \sum_{ijxy} \Gamma_{ij}^{xy} d_i^x d_j^y + \frac{1}{3!} \sum_{ijkxyz} \Psi_{ijk}^{xyz} d_i^x d_j^y d_k^z + \dots,$$

where $\langle \varphi_o \rangle$ is the equilibrium crystal potential, d_i^x is the displacement from equilibrium of atom i in the x (Cartesian) coordinate, and Γ_{ij} and Ψ_{ijk} are the second and third-order force constants.

The second-order interaction determines the phonon dynamics, i.e., the phonon frequencies ($\omega_{\mathbf{k}_p, \alpha}$) and eigenvectors ($\epsilon_{\mathbf{k}_p, \alpha}$), while the anharmonic (third-order and higher) interactions are responsible for the up and downconversion of phonons, the thermal expansion of the lattice, and the temperature dependence of the phonon frequencies.

The p - p coupling which arises from the anharmonicity of the crystal is typically dominated by the three-phonon interactions[14]: up-conversion, where two low-energy phonons combine to create a single high-energy phonon, and down-conversion, where a high-energy phonon scatters with and creates two low-energy phonons. The three-phonon coupling arises from the third-order derivatives of the crystal energy

(Ψ).[87] Thus, the matrix element for the interaction between three phonons is

(2.7)

$$M_{\alpha\alpha'\alpha''}^{\mathbf{k}_p\mathbf{k}'_p\mathbf{k}''_p} = \sum_{ijk} \sum_{xyz} \left(\frac{\hbar}{2m_i m_j m_k \omega_{\mathbf{k}_p, \alpha} \omega_{\mathbf{k}'_p, \alpha'} \omega_{\mathbf{k}''_p, \alpha''}} \right)^{3/2} \Psi_{ijk}^{xyz} \epsilon_{\mathbf{k}_p, \alpha}^{xi} \epsilon_{\mathbf{k}'_p, \alpha'}^{yj} \epsilon_{\mathbf{k}''_p, \alpha''}^{zk} \delta_{\mathbf{k}_p, \mathbf{k}'_p \pm \mathbf{k}''_p},$$

where $\epsilon_{\mathbf{k}_p, \alpha}^{xi}$ is the polarization of the phonon mode in the x direction for atom i , Ψ_{ijk}^{xyz} is the partial derivative of the crystal energy for the displacement of atoms i , j , and k in directions x , y , and z , and the δ -function conserves momentum during up- (−) and down-conversion (+). Note that the dynamical matrix describing the phonon modes arises from the second-order derivatives of the crystal energy.

The rate of down-conversion $[\gamma_{p-p}(\mathbf{k}_p, \alpha)]$ resulting from this interaction follows from the FGR. For a zone-center phonon mode, the FGR gives[28]

$$(2.8) \quad \dot{\gamma}_{p-p}(\Gamma, \alpha) = \frac{2\pi}{N_{\mathbf{k}'_p}} \sum_{\alpha'\alpha''\mathbf{k}'_p} |M_{\alpha\alpha'\alpha''}^{\Gamma\mathbf{k}'_p-\mathbf{k}'_p}|^2 \delta(\omega_{\Gamma, \alpha} - \omega_{\mathbf{k}'_p, \alpha'} - \omega_{\mathbf{k}'_p, \alpha''}) (f'_p + f''_p + 1),$$

where f_p is the phonon occupation. The occupation terms indicate that down-conversion is enhanced the hotter the cell becomes and the less energetic the final states are. Thus, down-conversion is reduced when the optical phonon mode is much more energetic than the thermal energy and, again, $E_{p,O} \gg k_B T$ is desired.

2.4 Phonon-defect coupling

Defects in a crystal, e.g., the B and N atoms in h-C:BN, act as scattering centers for the phonons of the ideal crystal. In general, a defect can have a different mass than the atoms in the ideal crystal, or it can change the interatomic force constants. These variations lead to local changes in the atomic displacement and the frequency of this displacement, creating a scattering center. Moreover, the variations are typically random, rather than ordered, such that the momentum conservation enforced in the e - p and p - p couplings do not apply here. That is, only energy is conserved in the phonon-defect coupling.[34]

The matrix element which arises from a change in mass, e.g., when isotopes are distributed throughout the crystal, is [90]

$$(2.9) \quad M_{p-i,\alpha\alpha'}(\mathbf{k}_p, \mathbf{k}_p') = [x(1-x)\left(\frac{\delta m}{\bar{m}}\right)]^{1/2} \omega_{\mathbf{k}_p,\alpha} \sum_i |\boldsymbol{\epsilon}_{\mathbf{k}_p,\alpha}^{i*} \cdot \boldsymbol{\epsilon}_{\mathbf{k}_p',\alpha'}^i|,$$

where x is the disorder parameter, i.e., the probability an atom at site i has mass $m + \delta m$, and \bar{m} is the average mass. From the FGR, the rate of isotopic scattering becomes

$$(2.10) \quad \dot{\gamma}_{p-i,\alpha}(\mathbf{k}_p) = \frac{\pi}{2N_{\mathbf{k}_p',\alpha'}} \sum_{\mathbf{k}_p',\alpha'} |M_{id,\alpha\alpha'}(\mathbf{k}_p, \mathbf{k}_p')|^2 \delta(\omega_{\mathbf{k}_p,\alpha} - \omega_{\mathbf{k}_p',\alpha'}).$$

However, this interaction element does not account for changes to the inter-atomic force constants, and it is difficult to derive a satisfactory and reasonable matrix element which includes the complete effects a cluster of BN atoms has when substituted into graphene. Thus, instead of the perturbation approach used for the previous scattering mechanisms, a Green's function approach is taken.[91, 90]

In this approach, the phonon spectral function [$A_{\mathbf{k}_p,\alpha}(\omega)$] is evaluated, and its full-width at half-maximum is the scattering rate. The spectral function is given by

$$(2.11) \quad A_{\mathbf{k}_p,\alpha}(\omega) = -\frac{1}{\pi} \text{Im}[G_{\mathbf{k}_p,\alpha}(\omega)]$$

$$(2.12) \quad G_{\mathbf{k}_p,\alpha}(\omega) = \langle \boldsymbol{\epsilon}_{\mathbf{k}_p,\alpha} | \frac{2\omega}{(\omega + i\zeta)^2 - \mathbf{D}} | \boldsymbol{\epsilon}_{\mathbf{k}_p,\alpha} \rangle,$$

where \mathbf{D} is the *ab initio* dynamical matrix of the h-C:BN crystal, $\boldsymbol{\epsilon}_{\mathbf{k}_p,\alpha}$ are the normalized eigenvectors of the dynamical matrix of the ideal graphene crystal, and ζ is a small, positive number.

2.5 Evaluating $\dot{\gamma}_{e-p}^*$

The fraction of hot optical phonons which relax by generating an electron rather than a pair of acoustic phonons ($\dot{\gamma}_{e-p}^*$) follows from the electron-phonon and phonon-phonon scattering rates [Eqs. (2.4) and (2.8)]. While Eq. (2.8) gives the rate at

which an optical phonon mode with $\mathbf{k}_p = \mathbf{0}$ and α ($f_{p,0} = 1$) downconverts, Eq. (2.4) provides only the rate at which that optical phonon mode generates an electron with momentum \mathbf{k}_e in band j . However, after summation over \mathbf{k}_e for $i, j \in c, v$, Eq. (2.4) gives the rate of recombination or generation driven by that optical phonon mode, such that the net generation \dot{n}_e is

$$(2.13) \quad \dot{n}_e(\mathbf{k}_p = \Gamma, \alpha) = \sum_{\mathbf{k}_e} [\dot{\gamma}_{cv}^{(e+p,\alpha)}(\mathbf{k}_e, \mathbf{k}_p = \mathbf{0}) - \dot{\gamma}_{vc}^{(e-p,\alpha)}(\mathbf{k}_e, \mathbf{k}_p = \mathbf{0})].$$

$\dot{\gamma}_{e-p}^*$ follows

$$(2.14) \quad \dot{\gamma}_{e-p}^*(\Gamma, \alpha) = \frac{\dot{n}_e(\Gamma, \alpha)}{\dot{n}_e(\Gamma, \alpha) + \dot{\gamma}_{p-p}(\Gamma, \alpha)} = \frac{\dot{n}_e(\Gamma, \alpha)}{\dot{n}_e(\Gamma, \alpha) + \dot{n}_a(\Gamma, \alpha)},$$

where \dot{n}_a is the net rate of acoustic phonon-pair generation. This quantity limits the quantum efficiency of the pV, i.e., the number of electrons extracted for each optical phonon excited, as discussed in Section 3.3.

CHAPTER III

Phonovoltaic Regime, Efficiency, and Material Figure of Merit

This chapter describes the pV cell. It examines the extent and limits of the pV regime and establishes the potential of the device to surpass the TE efficiency. First, a brief comparison with the TE and PV cells illustrates the unique features of the pV cell, the importance of nonequilibria, and the resulting nanoscale requirement (Section 3.1). Then the central mechanisms of the pV cell, i.e., the electron-phonon and the anharmonic three-phonon coupling, are discussed (Section 4.4). Next, the Boltzmann transport equation (BTE) and its solution via the Monte Carlo simulations illustrate the operation of a pV cell (Section 3.2). An analytical model is developed using the diode equation, a derived net-generation equation, and the resulting heat flow (Section 3.3). Finally, a self-consistent hydrodynamic model incorporating two phonon temperatures validates the analytic model, illuminates additional conditions required for efficient pV operation, and shows that a high Z_{pV} pV outperforms a TE cell (Section 3.4). However, finding a suitable material remains very challenging.

3.1 The phonovoltaic regime and comparison to thermoelectric and photovoltaic cells

Before continuing, it is helpful to clarify the difference between four devices with similar names and some relationship to the pV cell. They are as follows: the thermoelectric (TE), thermovoltaic (TV), phonovoltaic (pV), and photovoltaic (PV) cells. In this section, we discuss these four in order to separate the new device, the pV, from those previously described in the literature.

In a TE cell, electrons diffuse down a temperature gradient in a doped semiconductor to form the Seebeck potential and absorb (release) Peltier heat as they ascend (descend) a potential barrier at the semiconductor-metal junction. Simultaneously, heat conducts down the temperature gradient and generates entropy. Despite this, the efficiency grows with the spatial nonequilibrium across the cell, i.e., the Carnot efficiency (η_C). The TE figure of merit, Z_{TE} , and efficiency, η_{TE} , are

$$(3.1) \quad Z_{TE} = \frac{S^2 \sigma}{\kappa}, \quad \eta_{TE} = \eta_C \frac{(Z_{TE} T + 1)^{1/2} - 1}{(Z_{TE} T + 1)^{1/2} + 1 - \eta_C}, \quad \eta_C = \frac{T_h - T_c}{T_h},$$

where S , σ , and $\kappa = \kappa_e + \kappa_p$ are the Seebeck coefficient and combined electrical and thermal conductivity, and T_c and T_h are the temperature at the cold and hot junctions of the TE cell (assuming $T_e = T_p$)[24, 26]. Importantly, the local thermal equilibrium between the electron and phonon populations in a TE ensures coupled electric and thermal transport (e.g., through the Weidemann-Franz law) and limits Z_{TE} , such that $Z_{TE} T > 1$ and $\eta_{TE} > 0.2\eta_C$ remain challenging to significantly surpass in paired p and n -type TE legs. This limits the application of TE to hostile-environment power generation where reliability supersedes efficiency.

Moreover, TE effectiveness vanishes in nano and microscale devices, where the contact resistance dominates the thermoelectric effects[19, 4, 13, 29]. These factors led to the development of the thermovoltaic (TV) cell by Span *et. al.*[86], wherein

the hot-side p -metal- n junction in a TE is replaced by a p - n junction and electron generation events supply the TE current. They proposed that the TV can slightly exceed the limiting TE efficiency. However, subsequent investigation[92, 11, 5, 10] indicated the TV cell achieves, at most, the TE efficiency.

While the pV and TV share a similar architecture, the pV utilizes a nonequilibrium optical phonon population to drive generation. Indeed, the pV cell shares more features with the photovoltaic (PV) cell than it does with the TE or TV cells. Where TE and TV harvest a flux of equilibrium energy carriers (heat), the PV and pV cells harvest nonequilibrium energy carriers (the photon and phonon, respectively) resonant with or more energetic than the bandgap, as shown in Fig. 1.2. Other nonequilibrium phonon harvesting schemes have received attention for their ability to surpass the TE limits in scale and efficiency. These include the laser cooling of ion-doped materials through anti-Stokes florescence[72, 73], and the use of in-situ electron barriers to recycle phonons emitted during the Joule heating[79, 78]. Conversely, the pV cell focuses on power generation.

Table 3.1: A comparison of thermoelectric (TE), phonovoltaic (pV), and photovoltaic (PV) cells and their controlling processes, where $j_e - \Delta\varphi$ is the current-voltage curve, and other symbols are defined in the text.

Property	TE[24]	pV	PV[45, 33]
Construction			
Size	μm to cm [29]	nm	nm to mm
Junction	p -metal- n	p - n	p - n
Processes			
Energy Source	Heat	Optical Phonon	Photon
Power Generation	Diffusion	Generation	Generation
Entropy Generation nonequilibrium	Conduction Spatial	Downconversion, $E_{p,\text{O}} > \Delta E_{e,g}$ Local: Hot phonon	$E_{ph} > \Delta E_{e,g}$ Local: Hot photon
Performance			
$j_e - \Delta\varphi$	Linear	Exponential	Exponential
Figure of Merit	$S^2 T \sigma / \kappa$ [26]	$\hat{\gamma}_{e-p}^* \Delta E_{e,g} / E_{p,\text{O}}$	-
Quantum Efficiency	-	$\hat{\gamma}_{e-p}^*$	$(E_{ph} < \Delta E_{e,g}) / E_{ph}$
Efficiency	Eq. (3.1)[26]	$F_F \eta_{\text{C}} \hat{\gamma}_{e-p}^* \Delta E_{e,g} / E_{p,\text{O}}$	$F_F \eta_{\text{QE}} \Delta E_{e,g} / E_{ph}$ [48]

Table 3.1 compares the pV cell to TE and PV cells, where F_F is the fill factor, and

E_{ph} is the photon energy. While the TE and pV cells both harvest thermal energy, the pV is more similar to the PV cell, as both harvest a nonequilibrium population in a p - n junction. The major differences arise from the downconversion of optical phonons in a pV, and the transmission of photons with $E_{ph} < \Delta E_{e,g}$ in a PV cell. However, as the local nonequilibrium in a pV vanishes, so does the similarity between pV and PV cells. Instead, as the spatial, thermal nonequilibrium grows larger than the local nonequilibrium, the pV cell becomes more similar to a TV (or TE) cell.

That is, while the generation drives the operation of the pV cell, the generated carriers replace, at most, those diffusing down the temperature gradient. Moreover, despite initially absorbing a single phonon per pair ($E_{p,O}$), the generated electrons relax to a state of thermodynamic equilibrium, and the net energy required is given by the Peltier heat (ST). Finally, heat conduction rather than downconversion drives entropy generation and the efficiency limit approaches that of a TE cell, i.e., Eq. (3.1).

Similarly, when a heat flux is applied to a pV cell, the local nonequilibrium drives up- rather than downconversion. This upconversion supplies the optical phonon population driving electron generation. However, the acoustic phonon population is simultaneously conducting through the device as heat. Indeed, this conduction dominates energy transport in the device: At best, this heat-supplied pV cell achieves the TE efficiency. It reaches this limit when the optical phonon population is in near-equilibrium with the acoustic phonon population (i.e., the optical phonon population is as hot as the energy source) and the rate of electron generation maintains the electron population at near-equilibrium with its energy source, the optical phonon. That is, it behaves like a TV and reaches the TE limit when the local nonequilibrium vanishes. The local nonequilibrium which does develop at the hot-side of this TV

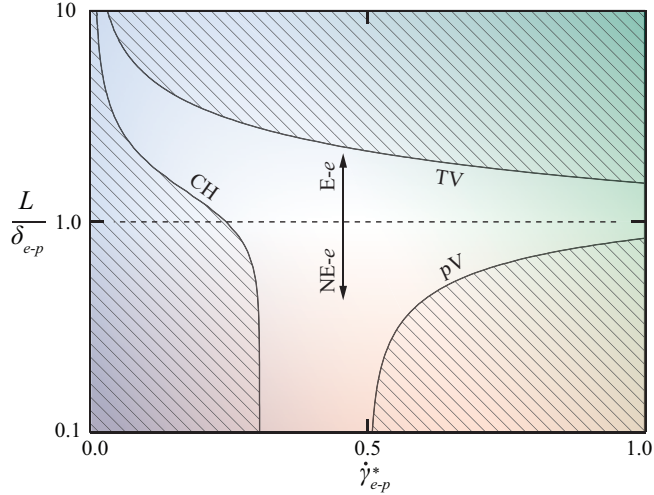


Figure 3.1: Qualitative regimes of a pV cell for variations in L/δ_{e-p} and $\dot{\gamma}_{e-p}^*$. The pV regime requires (i) a device smaller than the electron-phonon cooling length, δ_{e-p} , to sustain a nonequilibrium between the optical phonon and electron populations (NE- e), and (ii) that generation dominates downconversion ($\dot{\gamma}_{e-p}^* > 0.5$). When the local nonequilibrium vanishes (E- e), the pV cell behaves as a TE (TV regime). When generation is much slower than downconversion ($\dot{\gamma}_{e-p}^* < 0.5$), conduction hinders or dominates the device operation (CH regime).

may be understood as analogous to the thermal contact resistance which prevents the hot-side of a TE from being quite as hot as its heat reservoir or the electrical contact resistance which inhibits the diffusion of electrons near the metal-semiconductor junctions.

Therefore, the pV regime requires that a direct excitation of the optical phonon population creates a large, local (rather than spatial) nonequilibrium in the pV cell. Let δ_{e-p} be the electron-phonon cooling length, such that $T_{p,O} - T_e \approx (T_{p,O} - T_c) \exp(-L/\delta_{e-p})$ (the cooling length is on the order 100 nm in a typical semiconductor)[13]. Thus, preserving the local non-equilibrium requires $L/\delta_{e-p} \lll 1$. However, the loss of the local nonequilibrium is compensated by the growth of the spatial nonequilibrium, which drives the thermoelectric effects. Thus, the TE effects replace the pV effects as L/δ_{e-p} grows, such that $L/\delta_{e-p} = 1$ demarcates a qualitative boundary between the TE and pV regimes.

An efficient pV cell also requires $\dot{\gamma}_{e-p}^* > 0.5$, as small $\dot{\gamma}_{e-p}^*$ precludes efficient pV operation. Moreover, small $\dot{\gamma}_{e-p}^*$ indicates that the phonon-phonon nonequilibrium vanishes before the electron-phonon nonequilibrium, such that the pV cell achieves the TE limit most quickly as $\dot{\gamma}_{e-p}^* \rightarrow 1$. Thus, the third, conduction hindered (CH) region is defined by the $\dot{\gamma}_{e-p}^* \rightarrow 0$ and the $L/\delta_{e-p} \rightarrow 0$, where the downconversion of optical into acoustic phonons dominates energy conversion, generating entropy rather than power.

It is beyond the scope of this section to present the quantitative TV and CH regimes. However, Fig. 3.1 qualitatively illustrates the three regimes: The pV regime, where a hot optical phonon population relaxes primarily by generating electrons [$\dot{\gamma}_{e-p}^* \exp(-L/\delta_{e-p}) > 0.5$]; the TV regime, where the local nonequilibrium vanishes [$1 - \exp(-\dot{\gamma}_{e-p}^* L/\delta_{e-p}) > 0.9$]; and the conduction hindered (CH) regime, where generation cannot supply the TE current (limiting the TV regime) or is dominated by downconversion (limiting the pV regime) [$\exp(-\dot{\gamma}_{e-p}^* L/\delta_{e-p}) - \dot{\gamma}_{e-p}^* \exp(-L/\delta_{e-p}) > 0.7$]. Note that these contours have been chosen following the preceding discussion and to describe a pV cell which operates most efficiently in the pV rather than the TE regime. Still, it is primarily qualitative rather than quantitative.

3.2 Non-equilibrium in the phonovoltaic cell

Before attempting to model the pV cell, it is important to understand its nonequilibrium. Indeed, the nanoscale pV cell can exhibit several forms of it, including the local nonequilibrium between electron and phonon populations driving the net generation of electrons, the local nonequilibrium between optical and acoustic phonon populations driving the net downconversion of optical phonons, and the local nonequilibrium within the electron system which affects transport. Moreover, when the device

is sufficiently long, a spatial nonequilibrium grows within these populations and the aforementioned local nonequilibria may vanish, as discussed in Sec. 3.1. Thus, the investigation of a pV cell begins with the Boltzmann transport equation (BTE), which models spectral transport of an energy carrier (i) with momentum \mathbf{p} through its occupancy $f_i(\mathbf{p})$. As such, it demonstrates the role of the electron-electron nonequilibrium and spatial nonequilibrium within a pV cell.

The electron BTE, $i = e$, is[33]

$$(3.2) \quad \frac{\partial f_e}{\partial t} + \mathbf{u}_e \cdot (\nabla_{\mathbf{x}} f_e) + -e_c \nabla_{\mathbf{x}} \varphi_e \cdot \nabla_{\mathbf{p}} f_e = \frac{\partial f_e}{\partial t} \Big|_s + \dot{s} \approx \dot{\gamma}_e (f_e - f_e^\circ) + \dot{s}_e,$$

where the terms, in order, describes transient effects, the free flight of electrons with velocity \mathbf{u}_e , the acceleration by an electric field (where φ_e is the electric potential and e_c the electron charge), the in- and out-scattering of electrons at location \mathbf{x} , and the generation (\dot{s}_e) of new electrons with momentum \mathbf{p} . The scattering term is often approximated through the RTA, where f_e° is the equilibrium occupancy and $\dot{\gamma}_e$ is the total scattering rate. This approximation assumes that there is near equilibrium within the electron population, and it enables the integration of the BTE for various device level models.

Furthermore, the RTA provides the average distance between electron collisions (mean free path), $\lambda_e = u_F / \langle \dot{\gamma}_e \rangle$, where u_F is the Fermi velocity and $\langle \dot{\gamma}_e \rangle$ is the average electron scattering rate. When the device is very small compared to the mean free path ($L \ll \lambda_e$), the transport is ballistic and generated electrons are harvested without relaxing. For $L \gg \lambda_e$, the transport is diffusive, electron distributions are near equilibrium ($f_e \simeq f_e^\circ$), and the RTA is valid. This section presents an ensemble Monte-Carlo (MC) simulation of the BTE in order to investigate the electron population in the active region of a pV cell and to describe the electron transport in a pV cell.

The MC method statistically solves the BTE by simulating many electron superparticles freely-accelerating between electron-phonon scattering events. The time between scattering events and the scattering event which occurs are chosen statistically while preserving the kinetics of the system,[44] as discussed in Appendix B.

Here, only the scattering of electron with the optical and acoustic phonon population is considered. Furthermore, the kinetics within the MC model assume isotropic, parabolic bands and a constant electron-phonon coupling element [$M_{cc}^{e-p,\alpha}(\mathbf{k}_e, \mathbf{k}_p) = M_{p,\alpha}$] near the band-edge. Consider Eq. (2.4) integrated over \mathbf{k}_p from the perspective of conduction electron with momentum \mathbf{k}_e in a non-degenerate semiconductor ($f_{e,c,\mathbf{k}_e} = 1$ and $f_{e,c,\mathbf{k}_e \pm \mathbf{k}_e} = 0$). For a dispersionless optical phonon, this gives

$$\begin{aligned}
\dot{\gamma}_{cc}^{(e\pm p,O)}(\mathbf{k}_e) &= \sum_{\mathbf{k}_p} \dot{\gamma}_{cc}^{(e\pm p,O)}(\mathbf{k}_e, \mathbf{k}_p) \\
(3.3) \qquad \qquad \qquad &= \frac{2\pi}{\hbar} |M_{p,O}|^2 D_e(E_{e,\mathbf{k}_e} \pm E_{p,O}) \left(\frac{1}{2} \mp \frac{1}{2} + f_{p,O} \right),
\end{aligned}$$

where the density of states and electron dispersion are

$$(3.4) \qquad \qquad \qquad D_e(E_e) = \sum_{\mathbf{k}_p} \delta_e(E_e) = \left(\frac{m_{e,e}}{\hbar^2} \right)^{3/2} E_e^{1/2}$$

$$(3.5) \qquad \qquad \qquad E_{e,\mathbf{k}_e} = \frac{\hbar^2 |\mathbf{k}_e|^2}{2m_{e,e}},$$

and $m_{e,e}$ is the effective mass of a conduction band electron.

The scattering rate of an electron with an acoustic phonon of constant speed $u_{p,A}$ gives a similar result, only with a different phonon energy ($E_{p,A} = \hbar |\mathbf{k}_p| u_{p,A}$ rather

than $E_{p,O}$). This energy must conserve energy and momentum, i.e., we require

$$\begin{aligned}
E_{e,\mathbf{k}_e+\mathbf{k}_p} &= E_{e,\mathbf{k}_e} \pm E_{p,A} \\
\frac{\hbar^2(k_e + k_p)^2}{2m_{e,e}} &= \frac{\hbar^2 k_e^2}{2m_{e,e}} \pm u_{p,A} \hbar k_p \\
\text{s.t.} \quad k_p &= 2\left(\pm \frac{m_{e,e} u_{p,A}}{\hbar} - k_e\right) \\
(3.6) \quad \text{and} \quad E_{p,A} &= 2u_{p,A}(\pm k_e m_{e,e} u_{p,A} - \hbar k_e),
\end{aligned}$$

where $k_i = |\mathbf{k}_i|$ and the $k_{p,A} = 0$ solution does not represent a scattering event. The MC model does not treat the acoustic phonon scattering as elastic, but uses the above equations to determine the final state.

Additionally, a fast generation rate (\dot{s}_e) is prescribed in the active region and the energetic optical phonon is given a hot temperature ($T_{p,O,h}$). The remaining optical and acoustic phonon modes are given a cold temperature equal to the contact temperature, T_c .

As ensemble MC simulates thousands of electrons in one superparticle, less than one superparticles is typically generated or annihilated within a single time step (1 fs) in a particular location bin (0.5 nm). This MC model carries the remainder from one time step to the next, such that over many time steps the number of generated superparticles accurately represents the number of generated electrons. New electrons are given an initial energy through the implicit solution of

$$(3.7) \quad r \int_0^\infty D_e(E_e) D_e(E_e - E_{p,O}) dE_e = \int_0^{E_e} D_e(E_e - E_{p,O}) dE_e,$$

for E_e , where r is a uniformly distributed random number and $D_e(E_e) D_e(E_e - E_{p,O})$ is proportional to the net-generation rate. (See Section 3.3.A.) The initial momentum direction is randomized in the isotropic semiconductor. A typical Ohmic contact is modeled at $x = 0$, and electrons are reflected at $x = L/2$, where L is the length of the

Table 3.2: Material and parameters used in the MC simulations, where m_e is the electron mass. Parameters are chosen to represent partially-hydrogenated graphite.

MC Parameters			
$m_{e,e}$	$0.01 m_e$	$\Delta E_{e,g}$	150 meV
$E_{p,O,1}$	198 meV	$E_{p,O,2}$	154 meV
$ M_{p,O} _1$	140 meV	$ M_{p,O} _2$	110 meV
$u_{p,A}$	1000 m/s	$ M_{p,A} $	50 meV
L_a	$1/5L$	\dot{s}_e	$0.1/L \text{ nm-cm}^{-3}\text{ps}^{-1}$
T_c	300 K	$T_{p,O,h}$	600 K

cell, to represent an ideal junction under short-circuit conditions. This is illustrated in Fig. 3.2.

The MC simulations of the PV cell are run for the material parameters listed in Table 3.2. These parameters are similar to those of a tuned graphene[51, 53]. Note that the generation rate is proportional to the cell length. This ensures that in a long cell with $L \gg \lambda_e$, i.e., the diffusive regime, the change in the carrier concentration is independent of L . This simulation does not accurately track or predict the cell performance, as it is not self-consistent. However, it determines the extent of the electron relaxation and the transport regime (ballistic or diffusive) for the generated electrons as a function of L . Most importantly, it illustrates the operation of a pV cell.

Results

Figure 3.2 shows the spatial distribution of the (a) electron density and (b) temperature and (c) the local distribution electron energy for variations in the cell length. Electrons are generated within a small active region near the junction. The junction reflects all electrons, forcing electrons towards collection at the contact. Note the concentration gradient formed in the short cell is half of that formed in the long cell. Indeed, the concentration gradient required to drive the generated electrons out of the cell is reduced as L approaches λ_e and the transport regime becomes ballistic.

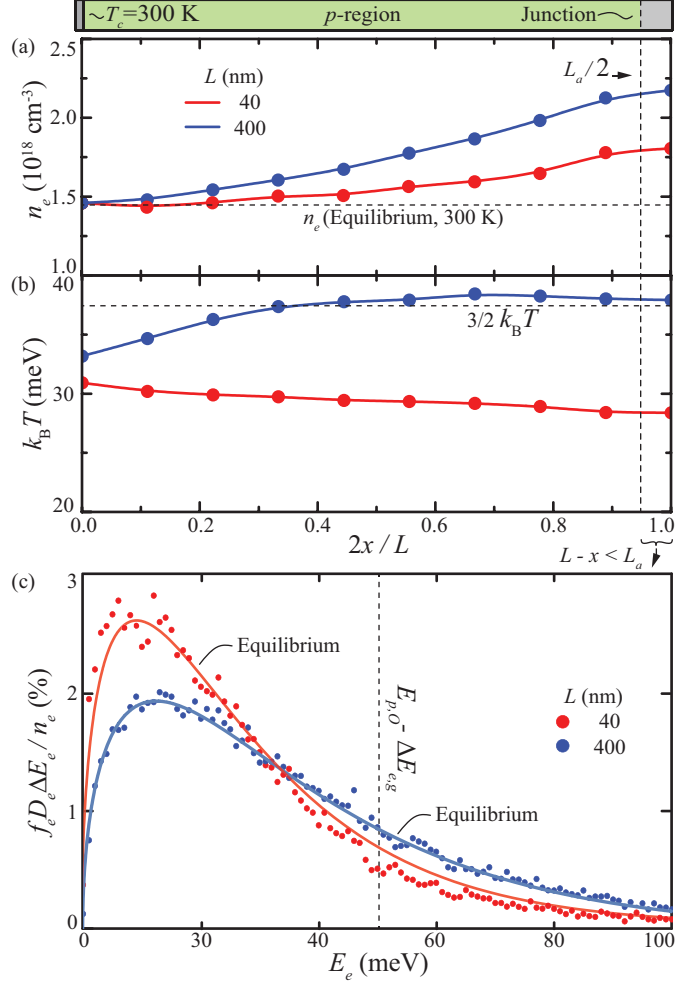


Figure 3.2: Spatial distributions of the (a) Electron density and (b) temperature, and (c) local energy distributions within the active region in 400 and 40 nm pV cells. The generation rates are scaled by $1/L$ to demonstrate that transport is partially ballistic in the 40 nm cell. The generation of cold electrons reduces the average energy of the population, but the nonequilibrium within the electron population remains small. The 400 nm cell, in comparison, exhibits diffusive transport, a negligible change in the electron temperature, and equilibrium occupancy within the electron population.

Additionally, as these electrons have a smaller kinetic energy than the thermal average, $3k_B T_c/2$, they cool the cell. However, the hot optical phonon population also heats the electron population through intraband interactions. In the short cell, the cooling effect dominates, while in the long cell, the two effects balance. In sufficiently long cell, intraband interactions should overcome the cooling and induce a spatial non-equilibrium. Regardless, the electron population in both the 40 and 400 nm cells

remains near the equilibrium distribution. Indeed, the RTA remains valid, even as the electron transport becomes ballistic.

In the following sections, macroscale models use the RTA to take moments of the electron BTE. While the MC results support this approach, there are restrictions to its validity. Primarily, at lower temperatures the mean free path grows substantially. Moreover, under an applied voltage, a significant number of electrons flow over the junction, gain a large kinetic energy, and these hot electrons are in nonequilibrium with the cold electron population. However, the mean free path of these hot electrons is relatively short. In general, the RTA and the resulting moments of the BTE remain valid.

3.3 Analytic efficiency and figure of merit

With the local nonequilibria limited to the electron-phonon and optical-acoustic phonon populations, a simple analytical model is developed in order to achieve the following goals: *(i)* develop a figure of merit, *(ii)* determine the temperature dependence of the pV cell, and *(iii)* provide accurate predictions and fundamental insights.

The ratio of the power produced ($P_e = J_e \varphi_a$, where J_e is the current extracted across a potential φ_a) to the heat flow applied (Q_{in}) determines the pV efficiency ($\eta_{pV} = P_e/Q_{in}$). In an ideal junction (i.e., one with no excess current loss, e.g., that from surface recombination or junction tunneling) with negligible internal resistance, the current produced is proportional to the net-generation (\dot{n}_e) within the cell volume (V), i.e., $J_e = e_c \dot{n}_e V$. The energy flow required to produce this current is $Q_e = E_{p,O} J_e$. However, additional heat flows from the hot optical phonon population into the acoustic branches due to the net-downconversion rate ($\dot{n}_{p,A}$) within the cell volume,

such that $Q_{p,A} = E_{p,O}\dot{n}_{p,A}V$. Assuming the interband electron-phonon and phonon-phonon interactions dominate the optical phonon lifetime, the controlling equations become

$$(3.8) \quad P_e = J_e\varphi_a = e_c\dot{n}_eV\varphi_a$$

$$(3.9) \quad Q_{in} = Q_e + Q_{p,A} = E_{p,O}(\dot{n}_e + \dot{n}_a)$$

$$(3.10) \quad \eta_{pV} = \frac{P_e}{Q_{in}} = \frac{e_c\varphi_a}{E_{p,O}} \frac{\dot{n}_e}{\dot{n}_e + \dot{n}_a}.$$

Thus, determining the efficiency and power output of a pV cell requires the relationship between the current (or net-generation) and voltage.

Before deriving a model for this relationship, consider the diode equation

$$(3.11) \quad J_e(\varphi_a) = J_o - J_d(\varphi_a),$$

where $J_o = J_e(0)$ is the short-circuit current and J_d is the dark, adverse current driven across the junction by a potential (or, alternatively, the net-recombination driven by the potential induced difference in electron and hole Fermi-levels). In an open-circuit, no current leaves the cell ($J_e = 0$). Instead, the potential develops within the cell until it reaches the open-circuit voltage ($\Delta\varphi_{oc}$) and the dark current balances with the short-circuit current generated by the hot optical phonon population.

Note that short-circuiting the pV cell ($\varphi_a = 0$) and maximizing the current, or open-circuiting the cell ($J_e = 0$) and maximizing the voltage generates no power. The maximum power and maximum efficiency conditions reside between these limits. The fill-factor (F_F) quantifies the fraction of power achieved by a diode to the product of the short-circuit current and open-circuit voltage, i.e.,

$$(3.12) \quad F_F = \frac{P_e}{J_o\Delta\varphi_{oc}}.$$

The fill-factor is limited to between 1/4 and 1, where the former requires a linear current-voltage curve and the latter requires a square curve. Next, analytic equations for the current-voltage relationship of an ideal pV cell and the resulting performance are derived.

3.3.1 Net generation

The electron-phonon interband interaction falls into the class of band-to-band recombination and generation events, which also includes radiative decay. A band-to-band recombination rate ($\dot{n}_{e,b-b}$) depends on the number of conduction electrons (n_e) which can recombine and the number of empty valence states, i.e., holes (n_h), with which they can recombine. Thus, the generation or recombination rate is expected to be proportional $n_e n_h$. Noting that no net recombination occurs under equilibrium, when $n_e n_h = n_i^2$ and n_i is the intrinsic electron and hole concentration. Thus, the net band-to-band recombination rate is

$$(3.13) \quad \dot{n}_{e,b-b} = a_{b-b}(n_e n_h - n_i^2),$$

where a_{b-b} is a coefficient which depends on the interaction. We show below that the net rate of generation due to the electron-phonon interaction exhibits a similar form when derived from the *ab initio* rate [Eq. (2.4)].

Consider Eq. (2.4), integrated over \mathbf{k}_p for a dispersionless optical phonon ($\hbar\omega_{\mathbf{k}_p,0} = E_{p,0}$) with a constant interaction strength for generation [$M_g = M_{vc}^{(e+p,0)}(\mathbf{k}_e, \mathbf{k}_p)$] and recombination [$M_r = M_{cv}^{(e-p,0)}(\mathbf{k}_e, \mathbf{k}_p)$] events. Further, assume there is equilibrium within the electron, hole, and optical phonon populations and thermal equilibrium between the electron and hole populations. Finally, assume a non-degenerate semiconductor where Maxwellian statistics hold, i.e., the population of the the electron

($i = e$), hole ($i = h$) and phonon ($i = p$) are

$$(3.14) \quad f_i(E_i, T) = \exp\left(\frac{E_{F,i} - E_i}{k_B T}\right) \ll 1,$$

where E_i and T are the population energy and temperature, and $E_{F,i}$ is the Fermi energy ($E_{F,p} = 0$).

Under these assumptions, the generation [$\dot{\gamma}_{e-p,g}(E_e)$] and recombination [$\dot{\gamma}_{e-p,r}(E_e)$] rates for an electron at initial energy E_e are

$$(3.15) \quad \begin{aligned} \dot{\gamma}_{e-p,g}(E_e) &= a_{e-p,g} \int d\mathbf{k}_p \delta_E(E_e - E'_e + E_{p,O}) f_{p,O}(E_{p,O}, T_{p,O}) \\ \dot{\gamma}_{e-p,r}(E_e) &= a_{e-p,r} \int d\mathbf{k}_p \delta_E(E_e - E'_e - E_{p,O}) f_e(E_i, T) f_h(E_f, T), \end{aligned}$$

where $a_{e-p,i} = \pi \hbar |M_i|^2 / (E_{p,O} \langle m \rangle)$. Using the definition of the density of states, $D_i(E_i) = \int d\mathbf{k}_p \delta_E(E_i)$, reduces the rates to

$$(3.16) \quad \begin{aligned} \dot{\gamma}_{e-p,g}(E_h) &= a_{e-p,g} D_e(E_{f,h}) f_{p,O}(E_{p,O}, T_{p,O}) \\ \dot{\gamma}_{e-p,r}(E_e) &= a_{e-p,r} D_h(E_{f,i}) f_{eh}(E_{p,O}, T_{p,O}), \end{aligned}$$

where f_{eh} uses the differences in Fermi energy $E_{F,eh} = \Delta E_F = E_{F,e} - E_{F,h}$, and $E_{f,i} = E_{p,O} - \Delta E_{e,g} - E_i$.

Integrating over the allowed electronic states gives the total rate of generation ($\dot{n}_{e,g}$) and recombination ($\dot{n}_{e,r}$). Let \mathcal{D} be the integral of $D_e(E_e) D_h(E_{f,e})$ over $0 \leq E_e \leq E_{p,O} - \Delta E_{e,g}$ and $E_h = E_{p,O} - \Delta E_{e,g} - E_e$, then the net rate of generation is

$$(3.17) \quad \dot{n}_e = \dot{n}_{e,g} - \dot{n}_{e,r} = a_{e-p,g} \mathcal{D} f_{p,O}(E_{p,O}, T_{p,O}) - a_{e-p,r} \mathcal{D} f_{eh}(E_{p,O}, T).$$

As the net generation must vanish under equilibrium ($T_{p,O} = T$), we require $a_{e-p,g} = a_{e-p,r}$.

This model, like the band-to-band model, is driven by the temperature difference $T_{p,O} - T$. However, the population terms $f_{p,O}(E_{p,O}, T_{p,O}) - f_{eh}(E_{p,O}, T)$ rely on $E_{p,O}$

rather than $\Delta E_{e,g}$, as in the band-to-band model ($\dot{n}_{e,b-b}$), i.e.,

$$(3.18) \quad \dot{n}_{e,b-b} \propto \left[\exp\left(-\frac{\Delta E_{e,g}}{k_B T_{p,O}}\right) - \exp\left(-\frac{\Delta E_{e,g} - \Delta E_F}{k_B T}\right) \right]$$

$$(3.19) \quad \dot{n}_e \propto \left[\exp\left(-\frac{E_{p,O}}{k_B T_{p,O}}\right) - \exp\left(-\frac{E_{p,O} - \Delta E_F}{k_B T}\right) \right].$$

This difference leads to a substantial divergence in the predicted behavior, and most notably, the open-circuit voltage. Noting that the $\Delta E_F = e_c \varphi_a$ under the current assumptions, i.e., negligible internal resistance in an ideal junction, the open-circuit voltage [$\dot{n}_e(\Delta E_F = e_c \Delta \varphi_{oc}) = 0$] is

$$(3.20) \quad \Delta \varphi_{oc,b-b} = \eta_C \Delta E_{e,g} / e_c$$

$$(3.21) \quad \Delta \varphi_{oc} = \eta_C E_{p,O} / e_c,$$

where $\eta_C = 1 - T/T_{p,O}$.

Typically, the open-circuit voltage in a photovoltaic cell is limited by the bandgap[82] rather than the photon energy. While it has been proposed that harvesting electrons before they relax enhances the open-circuit voltage[60], this has not been realized experimentally. In a pV cell, a similar phenomena is expected, where the relaxation of the generated carriers towards the bandedge ensures the same, bandgap-limited behavior. Therefore, the analytical model uses the band-to-band model for net-generation.

3.3.2 Current-voltage curve

As previously discussed, the current-voltage relationship is proportional to the net-generation, i.e.,

$$(3.22) \quad J_e(\varphi_a) = e_c V_a \dot{n}_e = e_c V_a a_{e-p,b-b} \left[\exp\left(-\frac{\Delta E_{e,g}}{k_B T_{p,O}}\right) - \exp\left(-\frac{\Delta E_{e,g} - \varphi_a}{k_B T}\right) \right],$$

where $a_{e-p,b-b}$ ensures that the short-circuit band-to-band current matches the derived model in Eq. (3.17). The maximum power (P_m) and the corresponding voltage

$(\Delta\varphi_m)$ are found by maximizing $P_e(\varphi_a) = J_e(\varphi_a)\varphi_a$. The maximization gives

$$(3.23) \quad \Delta\varphi_m = \frac{k_B T}{e_c} \{W[\exp(1 + \frac{\Delta\varphi_{oc}}{k_B T})]\}$$

where $W(z)$ is the principle solution for w in $z = we^w$ and $\lim_{x \rightarrow \infty} W[\exp(1 + x)] = x$. That is, as the open-circuit voltage grows large in comparison to $k_B T$, the $\Delta\varphi_m$ approaches the open-circuit voltage. Intuitively, this also implies the current (J_m) approaches the short-circuit current and the Fill-Factor approaches unity under the same condition. While the expressions for J_m and P_m becomes progressively more complicated and less insightful, numerical investigation confirms this. Indeed, the fill-factor expression corresponding to the maximized power condition is well approximated by

$$(3.24) \quad F_F = \frac{J_m \Delta\varphi_m}{J_o \Delta\varphi_{oc}} \simeq 1 - \frac{3}{4} \exp(-0.1\eta_C \Delta E_{e,g}^*) \text{ for } \eta_C \Delta E_{e,g}^* < 10,$$

where $\Delta E_{e,g}^* = \Delta E_{e,g}/k_B T$ and the limits $1/4 \leq F_F \leq 1$ are reproduced, and this equation confirms these suppositions.

3.3.3 Efficiency

From Eq. (3.20), the fraction of the optical phonon energy achieved by the pV cell in an open-circuit is

$$(3.25) \quad \eta_\varphi = \frac{e_c \Delta\varphi_{oc}}{E_{p,O}} = \eta_C \frac{\Delta E_{e,g}}{E_{p,O}}.$$

Additionally, the number of electrons extracted per optical phonon (quantum-efficiency) follows from Eqs. (3.9) and (3.22)

$$(3.26) \quad \eta_{QE} = \frac{J_o}{J_{p,O}} = \frac{e_c V_a \dot{n}_e}{e_c V_a (\dot{n}_e + \dot{n}_a)} = \frac{\dot{n}_e}{(\dot{n}_e + \dot{n}_a)} = \dot{\gamma}_{e-p}^*$$

where $\dot{\gamma}_{e-p}^*$ is the fraction of optical phonon scattering events which result in the generation of an electron [from Eq. (2.14)]. Thus, the efficiency for a square current-

voltage curve ($F_F = 1$) is

$$(3.27) \quad \eta_{\text{pV,max}} = \eta_C \dot{\gamma}_{e-p}^* \frac{\Delta E_{e,g}}{E_{p,O}} = \eta_C Z_{\text{pV}},$$

where $Z_{\text{pV}} = \dot{\gamma}_{e-p}^* \Delta E_{e,g} / E_{p,O}$ is the pV figure of merit.

Unfortunately, the analytic expressions for the maximum efficiency condition is much more complicated than the already complex expressions for $\Delta\varphi_m$ and P_m . Thus, a realistic and maximized analytic efficiency offers little insight. However, consider the following conservative procedure to derive an analytic and insightful efficiency relation (η_{pV}).

The maximum heat flow required by a pV cell occurs in the short-circuit condition, where \dot{n}_e is maximized. Assuming Q_{in} does not strongly depend on φ_a and remains near this limit, we can derive a useful relation. If Q_{in} does not depend on φ_a , then the maximum power and efficiency conditions coincide. Thus,

$$(3.28) \quad \eta_{\text{pV}} = \eta_C Z_{\text{pV}} F_F \simeq \eta_C Z_{\text{pV}} \left[1 - \frac{3}{4} \exp(-0.1 \eta_C \Delta E_{e,g}^*) \right],$$

where F_F is approximated as in Eq. (3.24).

Assuming a constant Q_{in} presumes that either $\dot{\gamma}_{e-p}^* \rightarrow 0$ or $F_F \rightarrow 1$ ($\eta_C \Delta E_{e,g}^* \rightarrow 1$). For large $\dot{\gamma}_{e-p}^*$ and small F_F , the heat decreases quickly with increasing φ_a (and decreasing J_e). In this case, the maximum efficiency and power conditions diverge, and the maximum efficiency increases significantly over Eq. (3.28). A parameterized investigation of Eq. (3.28) and its implications follows, and in the next section we look at the divergence of this relation from the results of a relaxed, hydrodynamic model.

3.3.4 Results

Figure 3.3 depicts Eq. (3.28), showing η_{pV}/η_C for variations in Z_{pV} and $\eta_C \Delta E_{e,g}^*$. In order to surpass η_{TE} , a pV must achieve $\eta_C \Delta E_{e,g}^* > 1$, unless $Z_{\text{TE}} T > 0.7$. Thus,

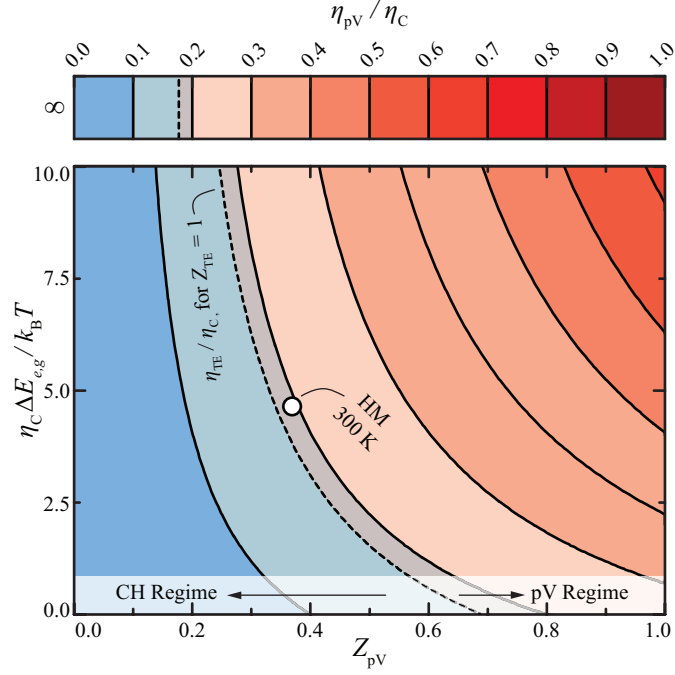


Figure 3.3: The pV efficiency as a function of the nonequilibrium, $\eta_C \Delta E_{e,g} / k_B T_c$, and the pV figure of merit, Z_{pV} [Eq. (3.28)]. Significant nonequilibrium is required to outperform a TE with $Z_{TE} T = 1$, unless the figure of merit exceeds 0.7. When T_c vanishes, the pV cell achieves $\eta_{pV} = \eta_C Z_{pV} \leq 1$. When $Z_{pV} \rightarrow 0$, the efficiency vanishes, and when $\eta_C \rightarrow 0$, the efficiency approaches $0.25 \eta_C Z_{pV}$. The hydrodynamic model (HM) simulations use a standard set of parameters slightly exceeding the TE cell.

an efficient pV cell requires either an optical phonon resonant with its bandgap and a linewidth dominated by the electron-phonon coupling, or it requires extreme nonequilibrium and a bandgap significantly more energetic than the thermal energy. That is, unless Z_{pV} is large, the pV is limited to low-temperature operation. However, if the Z_{pV} and nonequilibrium are large, the pV cell approaches the Carnot limit.

3.4 Hydrodynamic efficiency and operation

The analytical model requires a number of assumptions including fast transport and no surface recombination ($\eta_{QE} = \hat{\gamma}_{e-p}^*$). A numerical, hydrodynamic model (given in Appendix A) is used to validate Eq. (3.28), relax its assumptions, and reveal additional cell parameters which influence the pV efficiency. The hydrodynamic model considers the same nonequilibria as the analytic model, i.e., local $e-p$

and p - p nonequilibria, but adds the spatial nonequilibria within electron and phonon populations. It takes the first three moments of the electron BTE (continuity, momentum, energy), includes the conduction of optical and acoustic phonons, and uses the Poisson equation to ensure self-consistency.

Table 3.3: Material and parameters used in hydrodynamic model simulations at $T_c = 300$ K. Parameters are chosen to represent a hydrogenated graphite pV cell. Parameters are defined in Appendix A.

Figure of Merit			
$E_{p,O}$	198 meV	$\Delta E_{e,g}$	150 meV
a_{e-p}	$20 \text{ cm}^{-9} \text{ s}^{-1}$	a_{p-p}	$20 \text{ cm}^{-9} \text{ s}^{-1}$
$\tau_{e-p,E}$	20 ps	$\Delta E_{e,g}/E_{p,O}$	0.75
$\hat{\gamma}_{e-p}^*$	0.5	Z_{pV}	0.38
Transport			
$n_{e,v}$	$7.1 \times 10^{18} \text{ cm}^{-3}$	$n_{e,c}$	$7.1 \times 10^{18} \text{ cm}^{-3}$
μ_e	$0.2 \text{ m}^2/\text{V-s}$	ϵ_e	12
$\kappa_{p,A}$	0.3 W/m-K	$\kappa_{p,O}$	0.001 W/m-K
Cell			
L	50 nm	L_a	10 nm
η_C	2/3	$\Delta E_{F,p-n}$	150 meV
SR	w/o		

This section uses the parameters baseline given in Table 3.3, and then varies important parameters from among this collection to investigate their effects. The parameters are chosen to reflect a functionalized graphene material utilizing its E_{2g} optical phonon mode. The Z_{pV} is chosen to examine a moderate pV material which requires significant nonequilibrium to surpass a TE cell. Parameters are varied to both validate the analytic model, examine what is required for such a material to surpass the TE limit, and investigate pV cell operation under extreme nonequilibrium.

The length (L) is sufficiently small and the transport of the electron (μ_e), hole (μ_h), and acoustic phonon ($\kappa_{p,A}$) are sufficiently fast to ensure that these populations do not equilibrate with the optical phonon mode (limited spatial nonequilibrium). As long as this condition is satisfied (i.e., $L \gg \delta_{p-p} \simeq \delta_{e-p}$, where δ_{e-p} is the electron cooling length), the pV behavior is independent of these parameters. However, the slow optical phonon transport ($\kappa_{p,O}$) influences pV efficiency when $L_a/L < 1$, as it restricts the hot optical phonon population to the active region. In the standard

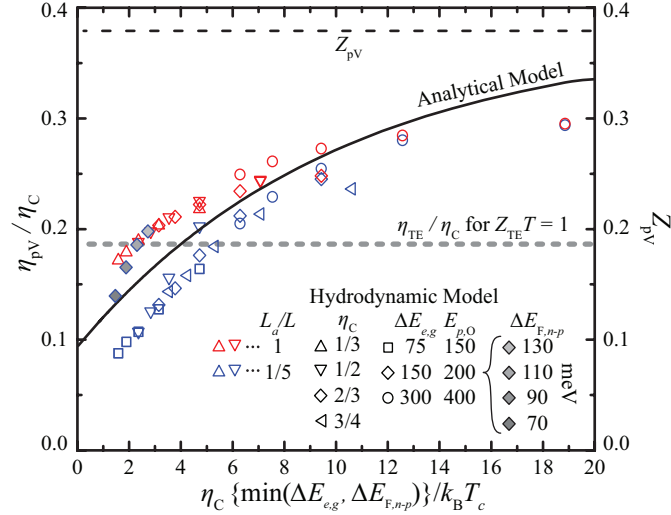


Figure 3.4: The pV efficiency as a function of $\eta_C \Delta E_{e,g}^*$ for variations in $\Delta E_{e,g}^*$ and η_C . As shown, the analytical model [Eq. (3.28)] provides a reasonable estimate for the pV cell performance. A significant nonequilibrium ($\eta_C \Delta E_{e,g}^*$) is required to exceed the TE efficiency (shown for $Z_{TE} T = 1.0$) when $Z_{pV} < 0.7$.

cell, the active length (L_a), i.e., the region where the optical phonon population is excited, is restricted to the junction itself, which is approximately 10 nm, and the diode is doped such that the difference between the Fermi energy in the p and n regions ($\Delta E_{F,p-n}$) equals the bandgap. Finally, the surface recombination (SR) is inhibited, a requirement for efficient operation (Section 3.4.2) and an assumption of the analytical model.

Note that the extent of the nonequilibrium, η_C , rather than the input heat or optical phonon temperature, is maintained at $\eta_C = 2/3$. This enables a simplified comparison between the hydrodynamic and the analytical models, which predicts $\eta_{pV} \propto \eta_C$. This represents a substantial nonequilibrium state. Moreover, this leads to large current and heat densities. For example, at $T_c = 300$ K, the optical phonon is excited to 900 K, a short circuit current density of nearly 1000 A/mm² is generated, and a heat flux of 1000 W/mm² is required. To avoid such large fluxes, a smaller phonon linewidth, a high figure of merit or small nonequilibrium are required.

Figure 3.4 summarizes the hydrodynamic results for variations in the dimensionless bandgap ($\Delta E_{e,g}^* = \Delta E_{e,g}/k_B T_c$) and the Carnot limit (η_C : primarily influences the fill-factor and open-circuit voltage), the intrinsic diode potential ($\Delta E_{F,p-n}/e_c$: primarily affects the open-circuit voltage) and the active length (L_a : primarily affects pV operation at high temperatures). While $\dot{\gamma}_{e-p}^*$, $\Delta E_{e,g}/E_{p,O}$, and Z_{pV} are constant in these pV cell, Fig. 3.7 (end of section) shows the pV efficiency for variations in these parameters and highlights the agreement between the analytical and hydrodynamic models when $\dot{\gamma}_{e-p}^* < 0.5$ and $L_a = L$. The analytical model gives a reasonable estimate across a wide range of parameters. However, there is significant discrepancy. This section explains the factors responsible for the difference and highlights the additional diode parameters required for effective pV operation.

3.4.1 Device operation

Before delving into the myriad parameters influencing the pV efficiency and its divergence from the analytical model, Fig. 3.5 illustrates the internal operation of the pV cell at 300 K under the applied voltage which maximizes η_{pV} ($\Delta\varphi_a = 5$ mV). In this cell, the optical phonon is excited within the junction, driving generation. The electrons and holes are separated by the junction and transported to and collected by the contacts. The applied voltage simultaneously drives carriers across the junction, reducing the net generation of electrons within the active region and inducing their recombination outside of it. While downconversion primarily occurs within the active region, it extends throughout the entire cell. The analytic model, in comparison, assumes the hot optical phonon population diffuses throughout the entire volume ($L_a = L$), driving substantial downconversion and generation. This leads to a decrease in the open-circuit voltage and performance loss, as shown in Figs. 3.4 and 3.6. Note that the electron, hole, and acoustic phonon transport are

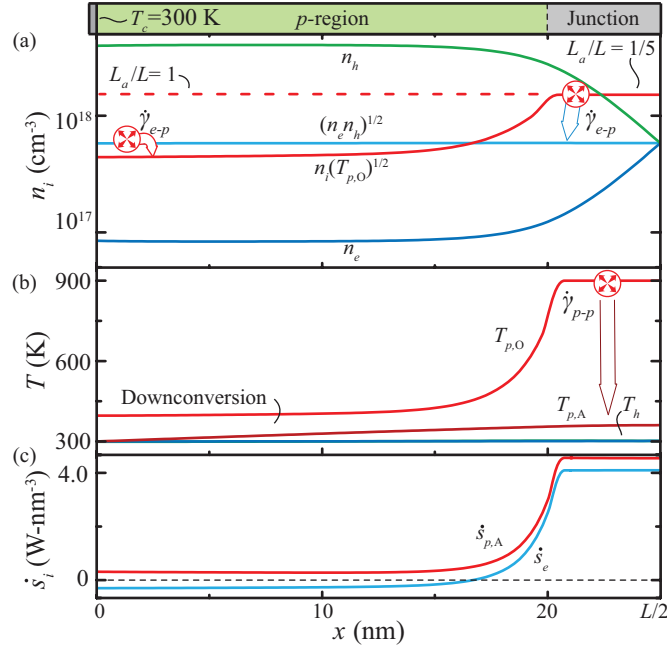


Figure 3.5: Spatial distributions of (a) the electron and hole densities, (b) population temperatures, and (c) generation and downconversion rates for a pV cell under 5 mV of applied voltage (maximum power) with $T_c = 300$ K and $T_{p,O} = 900$ K in the active region. The abrupt drop in the optical phonon temperature outside the active region leads to recombination and a lowered open-circuit voltage. Downconversion, however, extends throughout the cell.

sufficiently fast to ensure their respective population does not equilibrate with the optical phonon.

In Fig. 3.6, the (a) dimensionless and (b) dimensional current-voltage curves for this cell are shown for variations in the contact temperature. The dimensionless curves highlight the analytical limits, $\eta_{QE} = \dot{\gamma}_{e-p}^*$, and $\Delta\varphi_o = \eta_C \Delta E_{e,g}/e_c$, while the dimensional curves illustrate how a practical pV cell should behave. In particular, it depicts the efficiency loss at high temperatures, where the increased dark current reduces the fill-factor and the open-circuit voltage. While the short-circuit current vanishes with the temperature, the quantum efficiency remains constant. Indeed, low temperatures reduce both generation and downconversion rates, such that the current loss is balanced by the reduced downconversion rate. Additionally, the reduced relaxation rate in a cold cell enables the optical phonon to diffuse throughout the

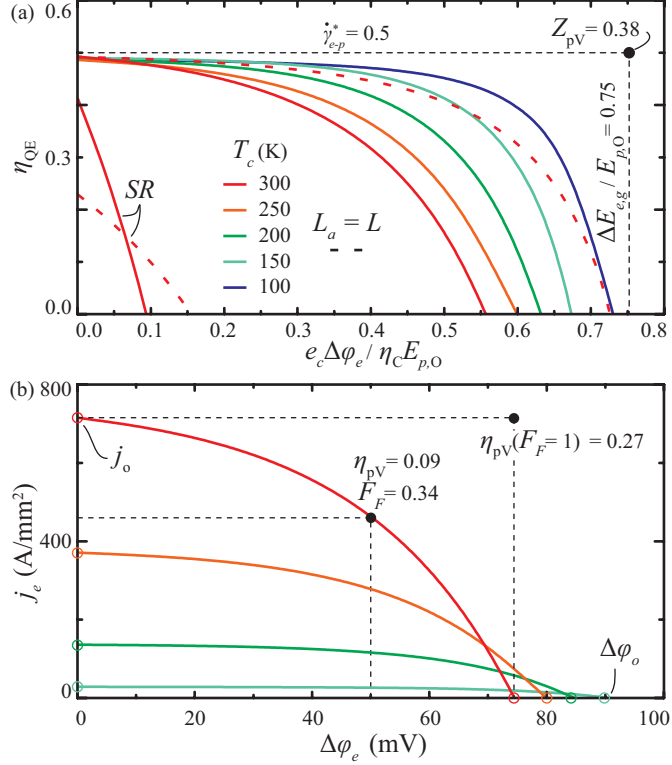


Figure 3.6: (a) Dimensionless and (b) dimensional current-voltage curves for variations in T_c for the pV cell parameters in Table 3.3. As expected, the quantum efficiency, open-circuit voltage ($\Delta\varphi_o$), and efficiency are limited by $\dot{\gamma}_{e-p}^*$, $\eta_C \Delta E_{e,g}$, and Z_{pV} . This limiting efficiency is approached as T_c vanishes and the nonequilibrium extends across the entire cell, i.e., when $F_F \rightarrow 1$ and $L_a = L$.

cell, despite its slow transport, and drive generation. Thus, the open-circuit voltage in a cold pv cell approaches that of a pV cell with $L_a = L$, i.e., that predicted by the analytical model. Furthermore, Fig. 3.6 shows that both the quantum efficiency and open-circuit voltage are significantly reduced when the surface recombination (SR) is not inhibited.

Furthermore, the dimensional curves in Fig. 3.6(b) emphasize the substantial current densities in a pV cell (and thus the heat density required to drive it). Three factors influence the current density: (i) the hot phonon temperature, $T_{p,O}$, (ii) the extent of the nonequilibrium, η_C , and (iii) the coupling strengths, a_{e-p} and a_{p-p} . Increasing these parameters increases the rate of hot optical phonon relaxation (heat

required for a given η_C) and the electron production (j_e). Thus, if lower current densities are desired, a cold cell and an optical phonon weakly coupled to the electron and phonon systems are required. Additionally, restricting L_a reduces the current generated within the pV cell.

3.4.2 Achieving analytic efficiency

Myriad factors influence cell operation. In order to achieve the predictions offered by the analytic model, a few cell design factors are crucial, the most crucial of which are highlighted here in order of importance. (i) Electron transport and pV length must ensure the electron-phonon nonequilibrium persists. (ii) Surface recombination must be inhibited. (iii) There must be sufficient doping. (iv) The optical phonon must diffuse throughout the cell. Briefly, these four factors are discussed below.

The core concept of the pV cell requires that local electron-phonon nonequilibrium exists. If electron transport is exceptionally slow or the cell is sufficiently long (e.g., order of μm), a large concentration gradient forms between the active region and the contact. The excess electrons in the active region block generation and reduce the quantum efficiency.

Surface recombination decimates the pV efficiency, and it does so in two ways. First, the minority carriers generated near the contacts tend to diffuse into those contacts and recombine. These generation events only produce entropy and lower the quantum efficiency, as shown in Fig. 3.6. Second, the small size of the pV cell implies that minority carriers driven over the junction by an applied voltage tend to reach the contact. If their entrance is not inhibited, the dark current grows much faster than predicted in the analytic model, and the open-circuit voltage vanishes as shown in Fig. 3.6. The surface recombination can be blocked, for example, by a properly doped, large bandgap material (window layer) placed between contact

and pV material blocks minority carriers from entering the contact while enabling majority carrier transport. Additional details on surface recombination and its effects are presented in Appendix C.2.

With no doping, no junction forms, minority and majority carriers are not separated, and the open-circuit voltage vanishes. Indeed, while the analytical model predicts that the open-circuit voltage is limited by the bandgap, it is truly limited by the change in the Fermi level from the p to n regions of the pV cell ($\Delta E_{F,p-n}$). Thus, to achieve the analytic prediction, the change in Fermi level must exceed $\eta_C \Delta E_{e,g}$.

Less important, but noticeable, is the ratio of the active region to the total volume. While generation occurs only in the active region, the applied voltage tends to drive minority carriers throughout the entire pV cell, where they recombine. This in turn reduces the open-circuit voltage, as shown in Fig. 3.6. Note that the analytical model assumes $L_a/L = 1$, such that $L_a/L = 0.2$ leads to a slight underperformance. At higher temperatures, this is especially noticeable, as the optical phonons relax quickly and do not escape the active region. At low temperatures, the cooling length is much larger, such that the optical phonon diffuses throughout the pV cell, regardless of the active length.

3.4.3 Exceeding analytic efficiency

Just as a myriad factors reduce pV performance below that predicted by the analytic model, there are a few important factors that enhance pV cell operation. Primarily, these factors are slow acoustic phonon transport and large $\dot{\gamma}_{e-p}^*$. When acoustic transport is slow, the acoustic phonon population in the active region heats up significantly. This reduces the net rate of downconversion. When $\dot{\gamma}_{e-p}^*$ is large, the analytic model overpredicts the heat requirements.

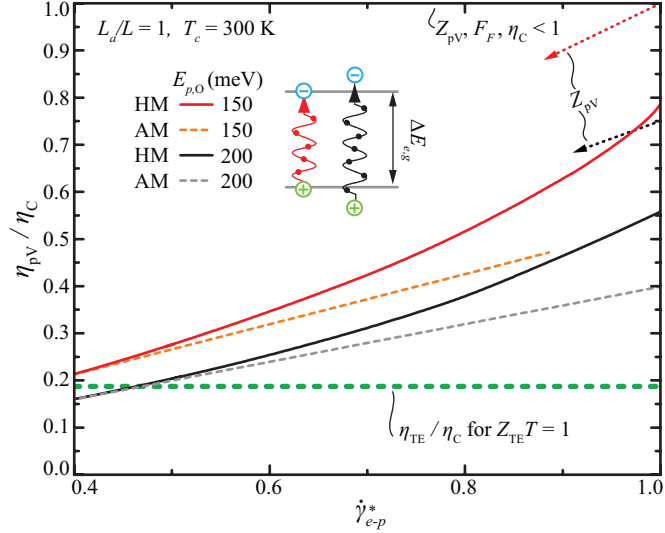


Figure 3.7: Efficiency of a pV cell for variations in $\hat{\gamma}_{e-p}^*$ using the analytical (AM) and hydrodynamic (HM) models. While increased resonance between $E_{p,O}$ and $\Delta E_{e,g}$ increases efficiency, increasing $\hat{\gamma}_{e-p}^*$ enables the efficiency to approach its limit: $\eta_C Z_{pV}$. Moreover, it greatly reduces the impact the temperature has on the efficiency and enables efficient room-temperature operation. The TE efficiency is shown for comparison.

Consider a pV cell with a large $\hat{\gamma}_{e-p}^*$. In this case, the optical phonon relaxes solely through the production of electrons. At open-circuit conditions, no heat is required to maintain the hot optical phonon population. Note that this is physically impossible: If the electron-phonon coupling is completely inhibited by the dark current, the phonon-phonon or intraband electron-phonon couplings must contribute to the relaxation of the optical phonon mode. However, the analytic model predicts that the heat requirement does not change, even as the electron-phonon coupling slows. Thus, the analytic model greatly overestimates heat requirements when $\hat{\gamma}_{e-p}^*$ approaches unity and the fill-factor is small (i.e., when the net generation rate decreases quickly as the applied voltage grows).

In Fig. 3.7, this discrepancy is illustrated for a pV cell at room temperature (300 K). Moreover, these results are for a moderate fill-factor (around 0.7). When η_C vanishes, the current-voltage curve becomes linear. In this case, achieving a large $\hat{\gamma}_{e-p}^*$ ensures a significant reduction in the heat required to operate at maximum

efficiency. Thus, the hydrodynamic simulations (HM) diverge from the analytical model (AM) for $\dot{\gamma}_{e-p}^* > 0.4$. Indeed, as $\dot{\gamma}_{e-p}^*$ approaches unity, the pV nearly reaches its limit: $\eta_{pV} = \eta_C Z_{pV}$. Figure 3.7 also shows the role of resonance in achieving high efficiency. When no kinetic energy is produced during a generation event, no optical phonon energy is wasted. Thus, a pV with a resonant bandgap surpasses the TE performance even at lower $\dot{\gamma}_{e-p}^*$.

Finally, Fig. 3.7 shows the potential of a pV cell to substantially outperform the TE, even at room temperature. Indeed, with a resonant and energetic optical phonon mode which primarily generates electrons, the pV cell triples the efficiency of a TE with $ZT_{TE} = 1$. Even under reduced nonequilibrium, such a pV cell doubles the TE efficiency. These encouraging results motivate the search for a high Z_{pV} material conducted in Chapters IV and V.

3.5 Conclusions

Here, we proposed and discussed the phonovoltaic cell which harvests energetic optical phonons resonant with the bandgap to generate power in a p - n junction. The central mechanisms, the electron-phonon and anharmonic three-phonon coupling, are discussed to quantify the quantum efficiency ($\eta_{QE} = \dot{\gamma}_{e-p}^*$). The Monte-Carlo simulations of the Boltzmann transport equation depicts the cell function using these couplings. Then, an approximate efficiency is developed analytically and a pV figure of merit proposed, i.e.,

$$\begin{aligned}
 Z_{pV} &= \dot{\gamma}_{e-p}^* \frac{\Delta E_{e,g}}{E_{p,O}} \leq 1 & \dot{\gamma}_{e-p}^* &= \frac{\dot{\gamma}_{e-p}}{\dot{\gamma}_{e-p} + \dot{\gamma}_{p-p}}, \\
 \eta_{pV} &\simeq \eta_C Z_{pV} [1 - 0.75 \exp(-\frac{\eta_C \Delta E_{e,g}}{k_B T_c})], \\
 \eta_C &= 1 - \frac{T_c}{T_{p,O}}.
 \end{aligned}
 \tag{3.29}$$

These results are most accurate when the surface recombination is suppressed, hot phonon relaxation is slow compared to the transport (or $L_a = L$), and $\dot{\gamma}_{e-p}^*$ is small or F_F is large. Regardless, Eq. (3.29) provides reasonable predictive power across a wide range of Z_{pV} and $\eta_C \Delta E_{e,g}^*$, as shown in Figs. 3.4 and 3.7. Importantly, this equation shows that either large η_C or large Z_{pV} are required for efficient pV operation.

Hydrodynamic simulations highlight the device requirements and validate the analytic model. These requirements are (i) the active volume should be maximized, such that $L_a/L \simeq 1$, unless the relaxation of hot optical phonon populations is slow compared to its transport; (ii) minority carriers must be blocked from entering the contact and recombining (i.e., hindered surface-recombination); (iii) the p - n junction must be sufficiently strong ($\Delta E_{F,p-n} > \eta_C \Delta E_{e,g}$), without inhibiting generation and lowering $\dot{\gamma}_{e-p}^*$. Additionally, the hydrodynamic model predicts that large $\dot{\gamma}_{e-p}^*$ increases the efficiency significantly compared to the linear relationship predicted by the analytic model.

When these requirements are met, and for $Z_{pV} \geq 0.7$, the pV cell is shown to significantly outperform a TE cell with $Z_{TE}T = 1$ (Figs. 3.3, 3.4, and 3.7). In Chapter V, the bandgap of graphite is tuned to resonate with its optical phonon modes by alloying it with boron nitride. This material is shown to exceed this figure of merit[53].

CHAPTER IV

The Importance of Kinetics: A Study of Partially-Hydrogenated Graphene

In this chapter the bandgap of graphene is tuned through its partial-hydrogenation. The *ab initio* bandgap is found for partially-hydrogenated graphene cells with variations in the atomic fraction and configuration of hydrogen. A stable structure is found which tunes the bandgap to roughly the E_{2g} graphene phonon mode (200 meV). Additional tuning to the E_g graphene mode is accomplished through the application of a small, isotropic strain. Then, the phonon and *e-p* properties are calculated, and compared with the *e-p* and *p-p* coupling in graphene and graphane. The transition from π to σ -type bands is shown to inhibit the *e-p* coupling and limit the $Z_{pV} < 0.1$.

4.1 Partially hydrogenated graphene

Theoretical investigations of graphane (fully-hydrogenated graphene) began before that of graphene[84]. Two stable conformations were discovered, the most stable of which is the chair conformation [Fig. 4.1(a)], wherein the hydrogen atoms alternately bind above and below carbon atoms in the graphene plane[70]. During hydrogenation, out-of-plane hydrogen atoms transform the local, sp^2 hybridized graphene structure into a sp^3 hybridized graphane structure. The resulting planar sp^3 structure localizes electrons within the σ -bond and opens a bandgap. Theoretically,

cal studies predicted a bandgap as high as 3.5-3.7 eV in graphane, depending on the conformation[85]. Although full hydrogen coverage has not been achieved experimentally, experimental and reversible hydrogenation of graphene has provided evidence for graphane[15] and its phonon properties, which are supported theoretically[62].

As the structural stability of graphane (partially-hydrogenated graphene) increases with hydrogen coverage, it is predicted that islands of hydrogenated carbon forms in a particular conformation and that these islands expand as hydrogenation continues[84, 85]. An example of such an island is shown in Fig. 4.1(d). As the hydrogenation progresses, the bandgap opens until full coverage is achieved. Thus, the bandgap of graphene is tuned by controlling the extent of the hydrogenation.

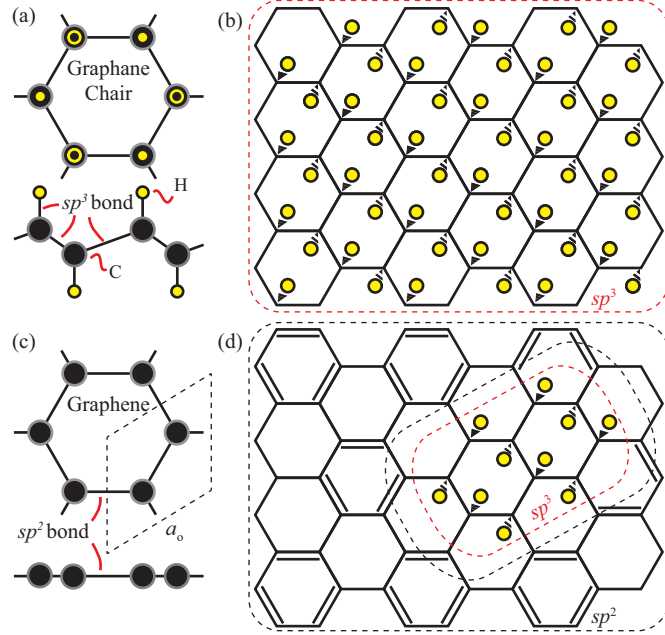


Figure 4.1: (a,b) Graphane in the chair configuration and (c) graphene and (d) partially hydrogenated graphene. Hydrogenation opens a bandgap by altering the sp^2 hybridized structure of graphene and transforming it into a sp^3 structure.

For the *ab initio* calculations to follow, the initial configuration chosen for the simulations within the density functional theory (DFT) and the density functional perturbation theory (DFPT) have a substantial impact on the resulting predictions.

Thus, constructing a grapheme supercell requires care. Indeed, the location of added hydrogen atoms, their conformation, and the number of hydrogen atoms compared to the number of carbon atoms all influence the resulting electronic and phononic properties.

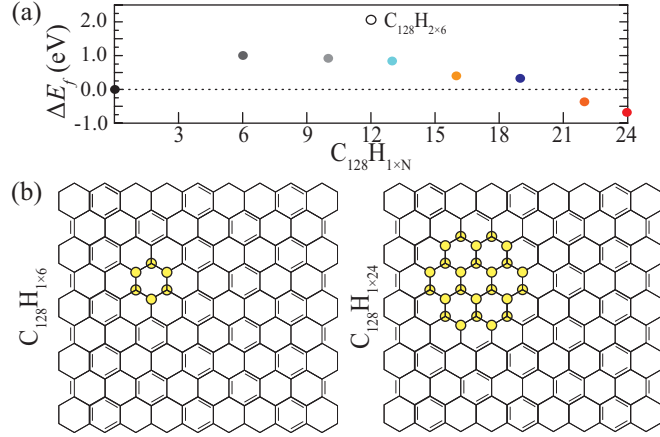


Figure 4.2: (a) Formation energy of grapheme structures for an increasing number of hydrogen in a chair configured island. Each island tested has fully hydrogenated carbon rings ($C_6H_{1 \times 6}$). Nearly complete concentric rings (22 H) or complete concentric rings (24 H) are required for stability. (b) Grapheme cells $C_{128}H_{1 \times 6}$ and $C_{128}H_{1 \times 24}$ are shown.

A rectangular graphene supercell of 128 carbon atoms (C_{128}) forms the scaffolding for the simulated grapheme cells. Hydrogen atoms are placed onto this scaffold in the chair configuration in fully-hydrogenated rings ($C_{128}H_{1 \times 6}$), as these are expected to be more stable than a partially-hydrogenated carbon ring. Structures involving multiple rings ($C_{128}H_{N_R \times 6}$) and larger hydrogenated islands are tested $C_{128}H_{1 \times N_H}$, where N_R and N_H are the number of rings and atoms. For example, two or three conjoined rings create a 10 H island ($C_{128}H_{1 \times 10}$) or 13 H island ($C_{128}H_{1 \times 13}$). $C_{128}H_{1 \times 6}$ and $C_{128}H_{1 \times 24}$ are shown in Fig. 4.2(b).

The density functional theory code VASP[37, 38, 36, 35] with plane-augmented wave[6, 39] (PAW) pseudopotentials using the generalized gradient approximation (GGA) and Perdew-Burke-Ernzerof[64, 65] functional (PBE) is used to relax the structures to their minimum energy. A \mathbf{k}_e mesh of $6 \times 6 \times 1$ and energy cut-off of

400 meV are used until forces converge to within 10^{-4} eV/Å and the total energy converges to within 10^{-5} eV, where \mathbf{k}_e is the electron wavevector. The resulting formation energies are shown in Fig. 4.2(a).

While a single hydrogen ring ($C_{128}H_{1\times6}$) is unstable, further and adjacent hydrogenation increases stability (while additional, non-adjacent rings do not). Thus, it remains likely that islands of hydrogen form and then expand outward. These results additionally suggest that the hydrogen prefers to form in even-numbered clumps such that all electrons pair. As expected, stability increases as the internal sp^3 structure grows larger than the strained sp^3 - sp^2 interface at the grapheme-graphane border.

4.2 Electron properties

The *ab initio* electronic properties of grapheme are presented in Figs. 4.3 and 4.4 for a small (a), odd (b), and large (c) number of H atoms, where the density of states are calculated on a $30 \times 30 \times 1$ \mathbf{k}_e -point mesh. When a small and even number of hydrogen are present, no bandgap opens, but the Dirac-point moves along the Γ -X line towards X. Only after the hydrogen island occupies a substantial portion of the grapheme unit cell does a bandgap open (at X), and this bandgap exceeds 200 meV, i.e., the most energetic phonon mode in graphene. When an odd number of hydrogen are present, the un-paired electron is trapped at the Fermi surface with a substantial energy gap between this trapping band and the valence and conduction bands.

These results, in addition to the substantial strains required to open a bandgap (see Appendix A), demonstrates the stability of the Dirac-point, which has been linked to translation and time invariance (i.e., its symmetry)[46]. This presents a challenge when tuning the bandgap to resonate with the optical phonons. However, once sufficient hydrogenation opens a bandgap and shifts the topology, arbitrary

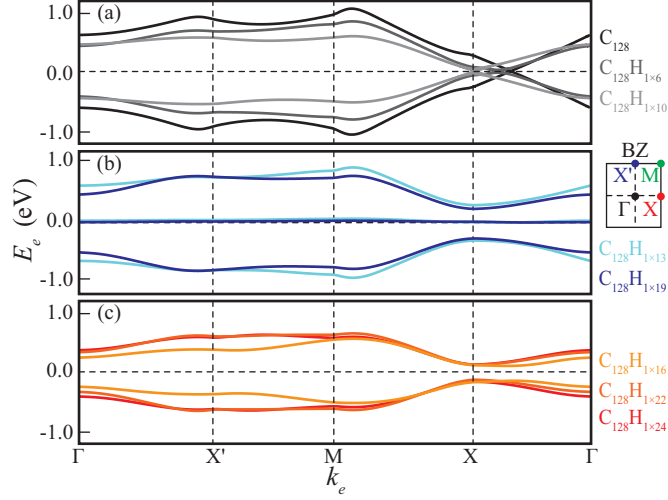


Figure 4.3: Electron Dispersion of lowest-energy bands in graphene (C_{128}) and graphane ($C_{128}H_{N_R \times N_H}$) for variation in the number of islands (N_R) and number of hydrogen atoms per island (N_H). (a) At low hydrogen concentrations, no bandgap opens but the Dirac-point moves towards X along the Γ -X high-symmetry line. (b) A trap band forms for an uneven number of hydrogen atoms. (c) At large hydrogen concentrations, however, a narrow bandgap opens at X. Some discontinuities arise from the crossing of the π and σ bands.

perturbations tune the bandgap.

Indeed, the bandgap becomes highly sensitive to the lattice constant (i.e., isotropic strains or thermal expansion) and the addition of additional hydrogen atoms. For example, the bandgap in $C_{128}H_{1 \times 24}$ changes from a 250 to a 175 meV bandgap under a isotropic strain of -0.02, while the bandgap of $C_{128}H_{1 \times 24}$ is 15 meV larger than $C_{128}H_{1 \times 22}$. Fine-tuning the bandgap of graphane through hydrogenation in *ab initio* simulation is challenging, as large structures (e.g., $C_{512}H_{2 \times 16, 2 \times 22}$) are required to achieve $\Delta E_{e,g} \simeq E_{p,O}$. Evaluating the phonon and *e-p* properties in a 600 atom cell is computationally impractical. Thus, the results presented in this chapter utilize small and isotropic strains to fine-tune the bandgap of $C_{128}H_{1 \times 24}$, such that it resonates with the desired optical phonon mode.

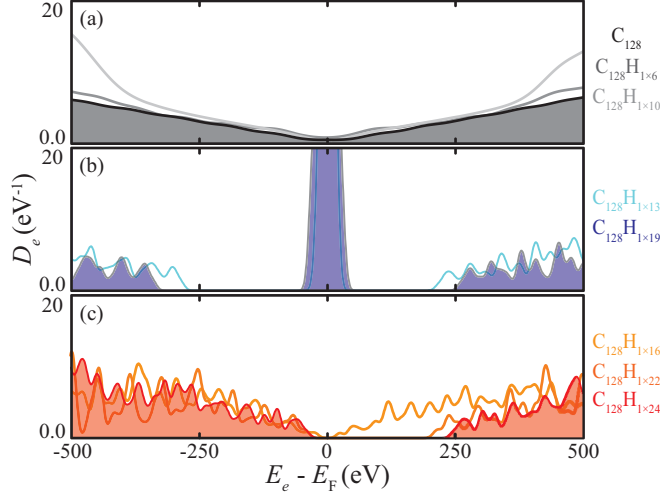


Figure 4.4: Electron density of states for graphene and graphane. The density of states is not affected significantly at (a) low hydrogen concentrations, (b) unless an unpaired electron is left in the structure ($C_{128}H_{1 \times 13}$, $C_{128}H_{1 \times 19}$). (c) A significant bandgap is not formed until the structures become stable ($C_{128}H_{1 \times 22}$), at which point a 250 meV bandgap opens.

4.3 Phonon properties

The *ab initio* dynamical matrices are evaluated within DFPT[3] on a rough mesh of \mathbf{k}_p points. On particular, graphene and graphane dynamical matrices are calculated on a $18 \times 18 \times 1$ \mathbf{k}_p mesh, while only the Γ -point dynamical matrix of $C_{128}H_{1 \times 24}$ is calculated due to computational constraints. However, this Γ -point calculation contains approximately an $8 \times 8 \times 1$ mesh of atomic force constants. These dynamical matrices are Fourier transformed into real-space and then interpolated to an arbitrary point in \mathbf{k}_p space. The resulting phonon dispersion and density of states for graphene, graphane, and $C_{128}H_{1 \times 24}$ are shown in Fig. 4.5.

The active optical phonon modes in graphene are the E_{2g} and A'_1 modes, where the A'_1 mode is at a Kohn anomaly and couples most strongly to the electronic system. The hydrogenation of graphene substantially changes the phonon properties. Graphane exhibits an extremely energetic optical phonon mode per Hydrogen atom: The out-of-plane vibration of hydrogen, as well as the less energetic E_g (rather than

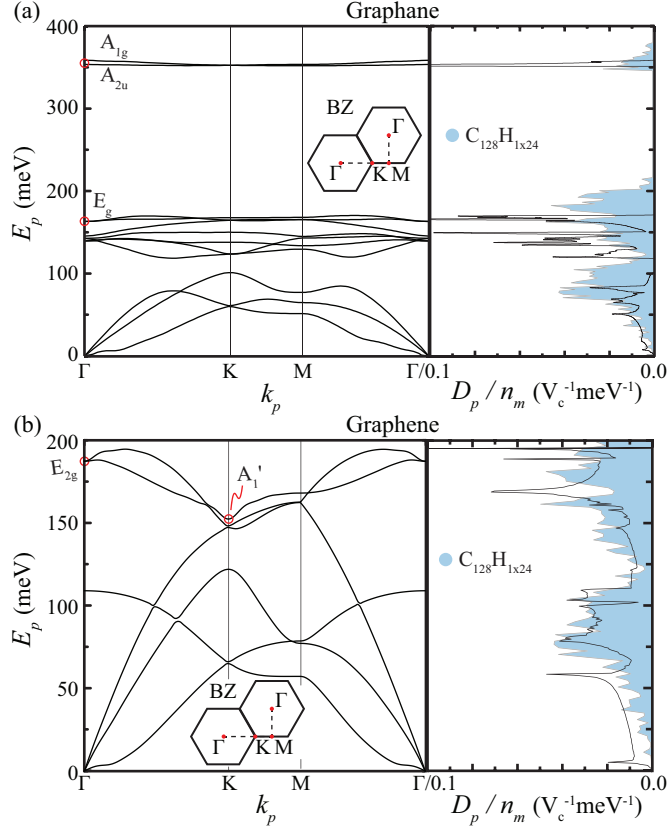


Figure 4.5: Phonon dispersion and density of states (D_p) for (a) graphane, (b) graphene, and $C_{128}H_{1 \times 24}$, where D_p is scaled by the number of modes (n_m) per unit cell. As expected, the $C_{128}H_{1 \times 24}$ phonon density of states shows a combination of the graphene and graphane optical phonon modes. These include (in order of energy) the energetic A_{1g} and A_{2u} graphane modes (out-of-plane hydrogen vibration), the E_{2g} mode (graphene), the A'_1 mode (graphene mode - Kohn Anomaly), and E_g (graphane).

E_{2g}) mode. Moreover, the optical modes in graphane tend to have lower group velocities. Graphane exhibits a mix of these modes, some smeared and distorted by the graphene-graphane border.

4.4 Scattering kinetics

As discussed in Chap. III, the relaxation of hot optical phonons through the generation of new electrons or acoustic phonons largely determines the performance of a pV cell. The e - p and anharmonic p - p couplings drive these phenomena. This section presents the *ab initio* coupling and kinetics from perturbation theory as

discussed in Sec. II for both coupling mechanisms.

4.4.1 e - p coupling and kinetics

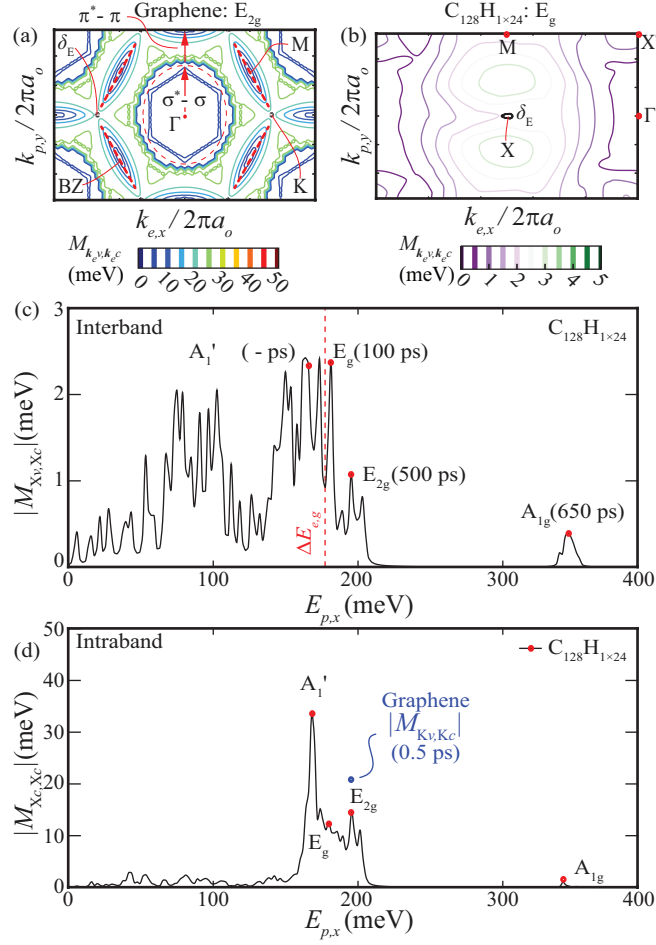


Figure 4.6: Contours of constant e - p coupling ($|M_{e-p}|$) and energy conserving lines (δ_E) of a selected phonon modes in (a) graphene and (b) $C_{128}H_{1 \times 24}$. The (c) intraband and (d) interband e - p coupling strength at the band-edge (X) for variations in $E_{p,O}$ and the phonon lifetime ($1/\gamma_{e-p}$) of selected modes.

Figure 4.6 shows the e - p coupling between the lowest conduction and highest valence bands in (a) graphene for the E_{2g} and (b) $C_{128}H_{1 \times 24}$ for the E_g optical phonon modes. After hydrogenation, the interband e - p coupling is substantially reduced near the band-edge. Indeed, Fig. 4.6(c) shows the weak interband coupling in graphane for all optical phonon modes at the bandedge (X), and that the e - p lifetime increases from 0.5 ps in graphene to over 100 ps in graphane. However, the

intraband coupling elements shown in Fig. 4.6(d) are not substantially weakened by the hydrogenation.

The poor overlap between σ and σ^* bands explains these results. Note that near the Γ -point in graphene, the σ -bands are nearest the Fermi surface, and Fig. 4.6(a) shows the weak coupling in this region. In comparison, the π - π^* band coupling near K and M is strong, as these bands overlap significantly.

Hydrogenation opens a bandgap by transforming graphene from a sp^2 to sp^3 hybridized structure. During this transition, the σ bands approach the Fermi surface and replace the π bands as the lowest energy bands. At this point, a bandgap opens. As the coupling between the σ - σ^* bands remains weak, so too does the interband coupling in graphane. In contrast, two conduction or valence states overlap completely, such that the intraband coupling remains strong. Thus, the e - p coupling of the E_{2g} mode in graphane is reduced from its value in graphene by approximately the atomic hydrogen fraction, rather than an order of magnitude.

A pV material must achieve stronger e - p coupling in order to succeed as a pV material. As functionalized graphene variants often transition from sp^2 to sp^3 hybridization, these materials, like graphane, will not achieve a high figure of merit due to the poor overlap between their σ and σ^* bands. An efficient pV material must achieve stronger e - p coupling, as the anharmonic phonon couplings, in comparison, do not change substantially. This is discussed in the following sections.

4.4.2 p - p coupling and kinetics

As discussed in Chapter II, the anharmonic (third-order and higher) interactions are responsible for phonon downconversion. However, evaluating the third-order force constants in $C_{128}H_{1 \times 24}$ remains unreasonable even under this restriction. Thus, the p - p lifetimes are evaluated from pure graphene and graphane crystals to estimate

the lifetimes of the various targeted optical phonon modes. For both of these structures, the third-order force constants are evaluated within DFPT using the $2n + 1$ formula[25], as implemented within Quantum Espresso on a $18 \times 18 \times 1$ \mathbf{k}_p point mesh. These dynamical matrix derivatives are fourier transformed into real space and then interpolated onto a $200 \times 200 \times 1$ mesh of \mathbf{k}_p points. Then, the integration in Eq. (2.8) is calculated using a Lagrangian δ -function with 20 K smearing.

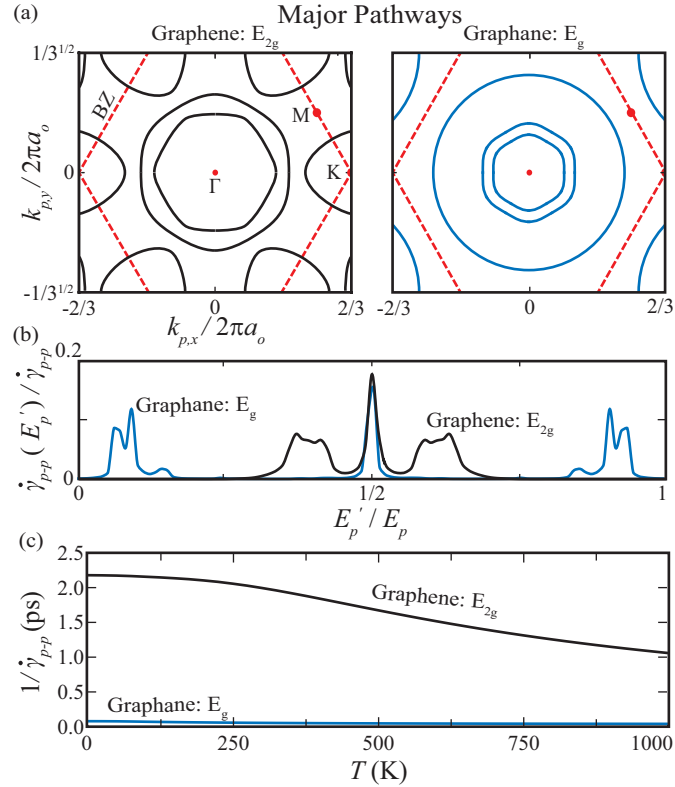


Figure 4.7: (a) Active downconversion pathways, (b) energy of the phonon modes produced, and (c) the scattering rate as a function of temperature for graphene E_{2g} and graphene E_g modes. Graphane exhibits significantly enhanced optical phonon downconversion rates.

Figure 4.7(a) shows the the downconversion paths for the graphene E_{2g} and graphene E_g phonon modes, (b) the energy of the phonon modes created, and (c) their lifetimes. Due to the high energy of these modes, the phonon lifetimes begin to change significantly around 500 K. Also shown in Fig. 4.7(c) is the increased downconversion rates of the zone-center optical phonon modes in graphane, as compared

to those in graphene. Indeed, even without the degradation of the electron-phonon coupling, hydrogenation enhances the optical phonon downconversion rates and reduces the promising $\dot{\gamma}_{e-p}^*$ of graphene.

4.4.3 Figure of merit

Using the results from Sections 2.2 and 4.4.2, $\dot{\gamma}_{e-p}^*$ is calculated for the zone-center modes in $C_{128}H_{1 \times 24}$, where $\dot{\gamma}_{e-p}^*$ is

$$(4.1) \quad \dot{\gamma}_{e-p}^*(\Gamma, \alpha) = \frac{\dot{\gamma}_{e-p}(\Gamma, \alpha)}{\dot{\gamma}_{e-p}(\Gamma, \alpha) + \dot{\gamma}_{p-p}(\Gamma, \alpha)}.$$

The results are shown in Fig. 4.8. Note that the $\dot{\gamma}_{p-p}(\Gamma, \alpha)$ used here are from the graphane and graphene calculations.

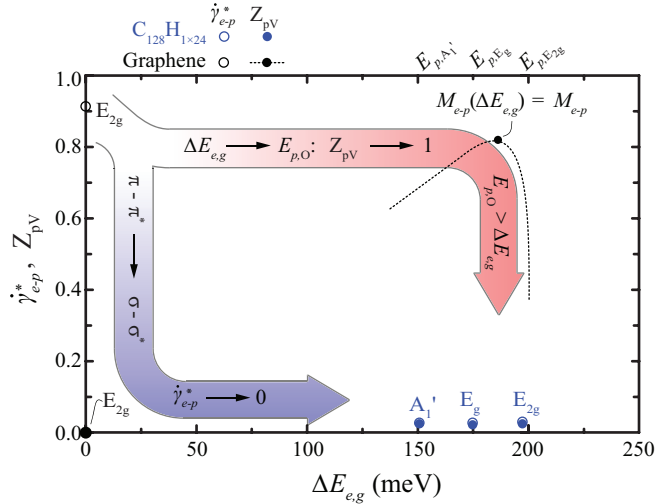


Figure 4.8: The fraction of hot optical phonons which generate electrons as they relax ($\dot{\gamma}_{e-p}^*$) and pV figure of merit (Z_{pV}) for graphene and tuned $C_{128}H_{1 \times 24}$ cells. Also shown is the graphene figure of merit if the $e-p$ and $p-p$ couplings remained constant as the bandgap opens. This figure of merit is substantially larger than that of $C_{128}H_{1 \times 24}$, as the interaction between the σ and σ^* bands is much weaker than that between the π and π^* bands in Graphene.

As shown in Fig. 4.8, the weak $e-p$ coupling in partially-hydrogenated graphene prevents it from achieving a large $\dot{\gamma}_{e-p}^*$ and Z_{pV} . This weak coupling is due to the small overlap between its valence (σ) and conduction (σ^*) bands. No similar effect reduces the $p-p$ interaction strength, such that the $\dot{\gamma}_{e-p}^*$ achieved by $C_{128}H_{1 \times 24}$ is

less than 0.1. As the bandgap is tuned to resonate with the optical phonon modes, $Z_{pV} = \dot{\gamma}_{e-p}^* < 0.1$.

In graphene, the overlap of π and π^* bands enables a large $\dot{\gamma}_{e-p}^* > 0.9$, but the gapless electronic structure ensures $Z_{pV} = 0$. If the $e-p$ and $p-p$ couplings were to remain unchanged as the bandgap opened, however, graphene would achieve a $Z_{pV} > 0.8$. In such a pV cell, the efficiency significantly exceeds that of a TE, even at room temperature and under negligible $e-p$ nonequilibrium. However, it is challenging to tune the bandgap of graphene without transitioning from π - π^* to σ - σ^* low-energy bands.

For example, hydrogenation, fluorination and other functionalization methods which create a sp^3 structure rely on this transition to open a bandgap. If a similar decrease in the interband $e-p$ coupling occurs across all sp^3 hybridized structures, as suspected, the kinetics would preclude their use in a pV. Thus, it is crucial to confirm this hypothesis.

4.5 Conclusions

In Chap. III, a pV cell is proposed that harvests a hot population of optical phonons resonant with the bandgap and much more energetic than $k_B T$. For efficient harvest, the $e-p$ coupling must dominate the $p-p$ coupling. No current material exists with this combination of properties.

Graphene, which has energetic optical phonon modes that couple strongly to the electron system, is proposed as a candidate, provided that its bandgap is tuned to the optical phonon energy. Uniaxially strained graphene is confirmed to require extreme strain in order to open a bandgap via a series of *ab initio* calculations, wherein the movement of the Dirac-point along the K-M symmetry line must be carefully

tracked. However, the bandgap in graphene may be tuned to its optical phonon modes through its partial-hydrogenation.

Here, this tuning is accomplished through the systematic *ab initio* simulation of partially-hydrogenated graphene layers with variations in the atomic fraction and placement of hydrogen. The $C_{128}H_{1\times 24}$ structure is shown to have a bandgap around 250 meV and the arbitrary and isotropic strains enable the fine-tuning to the desired optical phonon mode, e.g., the graphene E_{2g} (200 meV) and the graphane E_g (174 meV) modes.

However, the e - p coupling between the σ - σ^* bands in graphane is significantly weaker than the π - π^* band coupling in graphene. In comparison the p - p interactions in graphane are similar to or stronger than those in graphene, as shown through the *ab initio* evaluation of graphene and graphane Γ -point phonon lifetimes. Thus, the pV figure of merit for partially-hydrogenated graphene is limited to below 0.1.

The transition from π to σ -type bands near the Fermi level as a bandgap opens in graphene due to, e.g., the application of a uniaxial strain or functionalization is proposed to limit alternate graphene derivatives. However, the reduced-dimensioned graphene structures, e.g., quantum-dots and nano-ribbons, preserve the π and π^* bands and may overcome this trend. Additional study remains for other functionalized graphene structures, e.g., flourographane, and a theoretical explanation of the weak σ - σ^* e - p coupling is required, and finding alternate pV materials is crucial.

CHAPTER V

A High ZT Material: A Study of Graphene-Boron Nitride Alloys

The previous chapter showed that opening a band gap in graphene can severely and negatively impact its interband e - p coupling. In particular, the use of hydrogenation to shift from sp^2 to sp^3 hybridization and open a band gap reduced the e - p coupling so severely that the figure of merit vanished. It is hypothesized that the change in hybridization was responsible, as the e - p coupling between the σ and σ^* bands is extremely weak in pure graphene. Thus, this chapter investigates an alternative method for tuning the bandgap of graphene: the manipulation of its sublattice symmetry. This is done in general using a simple tight-binding model and in particular using the *ab initio* (DFT-LDA) simulation of graphene with boron and nitrogen atoms substituted into the lattice (h-C:BN) or placed below the graphene layer in a graphene/BN bilayer (h-C/BN).

5.1 Graphene:BN

Changing the hybridization of graphene is one method through which to tune the band gap of graphene. Another method is to remove and manipulate the time-reversal symmetry in graphene. That is, when the symmetry between the two sublattices in graphene is disturbed, a band gap opens. In h-C:BN, carbon

atoms in the crystal are replaced with a dilute concentration of boron and nitrogen atoms.[49, 80, 17] Electrons are attracted to the nitrogen atoms, or to the carbon atoms surrounding the boron atoms, due to the relative electronegativity of boron, carbon, and nitrogen. Ion-electron and electron-electron interactions propagate this perturbation throughout the lattice, such that the symmetry of the graphene lattice is removed and a band gap opens.[56] The more BN that is substituted into the lattice, the larger the band gap grows. Placing all of the boron atoms into one of the graphene sublattices and all of the nitrogen atoms into the other sublattice creates the largest band gap at a given BN concentration, as it maximizes the asymmetry created by the BN dopants.[56]

In theory, there is little reason to expect B and N atoms to order themselves at low concentration such that most B atoms are on one sublattice and most N atoms are on the other sublattice. However, a low concentration of BN opens a relatively large band gap in experiments[9], larger than those predicted by density functional theory (DFT) simulations of h-C:BN with B and N on separate sublattices.[56] This is explained by the tendency of B and N atoms to clump into local $(\text{BN})_n$ domains and also by the under-estimation of band gaps within DFT.[56]

Unfortunately, it is computationally impractical to calculate high-quality phonon and electron-phonon properties in large supercells. This limits the granularity and variety of h-C:BN crystals which can be reasonably simulated. Here, up to 6×6 graphene supercells are used with two distinct substitutional paradigms: ordered $[\text{h-C}_x(\text{BN})_{y,o}]$, wherein B and N are always on a different sublattice, and disordered $[\text{h-C}_x(\text{BN})_{y,d}]$, wherein B and N are spread between the two sublattices. Two examples of these paradigms are shown in Fig. 1.4(b).

5.2 Graphene/BN

When a graphene sheet is placed on a h-BN substrate, such that each boron atom lies below a carbon atom in one sublattice and each nitrogen atom lies below a carbon atom in the other sublattice, as shown in Fig. 1.4(c), the cross-plane Van der Waals interactions remove the symmetry between these sublattices, and a band gap opens. However, h-BN has a slightly larger lattice constant than graphene, such that the bilayer forms a Moire superlattice, as shown in Fig. 1.4(c). This discrepancy spreads the boron – carbon and nitrogen – carbon interactions evenly between the two graphene sublattices, such that no net asymmetry arises, and no band gap opens.[30, 55] While a bilayer of graphene on an h-BN substrate does exhibit a small band gap of 40 meV[30, 55], the number of atoms required to simulate the h-C/BN superlattice prohibits *ab initio* phonon calculations.

Instead, the three ideal stacking configurations of h-C/BN are simulated here. These stacking configurations are as follows: AA stacking, where the B and N atoms are directly below the C atoms in graphene; AB-N stacking, where the N atoms are below the C atoms and the B atoms are under the vacancy in the graphene lattice; and AB-B stacking, where the B atoms are below the C atoms and the N atoms are under the vacancy, as shown in Fig. 1.4(c). Although these structures are non-physical (i.e., do not capture the lattice mismatch and its effects), simulating them helps to investigate the relationship between the asymmetry, band gap, and *e-p* coupling in tuned graphene materials. Moreover, the small unit cell enables the *p-p* coupling calculations which remain out-of-reach for the large h-C:BN supercells.

5.3 Tight binding model

Before proceeding onto the *ab initio* analysis, it is useful to determine the expected results. Here, a simple tight binding model is presented in order to determine how the sublattice symmetry effects the band structure and electron-phonon coupling.

The tight binding (TB) model assumes each electron in the crystal is tightly bound to the ions in that crystal and that the remaining electron interactions are comparatively small. Thus, the Hamiltonian (H_{TB}) is

$$(5.1) \quad H_{\text{TB}} = \sum_m H_{at,m} + \Delta H,$$

where $H_{at,m}$ is the isolated atomic Hamiltonian of atom m and ΔH represents the remaining interactions of the crystal, with $H_{at,m} \gg \Delta H$. Thus, the electron wavefunctions (ψ) are built using a linear combination of Bloch functions (Φ_{mn}) based on the atomic orbitals (ϕ_{mn}) which satisfy $H_{at,m}\phi_{mn} = \epsilon_{mn}\phi_{mn}$, where ϵ_{mn} is the energy of the n^{th} orbital for atom m . That is,

$$(5.2) \quad \psi_{\mathbf{k}_e}(\mathbf{r}) = \sum_{mn} \beta_{mn} \Phi_{mn}$$

$$(5.3) \quad \Phi_{mn} = \frac{1}{N^{1/2}} \sum_l \phi_{mn}(\mathbf{r} - \mathbf{R}_{lm}) e^{i\mathbf{k}_e \cdot \mathbf{R}_{lm}},$$

where β_{mn} is the weight of each Bloch function, which combines the atomic orbitals of each atom at location \mathbf{R}_{lm} in the $l = 1, 2, \dots, N$ unit cells.

The tight-binding approach has been widely and successfully used to model the band structure of graphene.[93, 74, 71] A simple model which accurately reproduces the band structure near the Fermi surface assumes that the bonding sp^2 orbitals (s , p_x , and p_y) form the deep valence and energetic conduction bands (σ and σ^* bands), while the remaining p_z orbitals form the near-Fermi band structure (π and π^* bands). Moreover, it assumes that these two sets of orbitals do not interact.

Thus, the basis is safely constrained to a single p_z orbital per atom, i.e.,

$$(5.4) \quad \psi_{n\mathbf{k}_e}(\mathbf{r}) = |\mathbf{k}_e\rangle = \sum_m \beta_m \Phi_m = \frac{1}{N^{1/2}} \sum_l p_{z,m}(\mathbf{r} - \mathbf{R}_{lm}) e^{i\mathbf{k}_e \cdot \mathbf{R}_{lm}}.$$

Further, it assumes these atomic orbitals are orthogonal, such that $\langle p_{z,m} | p_{z,m'} \rangle = \delta_{m,m'}$ and

$$(5.5) \quad \langle \mathbf{k}_e' | H_{\text{TB}} | \mathbf{k}_e \rangle = \epsilon_{\mathbf{k}_e} \delta_{\mathbf{k}_e', \mathbf{k}_e}.$$

Finally, it assumes ΔH only contains the interactions between the orbital centered on one atom and the ionic potential of its nearest neighbor ions ($\varphi_{\text{ion},m'}$), i.e.,

$$(5.6) \quad \langle p_{z,m'} | \Delta H | p_{z,m} \rangle = \int d\mathbf{r} p_{z,m'}(r - \mathbf{R}_{m'}) \varphi_{\text{ion},m}(r) p_{z,m}(r - \mathbf{R}_m) = -\varphi_h,$$

when m and m' are nearest neighbor atoms. Otherwise, the integral is zero. φ_h , the hopping integral, describes the tendency for an electron to hop from one atomic orbital to its nearest neighbor.

It follows from Eqs. (5.4 and 5.5) that the 2×2 matrix formed by $H_{ij} = \langle \Phi_i | H_{\text{TB}} | \Phi_j \rangle$ has eigenvalues $\epsilon_{\mathbf{k}_e}^{\pm}$ and eigenvectors $\boldsymbol{\beta}_{\pm} = (\beta_1, \beta_2)$, which represent the valence ($-$) and conduction bands ($+$). That is,

$$(5.7) \quad \mathbf{H} - \epsilon_{\mathbf{k}_e} \mathbf{I} = 0,$$

where \mathbf{I} is the identity matrix. The diagonal elements of \mathbf{H} capture the self energy (ϵ_i) of the atomic orbitals, while the off-diagonals capture the hopping strength (φ_h) modified by a phase-factor (γ), i.e.,

$$(5.8) \quad \mathbf{H} = \begin{bmatrix} \epsilon_1 & \varphi_h \gamma(\mathbf{k}_e) \\ \varphi_h \gamma^*(\mathbf{k}_e) & \epsilon_2 \end{bmatrix}.$$

The phase-factors capture the effects of the geometry on the Bloch waves, i.e.,

$$(5.9) \quad \gamma = \sum \exp(i\mathbf{k}_e \cdot \boldsymbol{\delta}_i),$$

where $\boldsymbol{\delta}_i$ is a vector connecting nearest-neighbors, as shown in Fig. 1.4(a). That is, $\boldsymbol{\delta}_1 = a(0, 3^{1/2}/3, 0)$, $\boldsymbol{\delta}_2 = \boldsymbol{\delta}_1 - \mathbf{a}_1$, and $\boldsymbol{\delta}_3 = \boldsymbol{\delta}_1 - \mathbf{a}_1 - \mathbf{a}_2$ connect an atom on one sublattice with its nearest neighbors, where a is the lattice constant and $\mathbf{a}_1 = a(1, 0, 0)$ and $\mathbf{a}_2 = a(-0.5, 3^{1/2}/2, 0)$ are the vectors defining a hexagonal unit cell.

\mathbf{H} has eigenvalues (describing the electron bands)

$$(5.10) \quad \epsilon_{\mathbf{k}_e}^{\pm} = \frac{1}{2} \{ \epsilon_1 + \epsilon_2 \pm \varphi_h [12\varphi_h^2 + (\epsilon_1 - \epsilon_2)^2 + 8\varphi_h^2 (2 \cos \frac{\kappa_{e,x}}{2} + \cos \frac{3^{1/2}\kappa_{e,y}}{2} + \cos 3^{1/2}\kappa_{e,y})]^{1/2} \},$$

and eigenvectors (describing the electron wavefunctions)

$$(5.11) \quad \beta_1^{\pm} = 1$$

$$\beta_2^{\pm} = \frac{2\epsilon_{\mathbf{k}_e}^{\pm} - \epsilon_1}{2t(1 + 2 \exp \frac{i\kappa_{e,x}}{2} \cos \frac{3^{1/2}\kappa_{e,y}}{2})},$$

where the $+$ ($-$) denotes a value associated with the conduction (valence) band.

In graphene, and in the other Group IV hexagonal materials, both atoms in the unit cell are identical, such that $\epsilon_1 = \epsilon_2$. Under this symmetry, the conduction and valence bands are degenerate (no band gap) and the electron has zero effective mass near these Dirac points (at K and K'), as shown in Fig. 5.1. This leads to many of the remarkable material properties in graphene. In addition, the TB model predicts that both of the Bloch functions contribute equally to the conduction and valence band wavefunctions throughout the BZ ($|\beta_1^{\pm}| = |\beta_2^{\pm}|$). That is, the wavefunction is spread equally between all p_z orbitals, regardless of \mathbf{k}_e and $\epsilon_{\mathbf{k}_e}^{\pm}$.

The symmetry between the two sublattices creates these phenomena. As there is no energy cost associated with an electron moving from one set of orbitals to the other, the electrons are not localized to one set of orbitals. Thus, the wavefunction

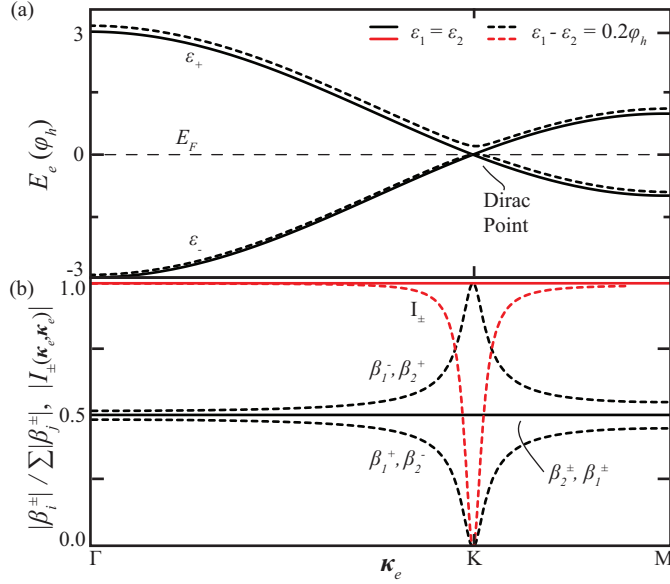


Figure 5.1: (a) The band structure (ϵ_{\pm}) and (b) fraction of the electron wavefunction composed by atomic orbitals centered on atoms in one of the two sublattices ($|\beta_i^{\pm}| / \sum |\beta_i^{\pm}|$) and resulting overlap ($I_{\mathbf{k}_e, \mathbf{k}_e'}^{\pm}$) of the valence (-) and conduction(+) bands with (—) and without (---) sublattice symmetry. In a symmetric crystal like graphene, no gap exists and the valence- and conduction-band wavefunctions overlap. In a non-symmetric crystal like h-BN, a band gap opens, the valence and conduction bands collapse into atomic orbitals centered on different sublattices, and the overlap between them vanishes at the band edge, proscribing the e - p interaction.

is a mix of both atomic orbitals. Moreover, the electrons are free to and always do move throughout the lattice.

However, when the symmetry between the two atomic sites is broken, such that $\epsilon_1 \neq \epsilon_2$, the degeneracy between the conduction and valence bands is lifted, a band gap opens ($\Delta E_{e,g} = \varphi_h |\epsilon_1 - \epsilon_2|$), and the electrons gain an effective mass at K and K' (the former Dirac points and the new band edge). Furthermore, the wavefunction at the valence (conduction) band edge collapses into the Bloch wavefunction composed of the less (more) energetic atomic orbitals, as shown in Fig. 5.1(b).

This wavefunction collapse is most intuitively understood through an excitation picture. Consider a valence electron at band edge in an asymmetric crystal, which is given just enough energy to surmount the band gap, scatter into the conduction

band, and leave a hole behind. As this electron has no energy remaining to move about the crystal (no kinetic energy), it must be localized to one of the two sets of atomic orbitals. Likewise, the hole it leaves behind has no kinetic energy and must also be localized. It is intuitive that the hole (electron) is localized to the set of orbitals with less (more) self-energy. Then, as these excitations gain kinetic energy, i.e., move through the crystal, they must also become delocalized. Therefore, their wavefunctions must mix with the previously unoccupied orbitals.

This has important consequences on the interband e - p coupling in asymmetric crystals. Consider the interband interaction element from Eq. (2.2) for a Γ -point

$$(5.12) \quad M_{ep,\alpha,+,-}(\mathbf{k}_e, \Gamma) \propto \langle \mathbf{k}_e, + | \frac{\partial \varphi_e}{\partial \mathbf{d}_{\Gamma,\alpha}} | \mathbf{k}_e, - \rangle.$$

Assuming that $\partial \varphi_e / \partial \mathbf{d}_{\mathbf{k}_p, \Gamma}$ is relatively constant throughout the cell, the interaction element is proportional to the overlap between the initial and final electron wavefunction ($I_{\mathbf{k}_e, \mathbf{k}_e'}^{\pm}$)

$$(5.13) \quad M_{ep,\alpha,+,-}(\mathbf{k}_e, \Gamma) \propto \langle \mathbf{k}_e, + | \mathbf{k}_e, - \rangle = I_{\mathbf{k}_e, \mathbf{k}_e'}^{\pm}.$$

Using Eqs. (5.4 and 5.5), the TB overlap integral is

$$(5.14) \quad I_{\mathbf{k}_e, \mathbf{k}_e'}^{\pm} = \sum_i |\bar{\beta}_i^+| |\bar{\beta}_i^-|,$$

where $\bar{\beta}_i^{\pm}$ is the normalized β_i^{\pm} . Thus, the collapse of the conduction and valence wavefunctions into orthogonal atomic orbitals prohibits the e - p interaction at, and weakens it near, the band edge (K and K'). Throughout most of the BZ, however, the TB overlap integral remains near unity, as shown in Fig. 5.1.

5.4 *Ab initio* results

The tight-binding model makes several key assumptions, e.g., that changes to the overlap integral dominate changes to the e - p interaction and that the two sets of

atomic orbitals are orthogonal. Therefore, it remains crucial to test its predictions. Here, the *ab initio* simulation of graphene, h-BN, h-C:BN, and graphene/BN is used for this purpose and in an effort to find and characterize a suitable pV material. Therefore, the TB model predicts that $\gamma_{e-p} \rightarrow 0$ as $\Delta E_{e,g} \rightarrow E_{p,O}$, but remains unaffected as $\Delta E_{e,g} \rightarrow 0$.

5.4.1 Methods

The density functional theory (DFT) and density functional perturbation theory (DFPT) calculations are done using Quantum Espresso[22], the local density approximation (LDA) for the exchange-correlation functional, norm conserving pseudopotentials generated by the Martins-Toullier method[89], and a plane-wave basis with a 55 Ry cut-off frequency. A 30×30 \mathbf{k}_e -mesh is used for graphene, h-BN, and h-C/BN crystals, while a 9×9 \mathbf{k}_e -mesh is used for the 4×4 h-C:BN supercells (32 atoms) and a 6×6 \mathbf{k}_e -mesh is used for the larger h-C:BN supercells. Phonon properties are calculated on a 15×15 \mathbf{k}_p mesh for graphene and h-C/BN and at the Γ -point of the h-C:BN crystals.

A lattice constant of 2.43 Å is used for all structures: While h-BN has a slightly larger lattice constant than graphene, a less than 6% concentration of BN should have a negligible impact on overall lattice constant. The graphite inter-layer spacing of 3.22 Å is used for the h-C/BN simulations. All structures are surrounded by at least 12 Å of vacuum. Before further calculation, the atoms are relaxed within the crystal until all force components converge to within 10^{-6} Ry/Å and the energy converges to within 10^{-8} Ry.

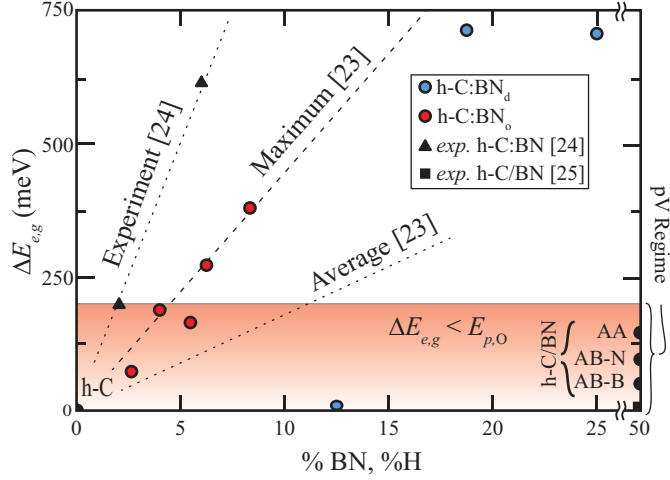


Figure 5.2: The band gap of h-C:BN and h-C/BN for variations in the BN concentration. The band gap tends to increase as the concentration increases, particularly when the B and N atoms are substituted into different sublattices (ordered h-C:BN_o), as previously predicted.[56] Conversely, the band gap widens slowly with the disordered substitution of BN onto random sublattices (h-C:BN_d). The experimental results[9] show that the gap widens even more quickly than in h-C:BN_o. Regardless, a few of the simulated crystals meet the primary pV condition: $E_{p,O} > \Delta E_{e,g}$.

5.4.2 Electron and phonon properties

Following these methods, the electron band gap and band structure are calculated for h-C, h-BN, a variety of h-C:BN crystals, and the three ideal h-C/BN stacking configurations. Then, the phonon properties are calculated h-C, h-BN, and for those h-C:BN and h-C/BN crystals which have a band gap in the range of interest [$\Delta E_{e,g} \in (0, E_{p,O})$].

Band gap

A variety of the simulated h-C:BN and all h-C/BN crystals have band gap that lies in range of interest, i.e., $\Delta E_{e,g} < E_{p,O}$, as shown in Fig. 5.2. In particular, the ordered h-C₄₈(BN)_{1,o} has a band gap extremely close to the optical phonon energy, while the disordered h-C₂₈(BN)_{2,d} has an extremely small band gap. The h-C₇₀(BN)_{1,o}, h-C₆₈(BN)_{2,o}, and the h-C/BN structures have band gaps spaced across $0.20E_{p,O} < \Delta E_{e,g} < 0.8E_{p,O}$. Thus, this collection of crystals enables a reasonable

investigation of the e - p coupling in tuned graphene.

As discussed in Sec. 5.1, the ordered placement of B and N atoms onto separate sublattices (h-C:BN_o) maximizes the band gap, while their disordered placement (h-C:BN_d) minimizes the band gap. Indeed, the band gap of h-C:BN_o approaches the maximum value predicted by Nascimento *et al.*, as shown in Fig. 5.2.[56] However, the band gap of the h-C:BN_o crystals remains well below the experimental trend.[9] Indeed, experimental results suggest that only a 2% BN concentration is required to tune the band gap of h-C:BN to its optical phonon mode (200 meV), while h-C:BN_o requires a BN concentration of 5% to reach 200 meV in these simulations. This is likely due to the underestimation of the band gap within DFT-LDA simulations.

The h-C/BN structures, in contrast, diverge from both previous *ab initio* and experimental results.[30, 55] This is expected: as discussed in Sec. 5.2, the real crystal forms a Moire superlattice, not the ideally stacked configurations simulated here. In these configurations, a boron atom (AB-B), nitrogen atom (AB-N) or both (AA) interact with one sublattice per atom, rather than interacting equally with both sublattices (as in the superlattice). Thus, a band gap opens. As the highly electronegative nitrogen interacts more strongly with the graphene layer than boron does, the AA stacking opens the largest band gap (both boron and nitrogen interact with the graphene), the AB-N stacking opens a moderate band gap (only nitrogen interacts with the graphene), and the AB-B stacking opens the smallest band gap (only boron interacts with the graphene).

Electronic Dispersion

Unsurprisingly, the electronic band structures of the three h-C/BN bilayers strongly resemble the superposition of the single layer h-C and h-BN band structures, as shown in Fig. 5.3(a) and (b). Indeed, the in-plane, electron-ion interactions are

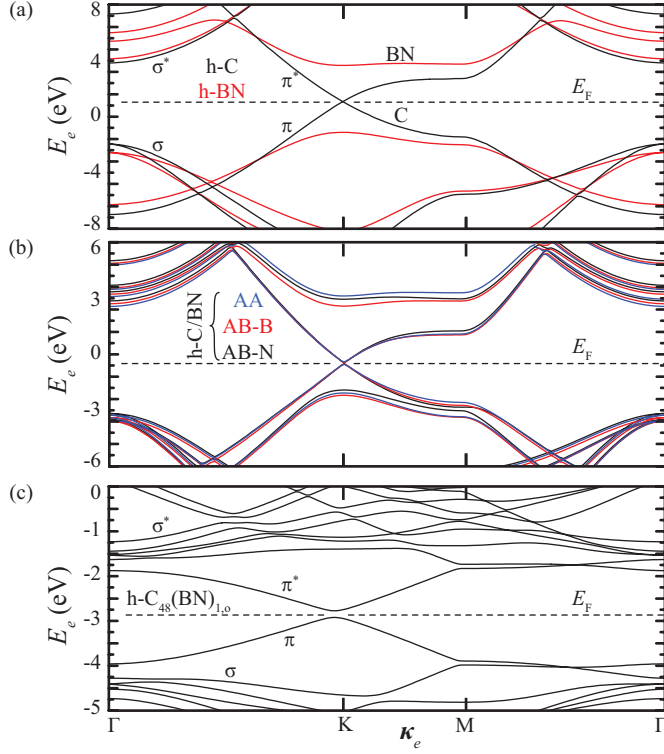


Figure 5.3: The electronic structure of (a) h-C and h-BN, (b) h-C/BN, and (c) h-C₄₈(BN)_{1,o}. The band structure of h-C/BN strongly resembles the superposition of the h-C and h-BN band structures. The band structure of h-C₄₈(BN)_{1,o}, although complicated by the band-folding, resembles that of h-C. However, the π bands are less energetic and have some dispersion throughout the BZ. Note the narrow band gap formed in h-C:BN and h-C/BN and the large band gap of h-BN.

much stronger than the cross-plane Van der Waals interactions. However, these small interactions do lift the symmetry between the graphene sublattices, such that a small band gap opens and the band edge gains dispersion at the K and K' points, as predicted by the TB model.

The electronic band structure h-C:BN primarily resembles that of graphene. Note the limited dispersion in the π bands between the K and M points and the similarities between the σ bands near Γ , as displayed in Fig. 5.3(c). However, the π bands are depressed throughout the BZ and gain slight dispersion between Γ and K, among other substantial changes. Most importantly, a small band gap opens and the band edge gains dispersion, as predicted. Indeed, the TB model accurately predicts the

qualitative features of the h-C:BN and h-C/BN π bands near the Fermi level.

Phonon density of states

The h-C/BN phonon density of states (D_p) very nearly equals the linear combination of the h-C and h-BN D_p , as shown in Fig. 5.4. While the asymmetry has important consequences for the electron band structure, the sp^2 bonds largely determine the phonon properties, and these bonds are nearly unaffected by the change in symmetry. Indeed, the only phonon features affected by the opening of the band gap are those which arise as a result of the strong e - p coupling in graphene and vanish as a result of this coupling weakening. For example, the Kohn anomaly of the TO phonon mode at K and K' (A'_1 mode) should weaken when the band gap opens, as the phonon no longer connects two points on the Fermi surface. However, accurately capturing this anomaly within DFT-LDA is difficult.[68] Therefore, the similarity between the phonon density of states in h-C, h-BN, and h-C/BN is both expected and produced.

Due to the computational requirements, calculating the dynamical matrices of h-C:BN for a grid of \mathbf{k}_p points is unrealistic. With such a small collection of force constants, Fourier interpolation only captures some features of the density of states (DOS) well. These features strongly resemble the D_p in pure graphene, as expected for such a small concentration of BN. However, some differences are certain to exist, due to the differences in mass and harmonic force constants between B, C, and N atoms. The failure to capture these features would be particularly troubling if the p - p coupling were to be calculated for h-C:BN. However, such a calculation is already precluded by the large number of atoms, as discussed in Sec. 5.4.3. Moreover, the spectral functions of h-C:BN suggest that the disturbance is minimal when the BN concentration is below 6%, as discussed in Sec. 5.4.3.

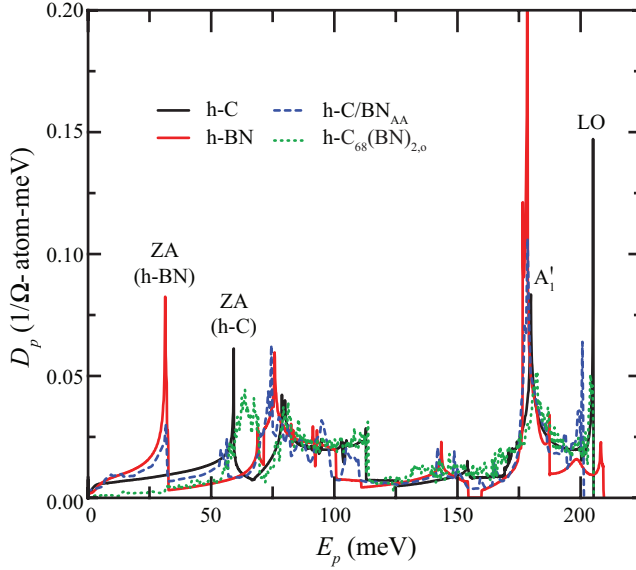


Figure 5.4: The phonon density of states (D_p) for h-C:BN and h-C/BN. The density of states in h-C/BN is nearly the superposition of that in h-C and h-BN. While the density of states in h-C:BN strongly resembles that of h-C, the h-C:BN D_p calculation uses a single *ab initio* dynamical matrix (at $\mathbf{k}_p = \Gamma$). Therefore, the D_p is not as well resolved.

5.4.3 Scattering kinetics

The interaction of the E_{2g} phonon mode, i.e., the 198 meV Γ -point LO mode, with electrons, acoustic phonons, and defects is considered in this section, using the equations discussed in Chapter II.

Electron-phonon coupling

The interband electron-phonon scattering rate given in Eq. (2.4) requires the valence and conduction band structures ($E_{\mathbf{k}_e, i}$) and the interaction matrix elements [$M_{ep, \alpha, i, j}(\mathbf{k}_e, \mathbf{k}_p)$]. The matrix elements are evaluated within DFPT on the \mathbf{k}_e -mesh given in Sec. 5.4.1, while the band structures are collected from an additional, non-self-consistent electronic calculation on a dense \mathbf{k}_e -mesh (180×180 for h-C and h-C/BN and 18×18 for h-C:BN). Then, the band structure and matrix elements are linearly interpolated onto a fine 2000×2000 \mathbf{k}_e -mesh and the integration [Eq. (2.4)] is carried out using a Lorentzian δ -function with 20 K of smearing, as in Phonovoltaic

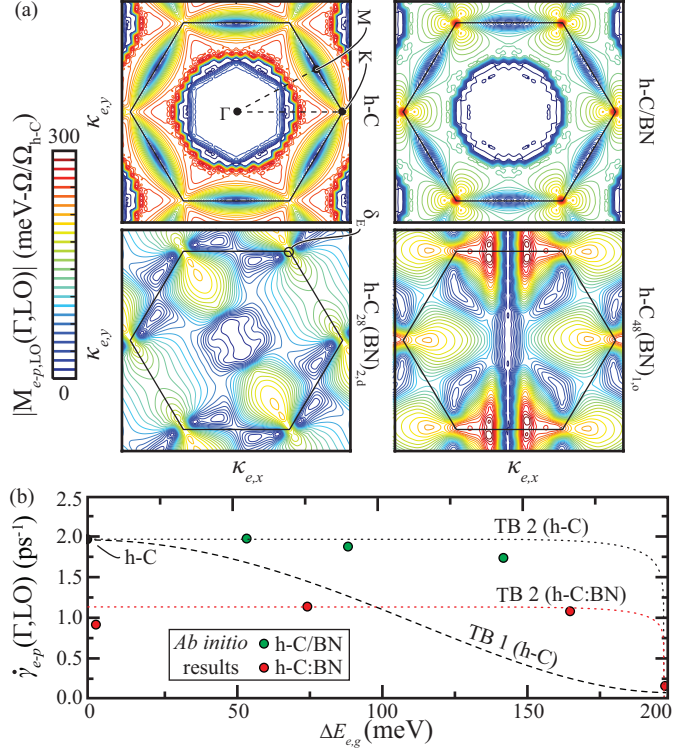


Figure 5.5: *Ab initio* (a) Interband e - p coupling and (b) e - p scattering rate in h-C, h-BN, h-C/BN, and h-C:BN for the zone-center, LO phonon mode. The BZ and high symmetry points are shown, along with the ring for which energy is conserved (δ_E). Also shown are two TB models: TB 1, which uses a scaled overlap integral [Eq. (5.14)] as the e - p matrix element; and TB 2, which assumes the matrix element is independent of the band gap. The scattering rate is approximately halved when h-C is doped with BN. However, the e - p coupling remains strong at the K and K' points, regardless of the asymmetry and band gap. Therefore, $\dot{\gamma}_{e-p}$ is nearly independent of $\Delta E_{e,g}$ until $\Delta E_{e,g} \simeq E_{p,O}$, at which point the number of states available for interband transitions vanishes. The TB 2 model predicts this trend.

II.[51]

The *ab initio* interband electron-phonon coupling strength of the Γ -point LO phonon is shown in Fig. 5.5(a), where it is scaled by the relative area of the supercell (Ω/Ω_{h-C} , where Ω_{h-C} is the area of the graphene unit cell). The e - p coupling in graphene has a few notable features. First, the coupling vanishes near the Γ -point (between the σ and σ^* bands). In Phonovoltaic II[51], this result is used to suggest that the transformation from sp^2 to sp^3 hybridization destroys the e - p coupling in graphane (h-C:H). Second, the e - p coupling is relatively strong at the Dirac points.

As the collection of energy conserving transitions form a small ring around these points (K and K'), this enables fast $\dot{\gamma}_{e-p}$. Both h-C:BN and h-C/BN exhibit these two features, as shown in Fig. 5.5(a).

This is unexpected: the TB model predicts that the conduction and valence band-edge wavefunctions are comprised of a different and orthogonal set of atomic orbitals, such that the $e-p$ coupling should vanish at the K points, as discussed in Sec. 5.3. This is particularly unexpected in h-C/BN, where the h-BN substrate primarily effects the sublattice symmetry of the h-C layer, without substantially affecting the local properties. A partial explanation of this discrepancy comes from the assumption of orthogonality in the TB model: That is, the overlap integral is at least equal to the overlap of the nearest neighbor orbitals ($I_{\mathbf{k}_e, \mathbf{k}_e}^\pm \geq \langle p_{z,1} | p_{z,2} \rangle$). Therefore, if the orbitals centered on one atom overlap substantially with those centered on the nearest neighbor, the overlap integral remains substantial, even as $\Delta E_{e,g} \rightarrow E_{p,O}$.

Two tight-binding models of the interband $e-p$ scattering rate are derived in order to examine this behavior and determine the $\dot{\gamma}_{e-p}(\Delta E_{e,g})$ trend. Both models use the TB band structure [Eq. (5.10)] and the FGR integration presented in Eq. (2.4). However, they use different matrix elements. The first model (TB 1) uses the TB overlap integral [Eq. (5.14)] as the matrix element, while the second model (TB 2) assumes the matrix element is independent of the asymmetry. The scattering rate predicted by either model only depends on $\Delta E_{e,g}/E_{p,O}$, and not on the individual parameters: $E_{p,O}$, φ_h , ϵ_1 , and ϵ_2 . Therefore, these models are fit to the *ab initio* results by setting $E_{p,O} = 198$ meV and then scaling $\dot{\gamma}_{e-p}$ to minimize the error between the predictions and the h-C, h-C:BN, or h-C/BN results.

As shown in Fig. 5.5(b), the TB 1 model predicts a steady decrease in $\dot{\gamma}_{e-p}$ with increasing $\Delta E_{e,g}$, while the TB 2 model predicts that $\dot{\gamma}_{e-p}$ is relatively independent

of $\Delta E_{e,g}$ until $\Delta E_{e,g} \rightarrow E_{p,O}$, at which point it vanishes. Indeed, the increasing dispersion at the valence and conduction band edges compensates almost exactly for the increasing band gap, such that the number of energy conserving transitions remains nearly constant as the band gap increases. When $\Delta E_{e,g} \rightarrow E_{p,O}$, however, the number of energy conserving transitions vanishes quickly, such that $\dot{\gamma}_{e-p} \rightarrow 0$. The *ab initio* results agree extremely well with the TB 2 model. Indeed, the *e-p* coupling is nearly independent of the band gap in both h-C/BN and h-C:BN.

However, the *e-p* scattering rate in h-C:BN is half of that in graphene. Interestingly, this is not a function of the asymmetry: Note that the scattering rate in h-C/BN nearly equals that in graphene, regardless of the band gap (and thus the magnitude of the asymmetry). Moreover, note that the weakest *e-p* coupling occurs in h-C₂₈(BN)_{2,d}, which has the smallest band gap and least asymmetry. As this crystal has the highest BN concentration, it is likely that the effects of the BN pairs on the local electron behavior weaken the *e-p* coupling. For example, the local electron density of states departs notably from the TB picture, especially around the BN atoms.[56]. While the asymmetry – symmetry axis provides a useful tool with which to predict the band gap, dispersion, and trend in $\dot{\gamma}_{e-p}(\Delta E_{e,g})$, it is incapable of predicting the *e-p* coupling itself, particularly in a complex tuned-graphene crystal like h-C:BN.

Phonon-phonon coupling

The *ab initio* calculation of the *p-p* coupling remains impossible for h-C:BN, due to the computational demand involved in gathering the third-order energy derivatives. Thus, it is calculated only for h-C/BN and h-C. This enables an investigation of the effects the sublattice asymmetry has on the *p-p* interaction.

The third-order force constants are evaluated on a $9 \times 9 \mathbf{k}_p$ mesh within Quantum

Espresso using the $2n + 1$ formula.[25] These are then Fourier interpolated onto a $200 \times 200 \times 1$ mesh of \mathbf{k}_p points. Then, the integration in Eq. (2.8) is carried out using a Lagrangian δ -function with 50 K smearing, as in Phonovoltaic II.[51]

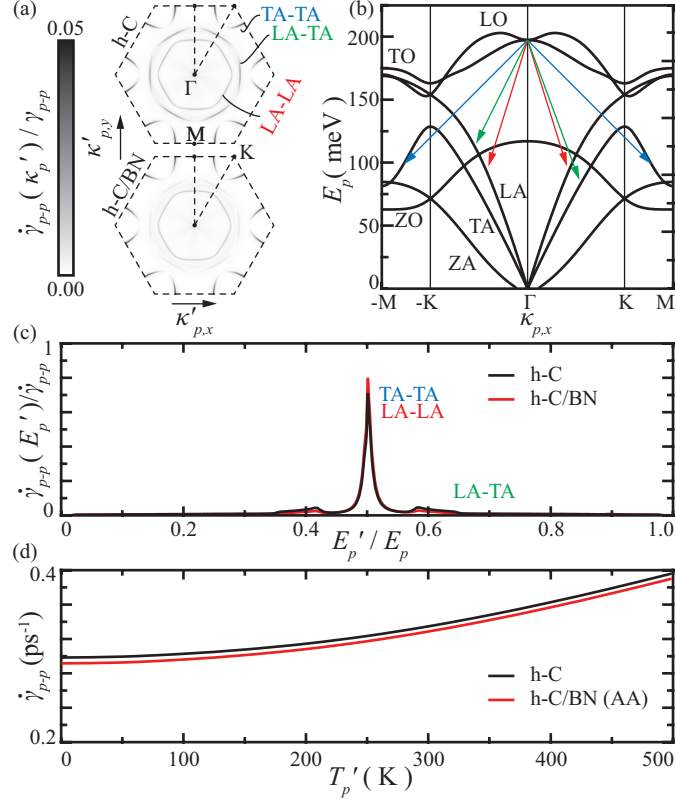


Figure 5.6: (a) The p - p coupling in the first BZ, (b) down-conversion pathways, (c) down-converted phonon energy distribution, and (d) down-conversion rates in h-C and h-C/BN. (a), (b), and (c) combine to show the momentum and energy of the acoustic phonon modes produced during down-conversion of the LO phonon. These results show that the p - p coupling is nearly unaffected by the disruption of the sublattice symmetry, such that the down-conversion rate of h-C/BN approximately equals that in graphene.

The results for h-C and h-C/BN are presented in Fig. 5.6. The h-C results agree well with DFT-LDA calculations performed by Bonini *et al.*[7] Although the LA-TA mode is found to contribute less to the rate of down-conversion, the overall rate is nearly identical. Indeed, the electron-phonon and phonon-phonon scattering rates evaluated here for graphene combine to reproduce the experimental E_{2g} phonon lifetime[95], as in [[7]].

Moreover, the p - p coupling in h-C is nearly unaffected by the disruption of the sublattice symmetry caused by the adjacent h-BN layer. The primary difference is the slight suppression of the LA-TA pathway. For the same reasons that the phonon density of states remains essentially unchanged in the graphene layer, the phonon-phonon scattering rate also remains unchanged. That is, the sp^2 bonds primarily dictate the phonon behavior, and the electrons involved in these bonds are nearly unaffected by the h-BN substrate.

However, similar arguments are less convincing when applied to the h-C:BN crystals for which a p - p calculations remain impossible. While the phonon density of states in these crystals strongly resembles that in pure h-C, there are un-resolved and rough areas of the D_p which may hide the contributions of the BN pairs. Moreover, the literature lacks a close examination of the phonon lifetimes in h-C:BN. The closest study uses MD to calculate the phonon-phonon lifetime in h-C|BN heterostructures with 50% BN.[12] The lifetime of most optical phonon modes remains unaffected by the heterostructures. However, there is a dip in the lifetime of some optical phonon modes around 200 meV when the distance between h-C and h-BN interfaces grows. That is, these results show that even at 50% BN concentration, the phonon-phonon coupling is not necessarily enhanced by the addition of BN, but by the period of the h-C|BN heterostructure. While definitive results remain elusive, the phonon-phonon scattering rate in pure graphene is used to characterize the phonovoltaic performance of an h-C:BN pV cell.

Phonon-defect coupling

As the phonon spectral function only requires evaluation of the harmonic force constants, it remains feasible to calculate the phonon-defect scattering in h-C:BN. First, the DFT-LDA dynamical matrices are collected for pure graphene and for h-

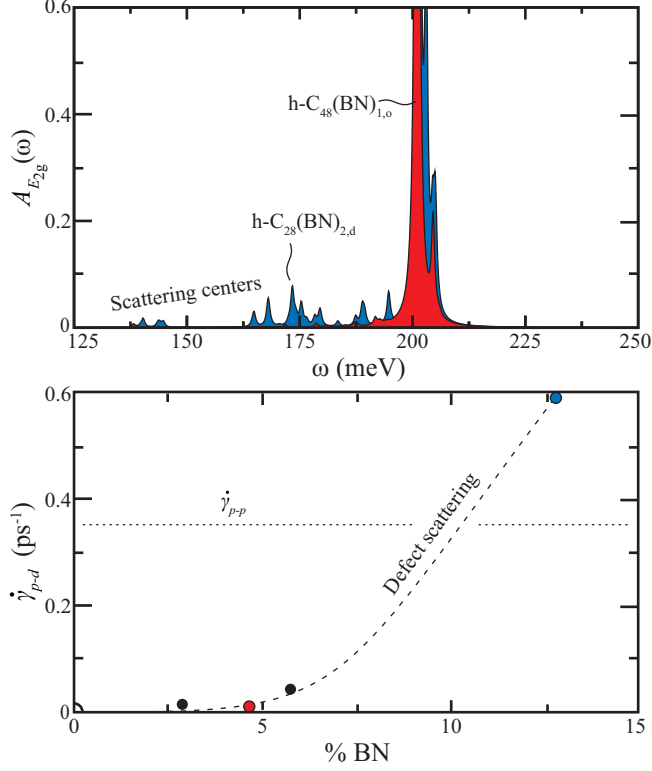


Figure 5.7: (a) Spectral function and (b) defect scattering rate for h-C:BN. While the rate of scattering is negligible at a low BN concentration, it increases substantially with the BN concentration. However, only a small BN concentration is required to tune the band gap to the optical phonon energy.[9]

C:BN. Then, the ideal graphene dynamical matrix is diagonalized in order to gather the phonon eigenvectors, and a Lanczos method is used to evaluate $G_{\mathbf{k}_p,\alpha}(\omega)$ [Eq. (2.12)].[91] Next, the spectral function is evaluated according to Eq. (2.11). Finally, a Lorentzian function is fit to $A_{\mathbf{k}_p,\alpha}(\omega)$, and the scattering rate is given by the full-width at half-maximum of that Lorentzian.[90]

The results, presented in Fig. 5.7(a), show that only a few peaks exist in the spectral function near the optical phonon energy. Therefore, the optical phonon does not have many defect modes with which to scatter. Indeed, the predicted scattering rate is negligible at sufficiently low concentration. In contrast, the isotopic scattering rate predicted by Eq. (2.10) is comparable to the rate of down-conversion and would severely impact the phonovoltaic performance, even at a 5% BN concen-

tration. However, as the decrease (increase) in mass for a boron (nitrogen) atom is compensated by weaker (stronger) force constants, the defect scattering rate of the E_{2g} mode remains negligible below 6% BN, which is sufficient to tune the band gap to the optical phonon energy. Indeed, experimental results suggest only 2% BN is required to open a 200 meV band gap.[9] Therefore, phonon-defect scattering is not important in a h-C:BN phonovoltaic.

Additionally, these results support the use of the h-C phonon-phonon down-conversion rates when evaluating a h-C:BN phonovoltaic. That is, if the spectral function has multiple, substantial peaks, it indicates that the perturbed lattice substantially affects the phonon dispersion and density of states. This, in turn, indicates that the anharmonic terms and resulting $\dot{\gamma}_{p-p}$ could be effected by the BN dopants. However, at low BN concentration, the spectral function exhibits very few off-center peaks. Therefore, it remains likely that the $\dot{\gamma}_{p-p}$ in h-C:BN nearly equals that in h-C.

5.5 Graphene:BN phonovoltaics

With the *ab initio* band gap ($0 < \Delta E_{e,g} < E_{p,O}$), phonon energy (nearly constant at 198 meV), and scattering rates (assuming $\dot{\gamma}_{p-p}$ remains constant, as discussed in Sec. 5.4.3), the pV figure of merit and efficiency are evaluated according to Eqs. (3.29). Here, the diode equations described in Chapter III are used to calculate the fill-factor, decreasing heat flux, and resulting efficiency. Figure 5.8 presents these *ab initio* results and the predicted phonovoltaic performance. In addition, the TB 2 *e-p* coupling model discussed in Sec. 5.4.3 is used to predict the performance of h-C:BN for $0 \leq \Delta E_{e,g} \leq E_{p,O}$.

As shown, a h-C₆₈(BN)_{2,o} pV cell can achieve a figure of merit around 0.6 and an

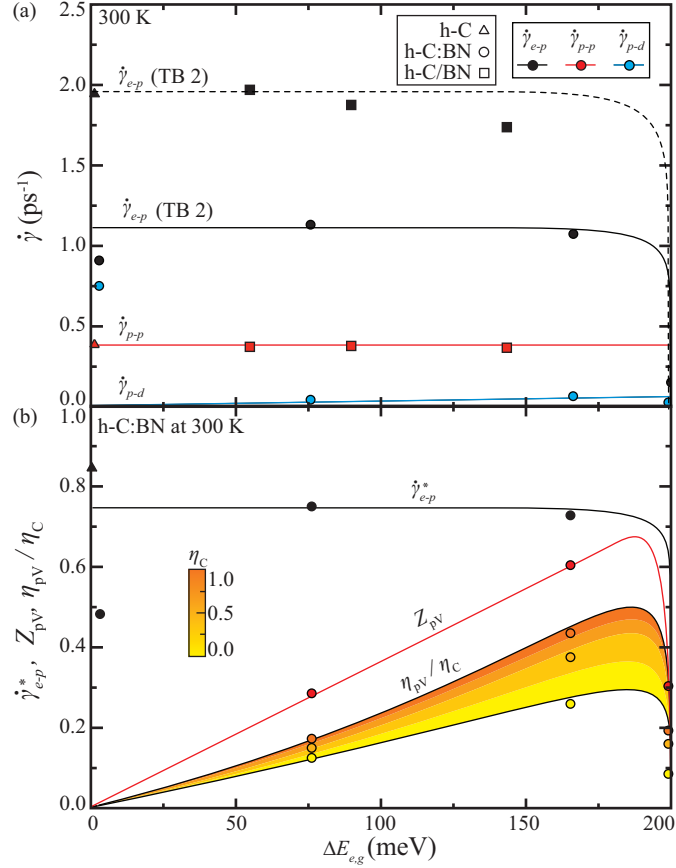


Figure 5.8: (a) The optical phonon scattering rates of h-C, h-BN, h-C/BN, and h-C:BN and (b) resulting h-C:BN performance metrics. The TB 2 model (Sec. 5.4.3) is used to model the $\dot{\gamma}_{e-p}$ trends and interpolate performance between the *ab initio* h-C:BN results. While the incorporation of BN in h-C disrupts its strong *e-p* coupling, $\dot{\gamma}_{e-p}$ remains much faster than $\dot{\gamma}_{p-p}$ until $\Delta E_{e,g} \rightarrow E_{p,O}$. Moreover, the defect scattering rate remains negligible in comparison to both $\dot{\gamma}_{e-p}$ and $\dot{\gamma}_{p-p}$. Thus, the $\dot{\gamma}_{e-p}^*$ in h-C:BN remains near 0.75 and Z_{pV} nearly reaches 0.7 at $\Delta E_{e,g} = 181$ meV. As the non-equilibrium between optical phonon population and cell increase ($\eta_C \rightarrow 1$), the fill factor of the cell increases, and the efficiency (η_{pV}) approaches the figure of merit (Z_{pV}) times the Carnot limit (η_C) [Eq. (3.28)], as shown using the color gradation.

efficiency around $0.4\eta_C$. This is a substantial improvement on the results presented in Chapter IV, which found that h-C:H pV cells had a negligible figure of merit and efficiency.[51] More importantly, it is a substantial improvement on a typical thermoelectric generator: if the thermoelectric figure of merit is $ZT = 1$ and $\eta_C = 0.5$, then its efficiency is only $\eta_{TE} \approx 0.2\eta_C$, half of the pV efficiency. Moreover, the TB 2 *e-p* coupling model predicts that a properly tuned h-C:BN pV cell achieves $Z_{pV} \approx 0.7$, as shown in Fig. 5.8. Note that h-C/BN does not make a good pV

material, as the ideally stacked bilayers simulated here do not represent the Moire superlattice that h-C/BN forms (See Sec. 5.2).

Finally, note that asymmetry neither decreases the e - p coupling strength (as discussed in Sec. 5.4.3) nor increases the p - p coupling strength (as discussed in Sec. 5.4.3). However, the substitution of BN into graphene does decrease the e - p coupling strength. Therefore, other tuned graphene materials may exceed the h-C:BN figure of merit, particularly when asymmetry is the primary mechanism by which the band gap is tuned. For example, when a strong electric field is applied to bilayer graphene, it lifts the sublattice symmetry without significantly disturbing the lattice. Therefore, it may reach an even higher Z_{pV} than h-C:BN does.

5.6 Conclusions

The promise of the pV cell is summarized and the difficulties in finding and designing a promising material are discussed. Tuned graphene remains the most promising material candidate, as graphene has an energetic optical phonon mode (200 meV) that exhibits strong e - p coupling and weak p - p coupling. Phonovoltaic II[51] showed that hydrogenating graphene (to produce graphane) can be used to tune the band gap of graphene to the optical phonon energy, but it also showed that doing so substantially weakens the e - p coupling.

Here, the e - p coupling of tuned graphene is investigated within the context of a tight-binding (TB) model in order to explore this result and discover if tuned graphene can succeed in a pV cell. The TB models shows that disrupting the sublattice symmetry in graphene in order to open a band gap also weakens the e - p coupling near the (former) Dirac points.

An *ab initio* investigation of substitutional and layered h-C:BN compounds is

carried out in order to investigate this prediction, open and tune the band gap of graphene, and, most importantly, find and describe a material with a high Z_{pV} . All of these goals are accomplished. That is, the band gaps of a various h-C:BN compounds are evaluated within DFT-LDA and a variety of h-C:BN cells are found with a band gap smaller than $E_{p,O}$. The *ab initio* e - p coupling calculations show that the TB overlap model (TB 1) is very conservative as $\Delta E_{e,g} \rightarrow E_{p,O}$: The e - p coupling remained substantial near the band edge in the h-C:BN simulations. Moreover, the phonon density of states in h-C is only slightly affected by the incorporation of BN and the p - p coupling remains unchanged, at least in the layered h-C/BN structures. Thus, h-C:BN can reach a high Z_{pV} when the band gap is appropriately tuned.

Indeed, h-C₆₈(BN)_{2,o} achieves a phonovoltaic figure of merit greater than 0.6. From previous analytical models, this implies that a h-C₆₈(BN)_{2,o} pV cell achieves at least 20% of the Carnot limit. Moreover, at a Carnot limit of 50% and cell temperature of 300 K (600 K optical phonon temperature), a h-C₆₈(BN)_{2,o} pV cell can reach an efficiency around 20%, nearly doubling the efficiency of a thermoelectric generator ($ZT = 1$) under the same conditions. Furthermore, an updated TB e - p coupling model (TB 2) predicts that an appropriately tuned h-C:BN crystal can reach $Z_{pV} \approx 0.7$.

Thus, the promise of tuned graphene is realized through the substitution of BN into graphene. Moreover, the TB model and *ab initio* results suggest that h-C:BN is not unique in this regard. Provided the sublattice symmetry of a tuned graphene material is manipulated to open a gap between 150 and 200 meV, that material should achieve similar or even higher Z_{pV} and η_{pV} .

With a suitable material candidate identified, the next theoretical challenges in pV research include the following: the identification and modeling of an appropriate

phonovoltaic system, including the optical phonon source (e.g., a pV cell harvesting phonons produced from the Joule heating in an adjacent graphene cell), and the identification of alternate materials (e.g., a graphene bilayer under an electric field). The experimental challenges include the following: the production of a high-quality h-C:BN crystal with a tuned band gap, the verification of the predicted e - p and p - p coupling strengths, and, most importantly, the demonstration of the pV effect.

CHAPTER VI

An Integrated Graphene Field-Effect Transistor and Phonovoltaic

Chapter V demonstrates that viable pV materials exist. However, it remains important to demonstrate that attractive pV applications exist. This chapter addresses this topic by suggesting the integration of a pV cell into a graphene based field-effect transistor (FET), creating a FET-pV. To facilitate and support the proposed FET-pV, *ab initio* simulations are conducted in order to investigate the electron-phonon coupling in bilayer graphene under a strong electric field. Then, MC simulations are used to examine the coupled electron and phonon populations under an electric field (i.e., in a FET) and investigate the ability of such a field to generate a suitable hot optical phonon population.

6.1 Combined graphene field-effect transistor and phonovoltaic for in-situ phonon harvest

One of the major goals in graphene research has been to develop an effective field-effect transistor[76], particularly after physicists created the first graphene FET in 2004[59]. In addition to its large mobility and its ability to maintain ballistic electron transport for hundreds of nanometers, graphene is attractive for its size[76]: While silicon-based FETs require a substantial thickness for thermodynamic stability

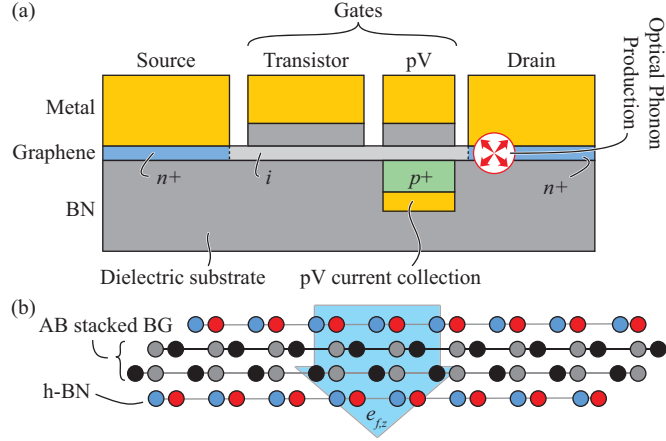


Figure 6.1: (A) An integrated graphene FET and pV and (b) bilayer graphene (BG) sandwiched between h-BN and under an electric field. A transistor field is constant applied between the source and drain. When the gate field is applied, it opens a large band gap and prohibits electronic transport in the FET. The pV diode harvests optical phonons released as ballistic electrons deposit their energy in the drain, reducing the amount of heat generated by the transistor.

and to enable the creation of a surface-charge, a graphene FET only requires a few atomically thin layers of graphene.

However, several substantial obstacles remain which prevent its success. Primarily, researchers have been unable to open a band gap exceeding a few hundred meV or to maintain the desirable properties of graphene upon opening a band gap[97, 94]. Despite these obstacles, successfully creating an effective graphene FET remains extremely attractive, as the material offers exceptional advantages. Thus, the topic remains active. Indeed, novel strategies have been suggested to aid in the adoption of graphene based FETs, including but not limited to the use of non-Boolean logic circuits[41]. Additionally, it has been suggested that graphene FETs can succeed in radiofrequency (RF) applications, where the lack of a substantial band gap does not prohibit their use[77]. Instead of the high on-off ratio required in a logical FET, a RF FET primarily requires a good electron transport and a small device size[18], i.e., the properties of a graphene FET. Indeed, by 2009 these properties had enabled graphene FET cut-off frequencies exceeding 100 GHz[40, 67].

In addition to the aforementioned obstacles facing graphene FETs, they can also produce massive heat fluxes when operating near their limits. Thus, a graphene FET presents an attractive application for in-situ optical phonon recycling, and we propose the integration of a pV cell into a graphene FET (FET-pV) to accomplish this, as depicted in Fig. 6.1(a). Indeed, if the pV is successfully integrated into a graphene FET, it could not only limit heat production in the transistor, but it could also generate some additional power.

Unfortunately, a nanoscale FET primarily produces heat near or in its drain[69], and any heat produced in the metal cannot be harvested by the pV. However, if the accelerated electrons primarily emit optical phonons in the n^+ -type graphene drain, those phonons are potentially harvestable. A detailed understanding of the electron transport in a nanoscale graphene FET is required to predict where the optical phonons are released and if an integrated graphene FET-pV can be successful. However, such an investigation is left for future study. Instead, two other crucial questions are investigated: (i) Is the material suitable, and (ii) is an electric field capable of producing a suitable population of hot optical phonons? These facets of the FET-pV are just as crucial to its success as an understanding of the spatial transport phenomena. Moreover, they answer fundamental questions about field-effect graphene as a pV material and electric fields as a suitable energy source for a pV.

In particular, *ab initio* calculations of BG under a strong electric field are performed, its electron and electron-phonon coupling properties are calculated, and the material is shown to reach a record $Z_{pV} = 0.9$. Then, the electric field driving current through a transistor is discussed as a potential source of optical phonons. Finally, MC simulations of the coupled electron and phonon populations in a graphene FET

are conducted to show that a high field produces an appropriate hot optical phonon population. These topics will provide the basis for future publication[52].

6.2 *Ab initio* properties of bilayer graphene under a strong electric field

Applying a strong electric field perpendicular to the graphene planes in BG, as shown in Fig. 6.1(b), opens a bandgap by driving electrons into one of the two layers and lifting the time-reversal symmetry of BG. This phenomena has been predicted using TB[8] and *ab initio* calculations[20] and was recorded experimentally[97, 94]. However, experimental band gaps have been limited to around 100 to 200 meV, with the stacking order and twisting angle substantially effecting the electronic properties[75, 43].

Here, AB stacked BG is investigated, where the AB stacking configuration is shown in Fig. 6.1(b) and denotes a structure wherein two of the four atoms in a unit-cell line up, and the remaining atoms are positioned above or below the vacancy in the other graphene layer. While the twisting angle may have a role in the electron-phonon coupling and bandgap size, the aim here is to discover if BG is a suitable pV material, not provide a comprehensive investigation into the role of twisting in the electron-phonon coupling. Additionally, it is not expected to have a large effect: the twisting angle primarily influences the time-reversal symmetry, and previous results suggest that the electron-phonon coupling is insensitive to symmetry changes[53].

6.2.1 Electronic properties

Self-consistent DFT simulations of BG under a perpendicular electric field are carried out using Quantum Espresso[22], the local density approximation (LDA) for the exchange-correlation functional, norm conserving pseudopotentials generated by the Martins-Toullier method[89], and a plane-wave basis with a 55 Ry cut-off

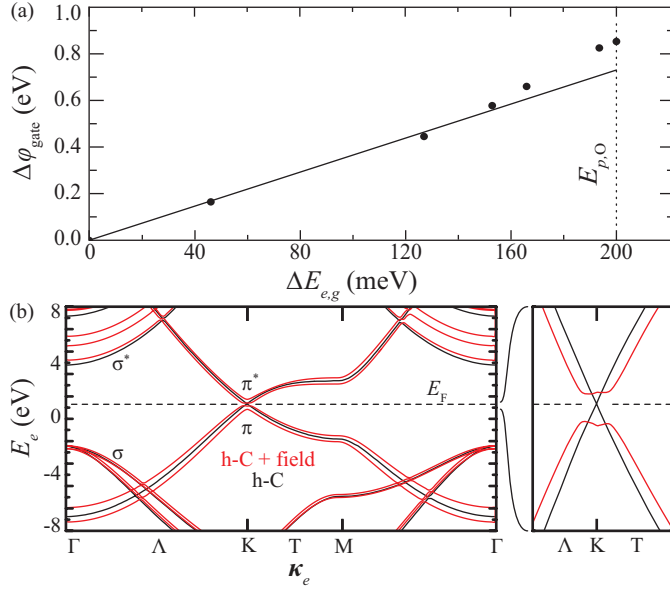


Figure 6.2: (a) The band gap in bilayer-graphene under a strong electric field and (b) the resulting electronic dispersion. The band gap is nearly proportional to the field, and a band gap exceeding 200 meV is nearly possible within the quasi-linear regime. Once the band gap grows beyond around 100 meV, the topology of constant energy contours change near the band edge, transitioning from single- to double-rings: Note the quartic electronic bands near K.

frequency. The calculations are performed on a $60 \times 60 \times 1$ \mathbf{k}_e mesh, with a saw-tooth electric potential positioned so that the field is unidirectional within the BG and switches direction within the 20 Å of vacuum between periodic images of BG. The interlayer distance c is set to 3.35 Å and the in-plane lattice constant a is relaxed to 2.43 Å.

The electronic properties calculated are consistent with the literature. For example, the band gap begins to open as a linear function of the applied field ($e_{f,z}$) or the potential between the two graphene layers ($\Delta\varphi = ce_{f,z}$)[8, 20]. This proportionality breaks down at sufficiently high fields, as shown in Fig. 6.2(a). Most importantly, these results confirm that the bandgap in BG is tunable via the application of a strong electric field perpendicular to the graphene planes.

The electronic dispersion shows similar agreement with the literature[8, 20]. That

is, as the electric field grows and the band gap opens, the valence and conduction bands at K are pushed down and up, respectively, breaking the degeneracy of the Dirac points. Moreover, the band-edges shift off of the K points and the simple linear or quadratic dispersion of graphene transitions to a complicated, quartic-like dispersion. Therefore, the constant energy curves form double rings near the K points, rather than the single rings seen in many tuned graphene materials[51, 53]. This shift in the constant energy curve topology has a large and positive impact on the interband electron-phonon scattering rate, the range of energy conserving phonon momenta, and thus, the function of a FET-pV, as discussed below.

6.2.2 Electron-phonon coupling and the phonovoltaic figure of merit in bilayer-graphene

The interband electron-phonon scattering rate given in Eq. (2.4) requires the valence and conduction band structures ($E_{\mathbf{k}_e,i}$) and the interaction matrix elements [$M_{ep,\alpha,i,j}(\mathbf{k}_e, \mathbf{k}_p)$]. The matrix elements are evaluated within DFPT on a $60 \times 60 \times 1$ \mathbf{k}_e mesh, while the band structures are collected from an additional, non-self-consistent electronic calculation on a dense $180 \times 180 \times 1$ \mathbf{k}_e -mesh. Then, the band structure and matrix elements are linearly interpolated onto a fine 2000×2000 \mathbf{k}_e -mesh and the integration [Eq. (2.4)] is carried out using a Lorentzian δ -function with 20 K of smearing, as in Phonovoltaic II and III.[51, 53]

Interestingly, the electron-phonon coupling does vanish at the K points, as predicted in the TB model of Section 5.3 and as shown in Fig. 6.3(a). This stands in contrast with the electron-phonon coupling in h-C:BN or h-C/BN which remains strong at K[53]. However, the scattering rate does not vanish as $\Delta E_{e,g} \rightarrow E_{p,O}$, as predicted by the TB model. This contradiction is explained by the change in the valence and conduction bands near K. That is, the energy conserving transitions move away from K as the band gap grows beyond approximately 100 meV, not towards

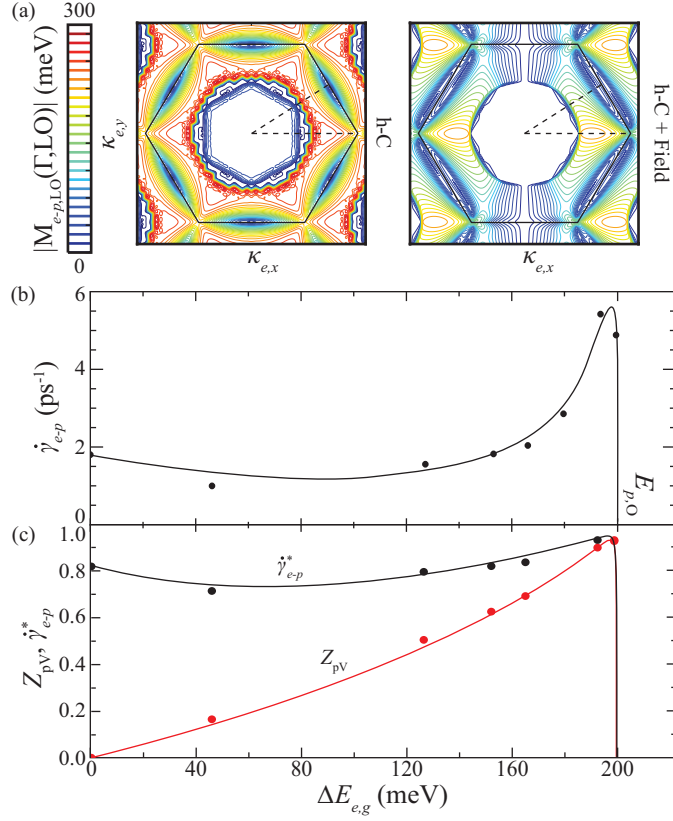


Figure 6.3: (a) the electron-phonon coupling in bilayer graphene under a field, (b) the resulting scattering rate, and (c) the $\dot{\gamma}_{e-p}^*$ and pV figure of merit for variations in the bandgap. The electron-phonon coupling vanishes at the K points, but remains strong very near them. Initially, the electron-phonon coupling decreases as the energy-conserving transitions draw closer to the K points. As the band gap increases, the change in the topology of the band-structure enables more energy conserving transitions, some of which are relatively far from K. Thus, the scattering rate increases drastically and the Z_{pV} reaches a record 0.9.

it. Thus, additional energy conserving transitions become available as the band gap grows, and the scattering rate increases. Moreover, as $\Delta E_{e,g} \rightarrow E_{p,O}$, a second ring of energy conserving transitions becomes available which is relatively far from the K points. This leads to a substantially faster generation rate as $\Delta E_{e,g} \rightarrow E_{p,O}$, as shown in Fig. 6.3(b).

This trend increases the BG pV figure of merit beyond the original goal of $Z_{pV} = 0.8$ and towards $Z_{pV} = 0.9$ at high fields and large bandgaps, as shown in Fig. 6.3(c). (Note that $Z_{pV} = 0.8$ occurs in graphene with $\Delta E_{e,g} = E_{p,O}$ and its zero-bandgap

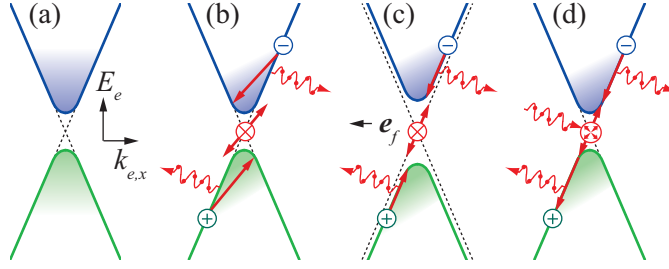


Figure 6.4: Electric fields as a source of hot optical phonons in tuned graphene. (a) An illustration of the electron dispersion and electron and hole populations in tuned graphene. Under a field, these populations are shifted symmetrically in \mathbf{k}_e space, and the excited electrons release optical phonons. (b) If the valence and conduction bands are not in-line, (c) or if the phonon released does not follow this line, then the released optical phonons have too much momentum to generate electrons. (d) If the phonon released is in-line with the bands, then that phonon can generate electrons.

$\dot{\gamma}_{e-p}^*$ of 0.8.) As the pV efficiency is limited by the product of the Carnot limit and the figure of merit, this means that a BG pV could harvest optical phonons at up to 90% of the Carnot limit. At 300 K, the pV could reach an efficiency exceeding 35% at $\eta_C = 0.5$, i.e., $T_{p,O} = 600$ K.

However, questions remain about a FET-pV. Of primary importance is the quality of an electric field as an optical phonon source. That is, (i) will the optical phonons emitted via intraband electrons be capable of generating electrons, and (ii) will the hot electrons block that generation? In the following sections, these questions are examined.

6.3 Electric fields as a source of hot optical phonons

Figure 6.4 depicts the role of an electric field in heating an optical phonon population. The electric field heats the optical phonon population by accelerating electrons which then relax via the emission of optical phonons. Note that the field creates an asymmetry in the electron distribution in \mathbf{k}_e space, as shown in Figs. 6.4(b), (c), and (d), and that this asymmetry describes an electric current.

The emitted optical phonons are not necessarily capable of generating electrons.

That is, if \mathbf{k}_p is too large, it cannot connect the valence and conduction bands, as shown in Fig. 6.4(b). Moreover, Fig. 6.4(b) shows that optical phonon emitted through an intraband process cannot connect the valence and conduction band edges if the bands do not “line-up”, i.e., the tangent-lines of the conduction (valence) band energy surface does not intersect with the valence (conduction) band energy surface. Figure 6.4(d) shows that the phonons emitted along the tangent are capable of generating electrons in a tuned graphene where the bands line-up perfectly. Note that it is not truly the tangent lines which matter, but the optical phonon emission vectors. Regardless, the tangent-line verification provides a reasonable approximation and applies precisely for the dispersionless bands of graphene.

Note that many intraband optical phonons emitted in BG are capable of generating electrons: The valence and conduction bands can be qualitatively described as having a broad trough with steep walls, such that the tangent lines from these walls intersect with the trough of the corresponding band. However, intraband optical phonon emission events can still produce optical phonons which are unable to generate electrons, i.e., through emissions of high momentum phonons, as depicted in Fig. 6.4(b). In the following section, a MC simulation is carried out to investigate which type of phonon emission is preferred and to understand whether an electric field can generate an appropriate population of optical phonons.

6.4 Monte Carlo simulation of tuned graphene under a field

The MC simulation considers a material with one dispersionless acoustic phonon polarization, one constant energy optical phonon polarization, and a dispersionless electron and hole bandstructure. Polar maps of the phonon $(k_{p,r}, \theta_p)$ and electron populations $(k_{e,r}, \theta_e)$ are used to describe their spectral heating in \mathbf{k}_p and \mathbf{k}_e space.

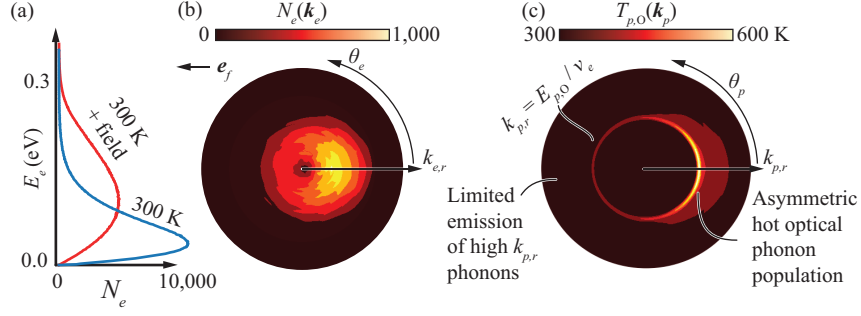


Figure 6.5: (a) The energy distribution of electrons before and after the application of a strong electric field and the final momentum distributions of (b) electron and (c) phonon populations. The electric field (oriented along $\theta = \pi$) shifts the electron distribution towards $\theta_e = 0$. These electrons, in turn, primarily emit phonons with $\theta_p = 0$. Similarly, the field creates a hole distribution near $\theta_e = \pi$, which also emits phonons near $\theta_p = 0$, as a hole losing momentum indicates an electron losing the opposite momentum.

Over 10 million electron particles are simulated to resolve these populations. Appendix B provides the remaining details of the MC simulations conducted here and a further discussion of the MC method, in general.

As expected and depicted in Figs. 6.4 and 6.5, the electric field accelerates the electrons to induce a large asymmetry in and excitation of their population. They relax by emitting optical phonons, and the results indicate that those phonons are primarily harvestable in a pV. That is, they have low momentum. Indeed, while no optical phonons are emitted with $k_{p,r} < E_{p,O}/\nu_e$, where ν_e is the constant electron group velocity, the vast majority of emitted optical phonons have $k_{p,r} \simeq E_{p,O}/\nu_e$, as shown in Fig. 6.5(b). This is crucial to the success of the FET-pV, as discussed above.

This preference to emit low-momentum optical phonons arises because every electron state with $E_e > E_{p,O}$ can emit a phonon with $k_p = E_{p,O}/\nu_e$. As the electron energy increases above $E_{p,O}$, the electron can emit increasingly larger momentum phonons, but they can still emit the $k_p = E_{p,O}/\nu_e$ phonon. Thus, the collection of \mathbf{k}_p produced by all electrons with momentum \mathbf{k}_e weighted by $\dot{\gamma}_{e-p}(\mathbf{k}_e, \mathbf{k}_p)$ gives a ring

which vanishes quickly with increasing $k_{p,r}$, i.e.,

$$(6.1) \quad \sum_{\mathbf{k}_e} \dot{\gamma}_{e-p}(\mathbf{k}_e, \mathbf{k}_p) \propto \delta(k_{p,r} + E_{p,0}/\nu_e).$$

This collection of optical phonons emitted by the excited electron and hole populations is biased by their field-induced asymmetry. That is, an electron population, shifted towards $\theta_e = 0$, primarily emits phonons with $\theta_p = 0$. While the same field shifts the hole population towards $\theta_e = \pi$, the holes also emits phonons around $\theta_p = 0$, as a hole losing some momentum is actually a representation of an electron losing the opposite momentum.

Under a sufficiently large field, the low-energy electron states are emptied by the high field, as shown in Figs. 6.5(a) and (c). Thus, generation will occur in order to refill these empty states, and question (ii) is also answered in the affirmative, and the electric field is a suitable source of hot optical phonons.

6.5 Conclusions

In this chapter a combined field-effect transistor and phonovoltaic device is discussed. Bilayer graphene is evaluated as a potential pV material, as it is central to many graphene based FET designs. *Ab initio* calculations show that bilayer graphene reaches a record pV figure of merit of $Z_{pV} = 0.9$, making it an attractive pV material. Indeed, it can reach an efficiency of 35% at 300 K when the optical phonon temperature is at 600 K.

Then, a discussion of electric fields as a source of optical phonons is presented. A new guideline is introduced for the success of a FET-pV material: In addition to requiring $E_{p,0} > \Delta E_{e,g}$, the near-Fermi FET-pV conduction (valence) bandstructure must have surface tangents which intersect with the near-Fermi valence (conduction) bands. Under this condition, optical phonons emitted via the intraband relaxation of

hot electrons can conserve momentum and energy while generating electrons. Note that tuned BG meets this criterion.

Finally, MC simulations are conducted in order to examine the typical optical phonons emitted in tuned graphene and investigate if they are suited for harvest in a pV. The simulations indicate that they are, indeed, suited. Specifically, the heated electrons primarily emit optical phonons with the minimum momentum possible momentum, $k_{p,r} = E_{p,O}/\nu_e$, in the same direction as the electric field.

Future study of the FET-pV requires an investigation of the ballistic electron transport in a graphene FET and an understanding of the location of optical phonon emission. That is, it requires an investigation to see if the majority of the electron energy is deposited in the metal contact or in the graphene drain. This requires a self-consistent MC simulation of the transport in the graphene FET, which accounts for the nonlinear potential drop near the source and drain due to rapidly changing electron concentration and geometry.

CHAPTER VII

Conclusions and Future Work

7.1 Contributions

Optical phonons are produced in great quantity in myriad devices and processes, including high-powered electronics, batteries, photonics, and photovoltaics. The resulting nonequilibrium optical phonon populations are contained in a narrow spectrum and are a low-entropy energy source when compared to heat. Thus, it should be possible to harvest nonequilibrium optical phonons more efficiently than heat.

However, due to the short length (nm) and timescales (ps) on which the nonequilibrium decays, a nanoscale structure or device is required to manipulate and use a nonequilibrium optical phonon population. Indeed, while optical phonons have been previously targeted in energy conversion processes, success has been limited. In this thesis, a new device named the phonovoltaic cell is proposed which harvests optical phonons rather than heat.

A simple and physically intuitive efficiency relationship and material figure of merit are analytically derived for this cell. Numerical modeling supports these analytical efforts. The results show that, in addition to being new and interesting, the device greatly improves upon the ability of thermoelectrics to harvest heat. Indeed, it potentially approaches the Carnot Limit

While the material requirements are strict, a graphene-based materials tuned through the manipulation of their time-reversal symmetry are shown to meet them. In particular, graphene doped with BN and bilayer-graphene under a strong electric field are shown to reach a large figure of merit through a series of *ab initio* calculations. A phonovoltaic cell comprised of these materials can exceed 40 to 60% of the Carnot limit at 300 K, respectively.

Due to the suitability of field-effect graphene, the integration of a phonovoltaic into a graphene field-effect transistor is discussed as potential phonovoltaic application. In support of this discussion, Monte-Carlo simulations of graphene under a large field is performed. The simulation shows that electric fields can provide a usable initial energy source.

7.2 Future Work

There are three extensions of the work presented within this thesis that should be pursued:

- Experimental validation: The major remaining objective is to validate the physics of the device. While the focus on theory has enabled the exploration of this device and its materials, it remains critical to validate the theory, discover additional issues, and prove to the community that the device has merit. We are currently working with collaborators at the Massachusetts Institute of Technology to build a functioning phonovoltaic cell using bilayer graphene on a hexagonal boron-nitride substrate. The nonequilibrium optical phonon population will be excited using an appropriately tuned Raman laser. While the bandgap will not be tuned to achieve a large figure of merit, cryogenic temperatures should enable the MIT researchers to record phonovoltaic effects.

- Continued modeling of the FET-pV application: While the Monte-Carlo simulations suggest that the field in a transistor is good primary energy source for a phonovoltaic, additional modeling is required to understand role of size-effects in modern transistors and the location of optical phonon emissions in a graphene FET. Furthermore, the field-effect graphene properties require additional *ab initio* modeling to understand the role of various substrates on the electron-phonon and phonon-phonon coupling rates.
- Search for other materials: While graphene is the best material option found, there is a possibility for other, better materials. In particular, organic semiconductors or semimetals may have more energetic vibrations while maintaining the coordination and symmetries required to have an ultranarrow bandgap, a strong electron-phonon coupling, and a weak phonon-phonon coupling.

7.3 Outlook

Theoretical investigations and an atomic-scale perspective have enabled the invention of a new and promising device which recycles optical phonons before they become heat; they have enabled the discovery and design of multiple potential materials; and they have enabled the proposal of a potential application. Discovering this device experimentally would have been exceedingly unlikely, due to the stringent material requirements unearthed during its theoretical study. Indeed, this thesis shows the indispensable nature of theory, which can reveal facets of a problem which are currently unavailable to experimentalists and iterate on the materials and methods investigated relatively quickly and inexpensively.

However, this thesis also shows the importance of experiment. While the outlook is promising from a theoretical perspective and continues to become more promising

as more knowledge is accumulated, the theoretical modeling requires assumptions about the physics and forethought about its potential issues. While care was taken, experiments are crucial to confirm that these choices were correct, to observe the function of the phonovoltaic, and, hopefully, to confirm its potential as an improved, solid-state heat harvester.

APPENDICES

APPENDIX A

Graphene under a uniaxial strain

Despite the initial *ab initio* results by Ni *et al.* suggesting that arbitrary uniaxial strains open a bandgap in graphene[57], the tight-binding modeling of Perier *et al.* showed that strains in excess of 0.2 are required to open a bandgap, and they hypothesized that that the *ab initio* simulations missed the movement of the Dirac-point from the K to M point under strain[66]. This supposition was confirmed by Ni *et al.*, who additionally proposed that under the strain requirements proposed by Periera *et al.*, the σ^* -band becomes the lowest-energy conduction band at M and may prevent the a bandgap from opening[58].

Figure A.1 presents the *ab initio* low-energy bandstructure for variations in the uniaxial strain, where the strained graphene unit cells are prepared in Quantum Espresso QE-2009,pbe1,pbe2 by applying a uniaxial strain on graphene in the x -direction (zig-zag) and then relaxing the cell in the y -direction. Then, a self-consistent DFT simulation on a $120 \times 120 \times 1$ k_e -mesh provides the charge density. The bandstructure is then found along the Γ -K-M high-symmetry line on a $1000 \times 1 \times 1$ k_e -mesh.

The results show that strains exceeding 0.25 are required to open a gap. While the σ^* -band does cross over the π^* -band to become the first-conduction band, a bandgap still opens at M. However, even under strains exceeding 0.3, the bandgap

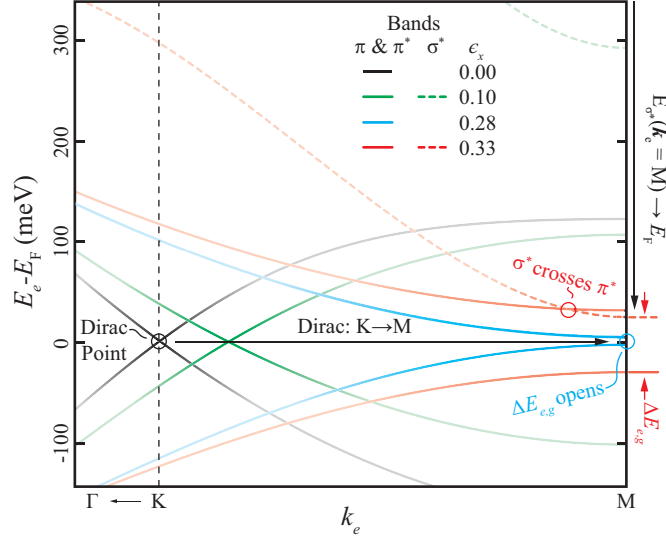


Figure A.1: The low-energy bandstructure of graphene for variations in the uniaxial strain (ϵ_x). Under a small strain, the Dirac-point moves from K towards M and the σ band moves towards the Fermi level at M. Around $\epsilon_x = 0.25$, the Dirac-point reaches M and a bandgap opens between the π bands. Around $\epsilon_x = 0.3$, the σ^* band becomes the first conduction band, reducing the bandgap.

remains extremely narrow, in part due to the crossing of σ^* and π^* -bands. Such substantial strains are impractical, at best, and fall well beyond the elastic deformation of graphene. Moreover, the application of a tensile strain reduces the energy of the optical phonon modes[54], further limiting strained graphene as a pV material.

In contrast, it has been shown that non-uniaxial strains induce a gauge field which in turn opens a band gap through the quantum hall effect[27]. However, this approach limits the pV to a 2-D device, whereas functionalization is potentially applicable to graphite and enables a 3-D cell. Thus, this study focuses on functionalization, and in particular, the partial hydrogenation of graphite.

APPENDIX B

Ensemble Monte Carlo Simulation

The discussion of Monte-Carlo simulations presented below follows the introduction presented by Lundstrom[44]. At the center of MC simulation is the generation of random numbers which are used to select events or conditions using a known probability distribution. Here, the MC method is discussed for its ability to solve the BTE without requiring an exact solution to the complicated partial-differential equation given in Eq. (3.2). That is, the MC method simulates electrons as classical particles which are influenced by forces, e.g., an electric field, and by scattering events, e.g., the emission or absorption of a phonon, as described by the BTE. By simulating millions of electron trajectories, one can determine any of the quantities represented in the BTE or its moments, e.g., the electron current, energy and momentum distributions, or net heat generation.

B.1 Scattering events

The major ingenuity of the MC method is to accurately represent the in- and out-scattering term of the BTE through the statistical selection of a scattering time, Δt_s , during which the simulated electron is in free-flight, and after which it scatters with some other energy carrier. The MC method uses a total scattering rate, $\dot{\gamma}_o$, to

choose this scattering time, where

$$(B.1) \quad \Delta t_s = -\frac{1}{\dot{\gamma}_o} \ln(r_{s,1})$$

and $r_{s,1} \in (0, 1)$ is a random number with uniform distribution. Then, the method checks which scattering interaction occurs by using a second uniformly distributed random number, $r_{s,2} \in (0, 1)$. The method loops through all n_s scattering mechanisms considered, summing across each rate until the sum is greater than $r_{s,2}\dot{\gamma}_o$. Once this criterion is met, the electron is scattered by the last scattering mechanism considered (i.e., given a new momentum and energy according to the scattering mechanism). If this criterion is not met, the electron does not scatter (or self-scatters). For this method to correctly model the scattering of the electrons, the total scattering rate must be greater than the sum of all scattering rates.

Pseudocode for this method is presented below.

```

stop =  $r_{s,2}\dot{\gamma}_o$ 
sum = 0
for  $i$  in range( $n_s$ ):
    sum +=  $\dot{\gamma}_{e-i}(\mathbf{k}_e)$ 
    if stop < sum:
        return  $i$ 
return -1

```

Here, returning -1 indicates that no scattering occurs, while returning i indicates that the scattering mechanism $\dot{\gamma}_{e-i}$ occurs. This pseudocode uses some python functions, when required. However, the code used in this thesis is implemented in C, and should typically be implemented in a fast and parallelizable language like C or Fortran.

B.2 Free-flight

Between scattering events, the electron is said to be in “free-flight.” That is, it travels as a classical particle moving some distance ($\Delta\mathbf{x}$) according to its velocity, acceleration, and time-of-flight (Δt_s). For a massless electron, e.g., one in graphene, under some electric field \mathbf{e}_f , these quantities are

$$(B.2) \quad \Delta\mathbf{x} = \frac{\mathbf{k}_e}{\nu_e} \Delta t_s - \frac{\Delta t_s^2 \mathbf{e}_f}{2\nu_e}$$

$$(B.3) \quad \Delta\mathbf{k}_e = \frac{\mathbf{e}_f}{\nu_e},$$

where ν_e is the constant group velocity of the electron bands.

B.3 The electron-superparticle and time-discretization

With algorithms describing the free-flight and scattering of an electron, one can simulate the trajectory of a single electron accurately, provided the electron behavior is classical, the scattering mechanisms and their rates are comprehensively and accurately incorporated, and the electronic dispersion is accurately modeled. From the record of the electron momentum and energy over time, one can determine the electron mobility of the material or the electron energy and momentum distribution. However, it is impossible to accurately model the electron-electron interactions, non-degenerate effects, or connect the simulations to the Poisson equation (a self-consistent electric field) or the evolution of a hot optical phonon population.

Generally, an ensemble approach is used to solve these problems. That is, millions of electron-superparticles are simulated simultaneously, where each superparticle represents many electrons. With a sufficient number of superparticles, one can accurately resolve the transient distribution of electrons in real- or momentum-space. Thus, one can calculate the electron concentration within finite volumes of a device,

use this to solve the Poisson equation, and calculate the internal electric fields created by variations in the electron and ion concentrations. Alternatively, one can track the emission and absorption of optical phonons by electrons over a period of time, solve the phonon energy equation to track the temperature of the phonon distributions in real- or momentum-space, and then update the scattering rates used in the MC simulation of electrons (the MC loop).

A time-discretization scheme must be used to align all of the superparticles in time before updating any of the external quantities like $T_{p,o}(\mathbf{x}, \mathbf{k}_p)$ or \mathbf{e}_f . Typically, one loops through each superparticle, simulating it for a short time, Δt , before moving on to the next one. Care must be taken to simulate any free-flight time remaining at the end of one time step upon entering the next time step. Additionally, one must choose a sufficiently large time step and simulate a sufficiently large electron ensemble in order to avoid instability. When performing a self-consistent MC simulation, for example, the time step must be larger than the plasma frequency of the material, or the Poisson solution may oscillate. Similar care must be taken when connecting phonon and electron simulations, as discussed below.

B.4 Coupled electron and phonon simulation

In Chapter VI, an ensemble MC simulation is performed to investigate the spectral heating of an optical phonon population. To accomplish this, the number of optical phonons emitted and absorbed at each $\mathbf{k}_p = (k_{p,r}, \theta_p)$ is tracked during the ensemble MC loop, as depicted in Fig. B.1. After the MC loop, the total energy deposited or removed from each bin is calculated $[\dot{S}_{e-p}(\mathbf{k}_p)]$, and the phonon energy equation is solved for that bin. In addition to the electron-phonon interactions, the phonon energy equations includes the in- and out-scattering caused by the phonon-

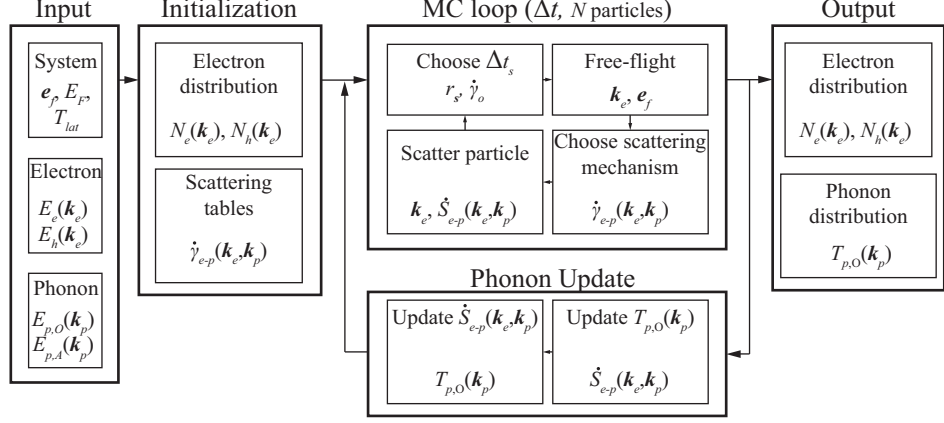


Figure B.1: A flowchart of the coupled MC-phonon simulation. The chart includes the major sub-routines and the primary quantities they manipulate or require. The program requires information on the electronic and phononic bandstructure as well as system information, such as the field strength, Fermi energy, and lattice temperature. Then, the program initializes the electron and phonon populations before proceeding with the main loop, which alternates between the MC loop (which updates the electron distribution) and the phonon block (which updates the phonon distribution and the related scattering mechanisms). After convergence, the electron and phonon distributions are output for analysis.

phonon interactions $[\dot{S}_{p-p}(\mathbf{k}_p)]$. Here, the phonon-phonon up- and down-conversion is modeled as a linear function of the temperature difference between that mode and a specified lattice temperature, T_{lat} , i.e.,

$$(B.4) \quad \dot{S}_{p-p}(\mathbf{k}_p) = A_{p-p}(T_{lat} - T_{p,O}),$$

and A_{p-p} is a phonon-phonon coupling coefficient assumed to be independent of \mathbf{k}_p .

Thus, the energy equation is

$$(B.5) \quad c(T_{p,O}) \frac{\partial T_{p,O}}{\partial t} = \dot{S}_{e-p} + \dot{S}_{p-p}(T_{p,O}),$$

where c is the heat capacity and we have dropped the notation indicating \mathbf{k}_p dependence in order to simplify the result. This convention is maintained for the rest of this section. Often, the transient behavior is not desired, in which case it is simple to solve for $T_{p,O}$, i.e.,

$$(B.6) \quad T_{p,O} = \frac{\dot{S}_{e-p}}{A_{p-p}} + T_{lat}.$$

To maintain stability in the combined MC-phonon solution, however, the result must be weighted by its previous value, such that

$$(B.7) \quad T_{p,O}^{(i)} = (1 - \lambda)T_{p,O}^{(i-1)} + \lambda\left(\frac{\dot{S}_{e-p}}{A_{p-p}} + T_{lat}\right),$$

where $\lambda \in (0, 1)$ slows the change in temperature when it approaches zero and can cause stability issues when it approaches unity. Here, a lambda around 0.02 and time step around one ps is found to maximize convergence in simulations with around 1 to 10 million superparticles without causing convergence issues. If the transient response is required, a backward euler method is suitable, but caution must be taken in choosing an appropriate Δt .

B.5 Building an efficient and fast MC program

With millions of particles and hundreds of time steps required to accurately solve the spatially-varying BTE self-consistently or model the nonequilibria in the phonon populations accurately, it is imperative that the MC simulation is efficient and fast. Typically, this requires pre-computing as many quantities as possible before entering into the ensemble MC simulation. Indeed, any function used inside the MC loop will be called billions to trillions of times. Thus, the scattering rate of each mechanism for each \mathbf{k}_e and \mathbf{k}_p are pre-calculated and then stored in tables. After each time step, the rates are updated to reflect the change in the phonon occupation so that the scattering algorithm is as quick as possible.

Parallelization of the MC simulation is also required to simulate a million or more particles in a reasonable amount of time. Fortunately, the ensemble MC simulation is "embarrassingly" parallel within a single time step. That is, there is no interaction between any two particles in the ensemble during the MC loop itself. Therefore, using additional computer cores can speed-up computation linearly. In this thesis,

the openMP parallelism scheme developed by Intel is used to achieve this drastic improvement. With only 8 cores, the program developed can simulate 10 million particles for 200 ps in a single day. With 32 cores, the program can achieve the same results in 6 hours. Figure B.1 shows a flow-chart of the implemented MC simulation.

APPENDIX C

Hydrodynamic Simulations

The hydrodynamic model takes the first three moments of the BTE to simulate the electron transport[44]. These moments conserve the carrier density (n_i), momentum density (\mathbf{j}_i), and kinetic energy density (\mathbf{w}_i) for electron ($i = e$) and hole ($i = h$), i.e.,

$$\begin{aligned}
 \nabla \cdot \mathbf{j}_i &= e_c \dot{n}_i, \\
 \mathbf{j}_i &= \mu_i (\pm k_B T_i \nabla n_i + k_B n_i \nabla T_i - e_c n_i \nabla \varphi_e), \\
 \nabla \cdot \mathbf{w}_i &= -\mathbf{j}_i \cdot \nabla \varphi - \sum \dot{w}_i,
 \end{aligned}
 \tag{C.1}$$

where T_i and μ_i are the temperature and mobility of carrier i . These equations track the drift and diffusion of electron and hole populations as well as the diffusion and advection of kinetic energy, and \dot{n}_i and \dot{w}_i quantify the addition of carriers and kinetic energy to population i . The kinetic energy flux is

$$\mathbf{w}_i = \nabla \frac{3}{2} k_B T_i \mathbf{j}_i - \kappa_i \nabla T_i,
 \tag{C.2}$$

where the thermal conductivity is

$$\kappa_i = \frac{\pi^2}{3} \frac{k_B^2}{e_c} T_i \mu_i n_i,
 \tag{C.3}$$

from the Weidemann Franz law.

Here, the electron-phonon interaction drives both \dot{n}_i and \dot{w}_i . The generation model follows the band-to-band models[81] discussed previously, i.e.,

$$(C.4) \quad \dot{n}_i = -a_{e-p}[n_e n_h - n_i(T_{p,O})^2],$$

where a_{e-p} is the generation coefficient associated with the electron-phonon coefficient and $n_i(T_{p,O})$ is the intrinsic carrier concentration at $T_{p,O}$. The kinetic energy imparted to the electron (and hole) population per generation event is, on average, $(E_{p,O} - \Delta E_{e,g})/2$. The corresponding energy transfer \dot{s}_G is

$$(C.5) \quad \dot{w}_G = \frac{E_{p,O} - \Delta E_{e,g}}{2} \dot{n}_e.$$

Additionally, the electron kinetic energy density ($3/2k_B T_e n_e$) equilibrates with the optical phonon temperature. The corresponding energy transfer is

$$(C.6) \quad \dot{w}_{i-p,O} = \frac{3}{2} k_B \frac{T_i - T_{p,O}}{\tau_{i-p,E}} n_i,$$

where $\tau_{i-p,E}$ is the electron phonon energy relaxation time[44].

Furthermore, the Poisson equation ensures a self-consistent simulation, i.e.,

$$(C.7) \quad \nabla \cdot \epsilon_e \epsilon_o \nabla \varphi = -e_c (n_e + n_D - n_h - n_A),$$

where $\epsilon_e \epsilon_o$ is the electrical permittivity of the material and n_D and n_A are the doping densities for electron donor and acceptor atoms.

The optical ($i = p, O$) and acoustic phonon ($i = p, A$) populations are modeled using the conduction equation, i.e.,

$$(C.8) \quad -\nabla \cdot \nabla \kappa_i T_i = \sum \dot{s}_{i-j},$$

where the optical phonon population gains energy from an external source ($\dot{s}_{p,O-in}$) and loses energy for each generation event (\dot{s}_G), from heating electron (and hole)

($\dot{s}_{p,O-e}$), and downconversion ($\dot{s}_{p,O-p,A}$), which the acoustic phonon population absorbs, i.e.,

$$\begin{aligned}
\dot{s}_G &= E_{p,O}\dot{n}_e, \\
\dot{s}_{p,O-i} &= -\dot{w}_{i-p,O}, \\
\dot{s}_{p,O-p,A} &= E_{p,O}a_{p-p}[f_{p,O}^\circ(T_{p,A})^2 - f_{p,O}^\circ(T_{p,O})^2], \\
\text{(C.9)} \quad \dot{s}_{p,A-p,O} &= -\dot{s}_{p,O-p,A},
\end{aligned}$$

where $f_{p,O}^\circ(T)$ is the equilibrium optical phonon occupancy at temperature T , and a_{p-p} is the downconversion coefficient associated with the anharmonic coupling strength. Note that Eq. (C.9) assumes that the acoustic phonon populations ($f_{p,A}^{\prime\circ}(T)$ and $f_{p,A}^{\prime\prime\circ}(T)$) are non-degenerate and classical statistics are appropriate, i.e.,

$$\begin{aligned}
f_{p,O}^\circ(T) &= \exp\left(-\frac{E_{p,O}}{k_B T}\right) \\
\text{(C.10)} \quad &= f_{p,A}^{\prime\circ}(T)f_{p,A}^{\prime\prime\circ}(T).
\end{aligned}$$

The hydrodynamic, Poisson, and phonon equations form a set of seven closed balance equations. Note that the closure involves the following assumptions: the kinetic energy is primarily thermal ($w = 3/2k_B T$), populations are non-degenerate, there is equilibrium within but not between populations e , h , p , O , and p , A , and the temperature tensor is diagonal. If the material is anisotropic care must be taken with the transport coefficients and the assumption of a diagonal temperature tensor; however, the transport has negligible effect on a sufficiently thin pV cell.

C.1 Boundary Conditions

The optical phonon is excited to a constant temperature in the active region, and it is not allowed to escape at the contacts ($\nabla T_{p,O} = 0$). (This assumes that the contact

material has no optical phonon mode of comparable energy.) All other temperatures are maintained at the contact temperature T_c . An Ohmic contact is simulated for the both carriers when surface recombination occurs (w/SR). Otherwise, the no minority current is allowed to enter the contact and only the majority carrier has its density maintained by the Ohmic contact (w/o SR), i.e.,

All Simulations:

$$\begin{aligned}
e_c\varphi(0) &= E_F(0), & e_c\varphi(L) &= E_F(L) - \Delta\varphi_a, \\
\nabla T_{p,O}(0, L) &= 0, & T_{p,A}(0, L) &= T_e(0, L) = T_h(0, L) = T_c, \\
n_h(0) &= n_{e,v} \exp\left[\frac{E_{e,v} - E_F(0)}{k_B T_c}\right], & n_e(L) &= n_{e,c} \exp\left[\frac{E_F(L) - E_{e,c}}{k_B T_c}\right].
\end{aligned}$$

w/SR:

$$n_e(0) = n_{e,c} \exp\left[\frac{E_F(0) - E_{e,c}}{k_B T_c}\right], \quad n_h(L) = n_{e,v} \exp\left[\frac{E_{e,v} - E_F(L)}{k_B T_c}\right].$$

w/o SR:

$$\begin{aligned}
j_e(0) &= 0, \text{ i.e.,} & j_h(L) &= 0, \text{ i.e.,} \\
\nabla T_e(0) &= 0, & \nabla T_h(L) &= 0, \\
\text{(C.11) } n_e(0) &= \frac{k_B T_e}{e_c} \frac{\nabla n_e}{\nabla \varphi_e}, & \nabla n_h(L) &= -\frac{k_B T_h}{e_c} \frac{\nabla n_h}{\nabla \varphi_e},
\end{aligned}$$

where E_F is the Fermi energy and $n_{e,c}$ and $n_{e,v}$ are the effective density of states for conduction and valence bands.

C.2 Surface Recombination

The negative effects outlined in Section 3.4.2 are shown in Fig. C.1. When the generation occurs near the contact, a significant number of minority carriers accumulate in the p -region, as shown in Fig. C.1(a). When these minority carriers are prevented from entering the contact and recombining, they diffuse towards the junction, which separates them from the majority carrier, and then the opposing

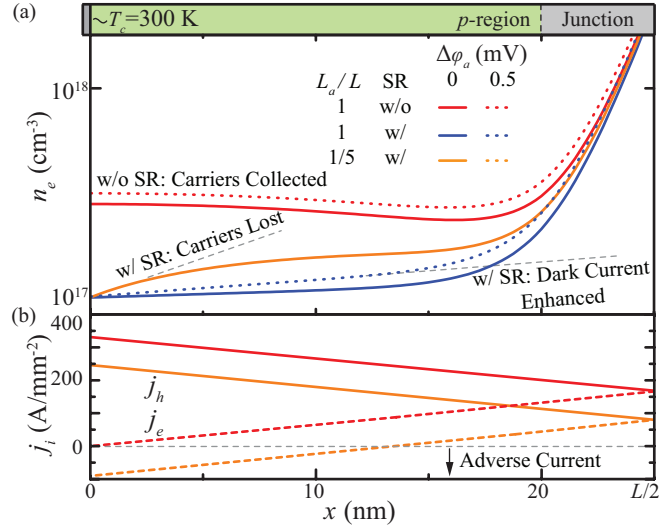


Figure C.1: (a) Minority carrier density and (b) electron and hole currents in a pV cell with and without surface recombination (SR) for variations in the active volume and applied potential. With SR, carriers generated near the contact are lost instead of being collected. Moreover, the applied voltage drives minority carriers into the contacts, instead of reducing the net generation, reducing pV performance.

contact collects them. Conversely, when SR occurs, these minority carriers diffuse into the adjacent contact as shown in Fig. C.1(a). Indeed, for $L_a = L$, wherein a large minority density gradient develops at the contact ($x = 0$). This creates a large adverse current near the contact.

While restricting the active region to the junction minimizes this effect, an applied potential drives a substantial number of minority carriers into the contact regardless of L_a/L , as shown in Fig. C.1(a). Thus, an efficient pV cell must utilize window layers on both contacts in order to prevent surface recombination.

BIBLIOGRAPHY

BIBLIOGRAPHY

- [1] S. Adachi. *Properties of Group-IV, III-V, and II-IV Semiconductors*. Wiley, 2005.
- [2] S. Baroni, S. de Gironcoli, A. D. Corso, and P. Giannozzi. Phonons and related crystal properties from density-functional perturbation theory. *Rev. Mod. Phys.*, 73:515, 2001.
- [3] S. Baroni, S. de Gironcoli, A. D. Corso, and P. Giannozzi. Phonons and related crystal properties from density-functional perturbation theory. *Rev. Mod. Phys.*, 73:515, 2001.
- [4] M. Bartowiak and G. Mahan. Heat and electricity transport through interfaces. *Semiconductors and Semimetals*, 70:245, 2001.
- [5] A. Becker, R. Chavez, N. Petermann, G. Schierning, and R. Schmechel. Enhancement of thermal to electrical energy conversion with thermal diodes. *Mat. Res. Soc. Symp. Proc.*, 691:G8.37.1, 2002.
- [6] P. Blochl. *Phys. Rev. B*, 50:17953, 1994.
- [7] N. Bonini, Lazzeri, N. Marzari, and F. Mauri. Phonon anharmonicities in graphite and graphene. *Phys. Rev. Lett.*, 99:176802, 2007.
- [8] E. V. Castro, K. S. Novoselov, S. V. Morozov, N. M. R. Peres, J. M. B. L. dos Santos, J. Nilsson, F. Guinea, A. K. Geim, and A. H. C. Neto. Biased bilayer graphene: Semiconductor with a gap tunable by the electric field effect. *Phys. Rev. Lett.*, 99:216802, Nov 2007.
- [9] C.-K. Chang, S. Kataria, C.-C. Kuo, A. Ganguly, B.-Y. Wang, J.-Y. Hwang, K.-J. Huang, W.-H. Yang, S.-B. Wang, C.-H. Chuang, M. Chen, C.-I. Huang, W.-F. Pong, K.-J. Song, S.-J. Chang, J.-H. Guo, Y. Tai, M. Tsujimoto, S. Isoda, C.-W. Chen, L.-C. Chen, and K.-H. Chen. Band gap engineering of chemical vapor deposited graphene by in situ bn doping. *ACS Nano*, 7(2):1333–1341, 2013.
- [10] R. Chavez, S. Angst, J. Hall, J. Stoetzel, V. Kessler, L. Bitzer, F. Maculewicz, N. Benson, H. Wiggers, D. Wolf, G. Schierning, and R. Schmechel. High temperature thermoelectric device concept using large area pn junctions. *J. Elec. Mat.*, 43:2376, 2014.
- [11] R. Chavez, A. Becker, V. Kessler, M. Engenhorst, N. Petermann, H. Wiggers, G. Schierning, and R. Schmechel. A new thermoelectric concept using large area pn junctions. *Mat. Res. Soc. Symp. Proc.*, 1543:3, 2013.
- [12] C. da Silva, F. Saiz, D. A. Romero, and C. Amon. Coherent phonon transport in short-period two-dimensional superlattices of graphene and boron nitride. *Phys. Rev. B*, 93:125427, 2016.
- [13] L. da Silva and M. Kaviani. Micro-thermoelectric cooler: interfacial effects on thermal and electrical transport. *Int. J. Heat Mass Transfer*, 47:2417, 2004.
- [14] D. Ecsedy and P. Klemens. Thermal resistivity of dielectric crystals due to four-phonon processes and optical modes. *Phys. Rev. B*, 15:5957, 1976.

- [15] D. Elias, R. Nair, T. Mohiuddin, S. Morozov, P. Blake, M. Halsall, A. Ferrari, D. Boukhvalov, M. Katsnelson, A. Geim, and K. S. Novoselov. Control of graphene's properties by reversible hydrogenation: Evidence for graphane. *Science*, 323:610, 2009.
- [16] M. N. et al. Semiconducting graphene from highly ordered substrate interactions. *Phys. Rev. Lett.*, 115:13680, 2015.
- [17] X. Fan, Z. Shen, A. Liu, and J.-L. Kuo. *Nano.*, 4:2157, 2012.
- [18] D. Frank, Y. Taur, and H. Wong. Generalized scale length for two-dimensional effects in mosfets. *Electron Device Lett., IEEE*, 19:385, 1998.
- [19] K. Fushinobu, A. Majumdar, and K. Hijikata. Heat generation and transport in submicron semiconductor devices. *ASME J. Heat Transfer*, 117:25, 1995.
- [20] P. Gava, M. Lazzeri, A. M. Saitta, and F. Mauri. Ab initio study of gap opening and screening effects in gated bilayer graphene. *Phys. Rev. B*, 79:165431, Apr 2009.
- [21] V. Georgakilas, M. Otyepka, A. B. Bourlinos, V. Chandra, N. Kim, K. C. Kemp, P. Hobza, R. Zboril, and K. S. Kim. Functionalization of graphene: Covalent and non-covalent approaches, derivatives and applications. *Chem. Rev.*, 112(11):6156, 2012.
- [22] P. Giannozzi, S. Baroni, N. Bonini, M. Calandra, R. Car, C. Cavazzoni, D. Ceresoli, G. L. Chiarotti, M. Cococcioni, I. Dabo, A. Dal Corso, S. de Gironcoli, S. Fabris, G. Fratesi, R. Gebauer, U. Gerstmann, C. Gougoussis, A. Kokalj, M. Lazzeri, L. Martin-Samos, N. Marzari, F. Mauri, R. Mazzarello, S. Paolini, A. Pasquarello, L. Paulatto, C. Sbraccia, S. Scandolo, G. Sclauzero, A. P. Seitsonen, A. Smogunov, P. Umari, and R. M. Wentzcovitch. Quantum espresso: a modular and open-source software project for quantum simulations of materials. *J. of Phys.: Cond. Matter*, 21(39):395502, 2009.
- [23] M. O. Goerbig. Electronic properties of graphene in a strong magnetic field. *Rev. Mod. Phys.*, 83:1193–1243, Nov 2011.
- [24] H. Goldsmid. *Electronic Refrigeration*. Pion, 1986.
- [25] X. Gonze and J.-P. Vigneron. Density-functional approach to nonlinear-response coefficients of solids. *Phys. Rev. B*, 39:13120, 1989.
- [26] J. Gordon. Generalized power versus efficiency characteristics of heat engines: The thermoelectric generator as an instructive illustration. *Am. J. Phys.*, 59:551, 1991.
- [27] F. Guinea, M. Katsnelson, and A. Geim. Energy gaps and a zero-field quantum hall effect in graphene by strain engineering. *Nat. Phys.*, 6:30, 2009.
- [28] O. Hellman and I. Abrikosov. Temperature-dependent effective third-order interatomic force constants from first principles. *Phys. Rev. B*, 67:144304, 2003.
- [29] M. Hodes. Optimal pellet geometries for thermoelectric power generation. *IEEE trans. comp. pack. tech.*, 33:307, 2010.
- [30] B. Hunt, J. Sanchez-Yamagishi, A. Young, M. Yankowitz, B. LeRoy, K. Watanabe, T. Taniguchi, P. Moon, M. Koshino, P. Jarillo-Herrero, and R. Ashoori. Massive dirac fermions and hofstadter butterfly in a van der waals heterostructure. *Science*, 340:1427, 2013.
- [31] S. R. J. Maultzsch, C. Thomsen, H. Requardt, and P. Odejón. Phonon dispersion in graphite. *Phys. Rev. Lett.*, 92:075501, 2004.
- [32] Y. Jiao. Graphdiyne: a versatile nanomaterial for electronics and hydrogen purification. *Chem. Commun.*, 47:11843, 2011.

- [33] M. Kaviany. *Heat Transfer Physics*. Cambridge University Press, 2nd edition, 2014.
- [34] P. Klemens. The scattering of low-frequency lattice waves by static imperfections. *Proc. Phys Soc. A*, 68:1113, 1955.
- [35] G. Kresse and J. Furthmüller. *Phys. Rev. B*, 54:11169, 1996.
- [36] G. Kresse and J. Furthmüller. *Comput. Mat. Sci.*, 6:15, 1996.
- [37] G. Kresse and J. Hafner. *Phys. Rev. B*, 47:558, 1993.
- [38] G. Kresse and J. Hafner. *Phys. Rev. B*, 49:14251, 1994.
- [39] G. Kresse and D. Joubert. *Phys. Rev. B*, 59:1758, 1990.
- [40] L. Liao and X. Duan. Graphene for radio frequency electronics. *Materials today*, 15:328, 2012.
- [41] G. Liu, S. Ahsan, A. Khitun, R. Lake, and A. Balandin. Graphene-based non-boolean logic circuits. *J. Appl. Phys.*, 114:154310, 2013.
- [42] H. Liu, Y. Liu, and D. Zhu. Chemical doping of graphene. *J. Mater. Chem.*, 21:3335, 2011.
- [43] J.-B. Liu, P.-J. Li, Y.-F. Chen, Z.-G. Wang, F. Qi, J.-R. He, B.-J. Zheng, J.-H. Zhou, W.-L. Zhang, L. Gu, and T.-R. Li. Observation of tunable electrical bandgap in large-area twisted bilayer graphene synthesized by chemical vapor deposition. *Sci. Rep.*, 5:15285, 2015.
- [44] M. Lundstrom. *Fundamentals of Carrier Transport*. Cambridge Univ. Press, 2nd edition, 2000.
- [45] A. Luque and S. Hegedus, editors. *Handbook of Photovoltaic Science and Engineering*. Wiley, 1984.
- [46] J. L. Mañes, F. Guinea, and M. A. H. Vozmediano. Existence and topological stability of fermi points in multilayered graphene. *Phys. Rev. B*, 75:155424, Apr 2007.
- [47] O. Madelung. *Semiconductors: Data Handbook*. Springer, 2004.
- [48] A. Martí and G. Araújo. Limiting efficiencies for photovoltaic energy conversion in multigap systems. *Solar En. Mat. and Solar Cells*, 43:203, 1996.
- [49] M. Mazzoni, R. Nunes, S. Azevedo, and H. Chacham. Electronic structure and energetics of $B_xC_yN_z$ layered structures. *Phys. Rev. B*, 73:073108, 2006.
- [50] C. Melnick and M. Kaviany. Phonovoltaic. I. Harvesting hot optical phonons in a nanoscale p - n junction. *Phys. Rev. B*, 93:094302, 2016.
- [51] C. Melnick and M. Kaviany. Phonovoltaic. II. Tuning band gap to optical phonon in graphite. *Phys. Rev. B*, 93:125203, 2016.
- [52] C. Melnick and M. Kaviany. In-situ phonon recycling in a graphene fet-pv. *Phys. Rev. Lett.*, In preparation:xx, 2017.
- [53] C. Melnick and M. Kaviany. Phonovoltaic. III. Electron-phonon coupling and figure of merit of graphene:bn. *Phys. Rev. B*, 94:245412, 2017.
- [54] T. M. G. Mohiuddin, A. Lombardo, R. R. Nair, A. Bonetti, G. Savini, R. Jalil, N. Bonini, D. M. Basko, C. Galotit, N. Marzari, K. S. Novoselov, A. K. Geim, and A. C. Ferrari. Uniaxial strain in graphene by raman spectroscopy: g peak splitting, grüneisen parameters, and sample orientation. *Phys. Rev. B*, 79:205433, May 2009.
- [55] P. Moon and M. Koshino. Electronic properties of graphene/hexagonal-boron-nitride moir superlattice. *Phys. Rev. B*, 90:155406, 2014.

- [56] R. Nascimento, J. Martins, R. Batista, and H. Chacham. Band gaps of bn-doped graphene: Fluctuations, trends, and bounds. *J. Phys. Chem. C*, 119:5055, 2015.
- [57] Z. H. Ni, T. Yu, Y. H. Lu, Y. Y. Wang, Y. P. Feng, and Z. X. Shen. Uniaxial strain on graphene: Raman spectroscopy study and band-gap opening. *ACS Nano*, 2(11):2301–2305, 2008.
- [58] Z. H. Ni, T. Yu, Y. H. Lu, Y. Y. Wang, Y. P. Feng, and Z. X. Shen. Uniaxial strain on graphene: Raman spectroscopy study and band-gap opening. *ACS Nano*, 2(11):2301–2305, 2009.
- [59] K. S. Novoselov, A. K. Geim, S. V. Morozov, D. Jiang, Y. Zhang, S. V. Dubonos, I. V. Grigorieva, and A. A. Firsov. Electric field effect in atomically thin carbon films. *Science*, 306(5696):666, 2004.
- [60] A. J. Nozik. Spectroscopy and hot electron relaxation dynamics in semiconductor quantum wells and quantum dots. *Ann. Rev. of Phys. Chem.*, 52(1):193, 2001.
- [61] C. Park, J. Ryou, S. Hong, B. G. Sumpter, G. Kim, and M. Yoon. Electronic properties of bilayer graphene strongly coupled to interlayer stacking and an external electric field. *Phys. Rev. Lett.*, 115:015502, Jul 2015.
- [62] H. Peelaers, A. Hernández-Nieves, O. Leenaerts, B. Partoens, and F. Peeters. Vibrational properties of graphene fluoride and graphane. *App. Phys. Lett.*, 98:051914, 2011.
- [63] F. M. D. Pellegrino, G. G. N. Angilella, and R. Pucci. Strain effect on the optical conductivity of graphene. *Phys. Rev. B*, 81:035411, Jan 2010.
- [64] J. Perdew, K. Burke, and M. Ernzerhof. *Phys. Rev. Lett.*, 77:3865, 1996.
- [65] J. Perdew, K. Burke, and M. Ernzerhof. *Phys. Rev. Lett.*, 78:1396, 1997.
- [66] V. Periera, A. C. Neto, and N. Peres. Tight-binding approach to uniaxial strain in graphene. *Phys. Rev. B*, 80:045401, 2009.
- [67] N. petrone, I. Meric, T. Chari, K. Shepard, and J. Hone. Graphene field-effect transistors for radio-frequency flexible electronics. *IEEE J. Electron Devices Society*, 3:44, 2015.
- [68] S. Piscanec, M. Lazzeri, F. Mauri, A. Ferrari, and J. Robertson. Kohn anomalies and electron-phonon interactions in graphite. *Phys. Rev. Lett.*, 93:185503, 2004.
- [69] E. Pop, S. Sinha, and K. E. Goodson. Heat generation and transport in nanometer-scale transistors. *Proc. of the IEEE*, 94:1587, 2006.
- [70] M. Pumera and C. Hong. Graphane and hydrogenated graphene. *Chem. Soc. Rev.*, 42:5987, 2013.
- [71] S. Reich, J. Maultzsch, C. Thomsen, and P. Ordejón. Tight-binding description of graphene. *Phys. Rev. B*, 66:035412, Jul 2002.
- [72] X. Ruan and M. Kaviani. Enhanced laser cooling of rare-earth-ion-doped nanocrystalline powders. *Phys. Rev. B*, 73:155422, 2006.
- [73] X. Ruan and M. Kaviani. Advances in laser cooling of solids. *J. Heat Transfer*, 129:3, 2007.
- [74] R. Saito, G. Dresselhaus, and M. Dresselhaus. *Physical Properties of Carbon Nanotubes*. Imperial, London, 1998.
- [75] A. O. Sboychakov, A. L. Rakhmanov, A. V. Rozhkov, and F. Nori. Electronic spectrum of twisted bilayer graphene. *Phys. Rev. B*, 92:075402, Aug 2015.

- [76] F. Schwierz. Graphene transistors. *Nat. Nano.*, 5:487, 2010.
- [77] F. Schwierz and J. Liou. Rf transistors: Recent developments and roadmap toward terahertz applications. *Solid-State Electronics*, 51:1079, 2007.
- [78] S. Shin and M. Kaviani. Toward reversing joule heating with a phonon-absorbing heterobarrier. *Phys. Rev. B*, 91:85301, 2015.
- [79] S. Shin, C. Melnick, and M. Kaviani. Heterobarrier for converting hot-phonon energy to electric potential. *Phys. Rev. B*, 87:075317, 2013.
- [80] P. Shinde and V. Kumar. Direct band gap opening in graphene by bn doping: Ab initio calculations. *Phys. Rev. B*, 84:125401, 2011.
- [81] W. Shockley. The theory of p-n junctions in semiconductors and p-n junction transistors. *Bell Sys. Tech. J.*, 28:435, 1949.
- [82] W. Shockley and H. Queisser. Detailed balance limit of efficiency of pn junction solar cells. *J. of Appl. Phys.*, 32(3):510, 1961.
- [83] J. Singh. *Physics of Semiconductors and their heterostructures*. McGraw-Hill, Inc., 1 edition, 1993.
- [84] M. Sluiter and Y. Kawazoe. Cluster expansion method for adsorption: Application to hydrogen chemisorption on graphene. *Phys. Rev. B*, 68:085410, 2003.
- [85] J. Sofo, A. Chaudhari, and G. Barker. Graphane: A two-dimensional hydrocarbon. *Phys. Rev. B*, 75:153401, 2007.
- [86] G. Span, M. Wagner, T. Grasser, and L. Holmgren. Miniaturized teg with thermal generation of free carriers. *Phys. Stat. Sol. (RRL)*, 1:241, 2007.
- [87] G. Srivistava. *The Physics of Phonons*. Adam Hilger, 1990.
- [88] W. Strehlow and E. Cook. Compilation of energy band gaps in elemental and binary compound semiconductors and insulators. *J. Phys. Chem. Ref. Data*, 2:163, 1973.
- [89] N. Troullier and J. L. Martins. Efficient pseudopotentials for plane-wave calculations. *Phys. Rev. B*, 43:1993–2006, Jan 1991.
- [90] N. Vandecasteele, M. Lazzeri, and F. Mauri. Boosting electronic transport in carbon nanotubes by isotopic disorder. *Phys. Rev. Lett.*, 102:196801, 2009.
- [91] N. Vast and S. Baroni. Effects of isotopic disorder on the raman spectra of crystals: Theory and ab initio calculations for diamond and germanium. *Phys. Rev. B*, 61:9387, 2000.
- [92] M. Wagner, G. Span, S. Holzer, and T. Grasser. thermoelectric power generation using large-area si/sige pn-junctions with varying ge content. *Semiconductor Sci. and Tech.*, 22:S173, 2007.
- [93] P. Wallace. The band theory of graphite. *Phys. Rev.*, 71:622, 1947.
- [94] F. Xia, D. B. Farmer, Y.-m. Lin, and P. Avouris. Graphene field-effect transistors with high on/off current ratio and large transport band gap at room temperature. *Nano Letters*, 10(2):715–718, 2010. PMID: 20092332.
- [95] J. Yan, Y. Zhang, P. Kim, and A. Pinczuk. Electric field effect tuning of electron-phonon coupling in graphene. *Phys. Rev. Lett.*, 98:166802, 2007.
- [96] H. Zhang, Y. Luo, X. Feng, L. Zhao, and M. Zhang. Flexible band gap tuning of hexagonal boron nitride sheets interconnected by acetylenic bonds. *Phys. Chem. Chem. Phys.*, 17:20376, 2015.

- [97] Y. Zhang, T.-T. Tang, C. Girit, Z. Hao, M. Martina, A. Zettl, M. Crommie, Y. Shen, and F. Wang. Direct observation of a widely tunable bandgap in bilayer graphene. *Nature*, 459:820, 2009.